

LEVEL

5

Interim

AD A110693

DTIC
SELECTED
FEB 9 1982
H

DCW INDUSTRIES

DTIC FILE COPY

82 02 08 069

4367 TROOST AVENUE, STUDIO CITY, CALIFORNIA 91604

Approved for public release;
distribution unlimited.

COMPUTATIONS WITH A TWO-EQUATION
MODEL OF TURBULENCE FOR THE
1981 STANFORD OLYMPICS

by

David C. Wilcox

Prepared
for

AIR FORCE OFFICE OF SCIENTIFIC RESEARCH
Bolling AFB, Washington, DC

and

NASA LEWIS RESEARCH CENTER
Cleveland, Ohio

Under Contracts

F49620-78-C-0024 and NAS3-22809

DCW Industries, Inc.

4367 Troost Avenue
Studio City, CA 91604
213/769-7571 or 213/790-3844

DTIC
SELECTED
FEB 9 1982
S H

DISTRIBUTION STATEMENT A
Approved for public release;
Distribution Unlimited

ACKNOWLEDGEMENT

DCW Industries, Inc. extends its appreciation to Dr. James Wilson of the Air Force Office of Scientific Research and to Dr. William McNally of the NASA Lewis Research Center for providing the funds which made this project possible.

Accession For	
NTIS GRA&I	<input checked="" type="checkbox"/>
DTIC TAB	<input type="checkbox"/>
Unannounced	<input type="checkbox"/>
Justification	
By _____	
Distribution/ _____	
Availability Codes	
Dist	Avail and/or Special
A	



ABSTRACT

This report summarizes results of 62 computations performed for and included in the proceedings of the 1981 Stanford Conference on Complex Turbulent Flows (commonly referred to as the 1981 Stanford Olympics). The work was done under joint sponsorship of the Air Force Office of Scientific Research (Contract F49620-78-C-0024) and the NASA Lewis Research Center (Contract NAS3-22809).

The objective of this study has been to use a single set of equations modeling turbulent flow phenomena, with no adjustment of closure coefficients from flow to flow, to predict a relatively wide range of turbulent flows. In so doing we have been able to objectively assess the current state of development of a two-equation model of turbulence and to establish its range of applicability.

Applications include: (a) homogeneous turbulent flows; (b) incompressible external and internal flows; and (c) compressible external flows. One of the incompressible cases is flow past a backward facing step and includes boundary-layer separation; all other cases have no separation.

The model employed in our computations predicts flow properties in quite close agreement with experimental data for the constant-pressure boundary layer, the incompressible mixing layer and for flows with surface mass transfer. Additionally, predicted effects of Mach number and surface cooling on a constant-pressure boundary layer are close to measured effects.

For flows with strong adverse pressure gradient, most notably the backward-facing step, the model's predictions differ substantially from corresponding measurements. As an almost uniform trend, the model initially responds to an adverse pressure gradient similar to what has been measured but, upon removal of the gradient, returns to equilibrium more rapidly than measured.

CONTENTS

SECTION	PAGE
ACKNOWLEDGEMENT.....	ii
ABSTRACT.....	iii
1. INTRODUCTION.....	1
2. EQUATIONS OF MOTION.....	3
2.1 Conservation Equations.....	3
2.2 Nonlinear Constitutive Relation.....	4
2.3 System Rotation And Streamline Curvature.....	5
3. BOUNDARY CONDITIONS.....	5
3.1 Integration to the Surface.....	6
3.2 Matching to the Law of the Wall.....	7
4. COMPUTATIONAL TOOLS.....	8
4.1 Homogeneous Turbulent Flows.....	8
4.2 Attached and Free Shear Flows.....	8
4.3 Backward Facing Step.....	8
4.4 Numerical Sensitivity Study.....	8
5. RESULTS.....	10
5.1 Homogeneous Turbulent Flows.....	10
5.1.1 Homogeneous Isotropic Turbulence.....	10
5.1.2 Homogeneous Rotating Turbulence.....	10
5.1.3 Homogeneous Plane Strain.....	11
5.1.4 Homogeneous Shear.....	11
5.2 Constant Pressure Boundary Layer.....	11
5.2.1 Incompressible Case.....	12
5.2.2 Effect of Mach Number.....	12
5.2.3 Effect of Surface Cooling.....	12
5.3 The Mixing Layer.....	12
5.3.1 Incompressible Case.....	12
5.3.2 Effect of Mach Number.....	13
5.4 Flows With Surface Mass Transfer.....	14
5.4.1 Effect of Blowing.....	14
5.4.2 Effect of Suction.....	14
5.5 Boundary Layers With Adverse Pressure Gradient....	15
5.5.1 Incompressible Case.....	15
5.5.2 Compressible Cases.....	15
5.6 Flow Over Transonic Airfoils.....	16
5.6.1 Airfoil RAE 2822.....	16
5.6.2 Airfoil DSMA 523s.....	17
5.7 Diffuser Flows.....	17
5.7.1 Low-Core Turbulence.....	18
5.7.2 High-Core Turbulence.....	18
5.8 Backward Facing Step.....	18
6. SUMMARY AND CONCLUSIONS.....	20
FIGURES.....	22
APPENDIX: WALL FUNCTIONS.....	106
REFERENCES.....	115

1. INTRODUCTION

The objective of our participation in the 1981 Stanford Conference on Complex Turbulent Flows has been to use a single theory to compute as wide a range of flows included in the Conference as possible. In so doing it has been our hope that we can objectively assess progress made to date in developing a universally applicable engineering model of turbulence. To accomplish this objective we have computed 20 flows with a total of 62 separate computations. Table 1 summarizes the flows computed, including the Sponsor for each case.

Table 1. Summary of Flows Computed

Flow Number	Description	No. of Cases	Sponsor
0141/Simple	Incompressible B.L. in Adverse ∇p	1	AFOSR
0142/Entry	Pozzorini Low-Core Turb. Diffuser	1	NASA
0143/Entry	Pozzorini High-Core Turb. Diffuser	1	NASA
0241/Entry	Boundary Layer with Blowing	1	AFOSR
0242/Entry	Boundary Layer with Suction	1	AFOSR
0244/Entry	Boundary Layers with Suction	5	AFOSR
0311/Entry	Mixing Layer Development	1	AFOSR
0371/Simple	Homogeneous Isotropic Turbulence	1	AFOSR
0372/Simple	Homogeneous Rotating Turbulence	3	AFOSR
0374/Simple	Homogeneous Plane Strain	2	AFOSR
0376/Simple	Homogeneous Shear	2	AFOSR
0421/Entry	Backward Facing Step	1	NASA
0612/Simple	Constant Pressure Boundary Layer	1	AFOSR
8101/Simple	Mach No. Effect on Boundary Layer	6	AFOSR
8201/Simple	Wall Temperature Effect on B.L.	6	AFOSR
8403/Simple	Compressible B.L. in Adverse ∇p	9	NASA
8411/Simple	Compressible B.L. in Adverse ∇p	1	NASA
8501/Simple	Mach No. Effect on Mixing Layer	3	AFOSR
8621/Entry	RAE 2822 Transonic Airfoil	10	AFOSR
8623/Entry	DSMA 523s Transonic Airfoil	6	AFOSR

All 62 computations used the two-equation model of turbulence devised by Wilcox and Rubesin¹ with some minor "fine tuning" of the closure coefficients. Computational tools used to solve the equations of motion include: (a) a fourth-order accurate Runge-Kutta integration scheme for the 8 homogeneous turbulent flows (Flows 0371, 0372, 0374 and 0376); (b) a fully elliptic incompressible

program named EDDYNSI for the backward-facing step (Flow 0421); and (c) a compressible/incompressible boundary-layer program named EDDYBL for the other 53 computations.

In the following Sections, we present in detail the equations of motion and boundary conditions employed. We then give a brief description of the numerical tools used followed by a discussion of the various numerical checks made during the course of the many computations. Finally, we summarize results obtained and outline possible future avenues of research.

2. EQUATIONS OF MOTION

This section first presents the basic equations of motion used in this project. Then a nonlinear stress/strain-rate constitutive relation used for the homogeneous turbulent flows is given. Finally, we specify special modifications to the basic model needed for flows with significant system rotation and/or streamline curvature.

2.1 CONSERVATION EQUATIONS

The equations of motion used in all of our computations are those devised by Wilcox and Rubesin. The model is of the two-equation variety in which the Reynolds stress tensor τ_{ij} is assumed proportional to the mean strain rate tensor S_{ij} according to

$$\tau_{ij} = 2\rho\epsilon \left(S_{ij} - \frac{1}{3} \frac{\partial u_k}{\partial x_k} \delta_{ij} \right) - \frac{2}{3} \rho\epsilon \delta_{ij} \quad (1)$$

where ϵ is the eddy diffusivity, e is the turbulent mixing energy, ρ is mass density, u_i is the mean velocity vector, x_i is position vector and δ_{ij} is the Kronecker delta. The mean equations of motion thus are written (for steady flow) as follows.

$$\frac{\partial}{\partial x_j} (\rho u_j) = 0 \quad (2)$$

$$\frac{\partial}{\partial x_j} (\rho u_j u_i) = - \frac{\partial p}{\partial x_i} + \frac{\partial}{\partial x_j} \left(2\mu \left(S_{ij} - \frac{1}{3} \frac{\partial u_k}{\partial x_k} \delta_{ij} \right) + \tau_{ij} \right) \quad (3)$$

$$\frac{\partial}{\partial x_j} (\rho u_j h) = u_i \frac{\partial \bar{p}}{\partial x_i} + \beta^* \rho \omega e + \frac{\partial}{\partial x_j} \left(\left(\frac{\mu}{Pr_L} + \frac{\rho\epsilon}{Pr_T} \right) \frac{\partial h}{\partial x_j} \right) \quad (4)$$

In equations (2-4) \bar{p} is mean pressure, h is mean enthalpy, μ is molecular viscosity, Pr_L and Pr_T are laminar and turbulent Prandtl numbers, ω is turbulent dissipation rate and β^* is a closure coefficient which will be defined momentarily. Before introducing

the two turbulence model equations it is instructive to note that the mean energy equation (4) appears to find the conventional work term $\tau_{ij} \partial u_i / \partial x_j$, replaced by $\beta^* \rho w e$. This is not an ad hoc closure approximation, but rather a closure approximation consistent with those made below in the turbulent energy equation. The correctness of Equation (4) becomes obvious when the resultant equation for total energy, viz, $(h + \frac{1}{2} u_i u_i + e)$, is formed.

To complete our set of equations, we compute the eddy diffusivity in terms of e and w from:

$$\epsilon = \gamma^* e / w \quad (5)$$

where γ^* is a closure coefficient given below in Equations (8).

The equations governing the evolution of e and w are:

$$\frac{\partial}{\partial x_j} (\rho u_j e) = \tau_{ij} \frac{\partial u_i}{\partial x_j} - \beta^* \rho w e + \frac{\partial}{\partial x_j} \left((\mu + \sigma^* \rho \epsilon) \frac{\partial e}{\partial x_j} \right) \quad (6)$$

$$\frac{\partial}{\partial x_j} (\rho u_j w^2) = \gamma \frac{w^2}{e} \tau_{ij} \frac{\partial u_i}{\partial x_j} - \left\{ \beta + 2\sigma \left(\frac{\partial \ell}{\partial x_k} \right)^2 \right\} \rho w^3 + \frac{\partial}{\partial x_j} \left((\mu + \sigma \rho \epsilon) \frac{\partial w^2}{\partial x_j} \right) \quad (7)$$

where ℓ is turbulent length scale defined as $e^{1/2} / w$. In Equations (5-7) there are several closure coefficients whose values are as given in Equations (8).

$$\left. \begin{aligned} \gamma^* &= 1 - (1 - \lambda^2) \exp(-Re_T) \\ \gamma \gamma^* &= \frac{25}{27} \{ 1 - (1 - \lambda^2) \exp(-Re_T / 1.5) \} \\ \lambda &= 1/11, \quad \sigma = \sigma^* = 2/3 \\ \beta &= 3/20, \quad \beta^* = 9/100 \end{aligned} \right\} \quad (8)$$

Note that $Re_T = \rho e / \mu w$ is the turbulent Reynolds number.

2.2 NONLINEAR CONSTITUTIVE RELATION

The homogeneous turbulent flow calculations used the nonlinear stress/strain-rate constitutive relation devised by Wilcox and Rubesin¹

which, for the high Re_T , incompressible cases considered becomes:

$$\frac{\tau_{ij}}{\rho} = 2\epsilon S_{ij} - \frac{2}{3}\epsilon\delta_{ij} + \frac{4\epsilon}{9\beta^* (\omega^2 + 2S_{mn}S_{nm})} (S_{im}\Omega_{mj} + S_{jm}\Omega_{mi}) \quad (9)$$

where $\Omega_{ij} = \frac{1}{2} (\partial u_i / \partial x_j - \partial u_j / \partial x_i)$ is the mean rotation tensor.

2.3 SYSTEM ROTATION AND STREAMLINE CURVATURE

For rotating homogeneous turbulent flow (Case 0372) computations include the Wilcox-Chambers² rotation term. This term is added to the equation for ϵ , which becomes

$$\frac{\partial \epsilon}{\partial t} = \tau_{ij} \frac{\partial u_i}{\partial x_j} + 9\Omega \langle -u'v' \rangle - \beta^* \omega \epsilon \quad (10)$$

Rotation Term

where t is time and Ω is rotation rate. Finally, the transonic airfoil Cases 8621 and 8623 use the Wilcox-Chambers² streamline curvature term which yields the following modified equation for ϵ :

$$\frac{\partial}{\partial x_j} (\rho u_j \epsilon) = \langle -\rho u'v' \rangle \frac{\partial u}{\partial y} - \frac{9}{2} \langle -\rho u'v' \rangle \frac{u}{R} + \dots \quad (11)$$

Curvature Term

where R is surface radius of curvature (positive for convex, negative for concave).

3. BOUNDARY CONDITIONS

For all but the 8 homogeneous cases solid boundaries are present and surface boundary conditions must be specified. With the exception of the backward-facing step, all computations integrated all the way to the surface, $y = 0$. The backward-facing step computation employed "surface" boundary conditions based on the law of the wall. This section describes the surface boundary conditions used in each case.

3.1 INTEGRATION TO THE SURFACE

For integration all the way through the sublayer to the surface, $y = 0$, boundary conditions are as follows:

$$\left. \begin{aligned} u &= 0 \\ T &= T_w \text{ or } \partial T / \partial y = 0 \\ e &= 0 \\ \omega &= Su_\tau / (\beta^{1/2} v) \end{aligned} \right\} \text{ at } y = 0 \quad (12)$$

where T is temperature and subscript w denotes surface. For the dissipation rate, the quantity S is a universal function of surface roughness and mass injection rate defined by (Wilcox-Traci³):

$$\left. \begin{aligned} S &= (S_B^{-1} + S_R^{-1})^{-1} \\ S_B &= 6 / \{v_w^+ (1 + v_w^+)\} \\ S_R &= (36/k^+)^2 + (8/k^+)^{1/2} \end{aligned} \right\} \quad (13)$$

where $v_w^+ = v_w / u_\tau$ is nondimensional injection rate and $k^+ = ku_\tau / v$ is nondimensional roughness height. Note that for suction ($v_w < 0$) we take $S_B^{-1} = 0$ and in the limit of zero roughness and injection the near-surface behavior of ω is:

$$\omega \rightarrow \frac{20}{B} \frac{v}{y^2} \quad \text{as} \quad y \rightarrow 0 \quad (14)$$

where ν is kinematic viscosity.

3.2 MATCHING TO THE LAW OF THE WALL

For the backward-facing step we used boundary conditions consistent with the law of the wall, viz,

$$\left. \begin{aligned} u + \frac{u_T}{\kappa} \log \left(\frac{u_T y}{\nu} \right) + 5.0 \\ e + u_T^2 / \beta^{*3/2} \\ w + u_T / (\beta^{*3/2} \kappa y) \end{aligned} \right\} \text{as } y \rightarrow 0 \quad (15)$$

where $\kappa = .41$ is Karman's constant. While more-accurate boundary conditions (also known as wall functions) are available for our equations (see the Appendix), limited time and funds precluded their use for the Conference.

4. COMPUTATIONAL TOOLS

4.1 HOMOGENEOUS TURBULENT FLOWS

Because of their inherent simplicity, we solved the equations of motion for the 8 homogeneous turbulent flows with a straightforward fourth-order accurate Runge-Kutta integration scheme and, for obvious reasons, the program requires no further description.

4.2 ATTACHED AND FREE SHEAR FLOWS

The lion's share of our computations used the same program, namely our two-dimensional/axisymmetric compressible/incompressible boundary-layer/shear-layer program known as EDDYBL⁴. In performing the calculations all compressible cases were done on a UNIVAC 1108 and all incompressible cases on a TRS-80 Microcomputer. The latter cases were actually done with a version of EDDYBL in which all of the compressibility terms were eliminated. The program is a parabolic marching code which is second-order accurate in both streamwise and normal directions.

4.3 BACKWARD FACING STEP

The backward-facing step case was done with an incompressible, elliptic program known as EDDYNSI. The program is a modified version of the TEACH-2E Code⁵ which also is second-order accurate in streamwise and normal directions.

4.4 NUMERICAL SENSITIVITY STUDY

We performed many numerical accuracy tests on a more or less random sampling of the many cases we computed. In general we tested the effect of total mesh point number, location of mesh point nearest the surface and size of streamwise steps taken. For all of the boundary-layer cases we found 80-100 mesh points normal to the surface with the value of y^+ for the point nearest the surface less than unity to be quite satisfactory. Except for very strong adverse pressure gradient cases there is virtually no loss in accuracy in

taking streamwise steps up to about one boundary-layer thickness. In some of our compressible boundary-layer runs we used as many as 280 points normal to the surface with y^+ nearest the surface as small as .09. The difference in computed integral properties over a 100 point calculation was never found to be more than 2%.

For the backward-facing step case we used meshes which had a total of 196, 529, and 870 mesh points. The total number of mesh points had very little effect on predicted reattachment length although local flow properties varied substantially with the number of points used.

5. RESULTS

This section presents a case-by-case description of results obtained including all plots submitted to the 1981 Stanford Olympics Conference.

5.1 HOMOGENEOUS TURBULENT FLOWS

These flows have no solid boundaries and diffusion across streamlines is negligible. Thus the equations of motion simplify to first-order ordinary differential equations (convective terms are replaced by time rate of change terms, c.f. Equation 10). The equations of motion are trivially integrable using a standard Runge-Kutta algorithm.

Our purpose in doing these flows was to clearly delineate one of the bounds on the applicability range of a two-equation model of turbulence. The assumption of an algebraic relation between the Reynolds stress tensor and the mean strain rate tensor implies that the flow has achieved an "equilibrium" state. Even using a nonlinear stress/strain-rate constitutive relation (Equation 9) accounts only for nonequipartition of energy; departures from equilibrium still are ignored. Results for the four homogeneous turbulent flow cases follow.

5.1.1 Homogeneous Isotropic Turbulence

Figure 1 compares computed and measured turbulent kinetic energy, q^2 for decaying isotropic turbulence. As shown computed and measured energies differ by less than 1% of scale. This close agreement is unsurprising as the ratio of β to β^* has been selected to match measured decay rates for homogeneous isotropic turbulence.

5.1.2 Homogeneous Rotating Turbulence

Figures 2-5 compare computed and measured flow properties for three different rotation rates, viz, $\Omega=0, 20, 80 \text{ sec}^{-1}$. As shown

in Figure 2 (the nonrotating case), we again predict the decay of homogeneous isotropic turbulence quite accurately. Even with $\Omega = 20 \text{ sec}^{-1}$, predicted and measured decay of q^2 are quite close. However, at the highest rotation speed we actually predict an eventual increase in q^2 in contrast to the monotonic decrease measured. Figure 5 compares computed and measured ratios of $\sqrt{u'^2}$ to $\sqrt{v'^2}$. Clearly the measured partition of energy differs substantially from that predicted.

5.1.3 Homogeneous Plane Strain

Two strain rates were considered, viz, $-\partial v/\partial y = \partial w/\partial z = 9.44 \text{ sec}^{-1}$ (Townsend) and 4.45 sec^{-1} (Tucker-Reynolds). Figures 6-8 compare computed and measured normal Reynolds stresses for the higher strain rate while Figures 9-11 correspond to the lower strain rate. As shown, for both cases, w'^2 is reasonably close while predicted u'^2 and v'^2 are about 50% lower than measured.

5.1.4 Homogeneous Shear

Two shear rates were considered, viz, $\partial u/\partial y = 12.9 \text{ sec}^{-1}$ (Champagne, et al) and 48 sec^{-1} (Harris, et al). Figures 12-15 compare computed and measured Reynolds stress components for the lower shear rate while Figures 16-19 correspond to the higher shear rate. For both cases predicted normal and shear stress components are much lower than measured.

5.2 CONSTANT PRESSURE BOUNDARY LAYER

Our next round of applications of the turbulence model is to flow over a flat plate at both incompressible and compressible flow conditions. In all computations, computation was initiated at the leading edge of the plate from laminar profiles. The equations of motion are integrated through transition up to $Re_\theta = 10000$ for all of the compressible cases.

5.2.1 Incompressible Case

Figures 20-22 compare computed and measured velocity profile, skin friction and shape factor for an incompressible flat-plate boundary layer (FPBL). The velocity profile corresponds to a plate-length Reynolds number of 10.9 million. As shown, differences between computed and measured flow properties are well within engineering accuracy.

5.2.2 Effect of Mach Number

Figure 23 compares computed effect of freestream Mach number on an adiabatic-wall FPBL. As shown for Mach number ranging from 0 to 5 and at a momentum-thickness Reynolds number, Re_θ , of 10000, the model equations predict skin friction approximately 3-5% lower than measured. Figure 24 shows the predicted recovery factor as a function of Mach number. The predicted variation is well within experimental data scatter.

5.2.3 Effect of Surface Cooling.

Figure 25 compares computed and measured effects of surface cooling on a Mach 5 FPBL. The adiabatic wall temperature determined from the Mach 5 computation of Subsection 5.2.2 was used for all surface cooling cases. Again computed skin friction is about 3-5% lower than measured.

5.3 THE MIXING LAYER

Perhaps the most basic of all free shear flows is the mixing layer. The mixing layer is the next of our applications. In this subsection we first describe our results for the incompressible case, including effects of velocity ratio. Then we discuss the compressible case.

5.3.1 Incompressible Case

Application of the Wilcox-Rubesin¹ model to this flow found the predicted spreading rate to be .085 as compared to the measured

(consensus) value of .115. Further investigation showed that the spreading rate is strongly affected by the closure coefficients σ and σ^* (see Equations 6-7). Figure 26 shows the predicted effect of σ on spreading rate (the curve was constructed with $\sigma=\sigma^*$). As shown, selecting $\sigma = \sigma^* = 2/3$ yields a spreading rate of .115. This is the "fine tuning" of the Wilcox-Rubesin model alluded to in the Introduction.

Figure 27 compares computed and measured spreading rate as a function of velocity ratio u_2/u_1 where u_2 and u_1 are the velocities of the mixing streams. As shown, predicted spreading rate virtually duplicates the accepted correlation of measured values. Figure 28 compares the computed velocity profile with the measurements of Liepmann and Laufer.

Finally, Figure 29 compares computed and measured development of a mixing layer from separation to a distance 1800 momentum thickness downstream. The predicted asymptotic spreading rate is, as expected, .115. As shown, the initial spreading rate is somewhat higher than measured and falls a bit below measured values farther downstream.

5.3.2 Effect of Mach Number

To assess effects of compressibility, we next compute the adiabatic mixing layer, viz, the mixing of a supersonic stream with a stream of the same fluid at rest having identical total temperatures. In order to differentiate effects of Mach number and density variation we first predicted the Mach zero spreading rate for density ratios of 1/7 and 7. When the denser fluid is at rest the spreading rate is reduced to .111; when the heavier fluid is at rest the spreading rate increases slightly to .116. Then, varying Mach number from 0 to 19, we find virtually no effect whatever on spreading rate (Figure 30).

To be certain no numerical errors are involved we reran all compressible cases with a one-dimensional implicit time marching program to solve the farfield (self-similar) equations and found precisely the same result...no variation of spreading rate with Mach number.

Using the farfield equations we also included (a) transverse pressure gradient, (b) the Saffman-Wilcox⁶ compressibility term and (c) the Wilcox-Chambers streamline curvature term. None of these modifications had any substantial (greater than 10%) effect on predicted spreading rate.

5.4 FLOWS WITH SURFACE MASS TRANSFER

We now turn to more advanced applications, the first of which are flows with surface mass transfer. Only incompressible cases were done, one with surface mass injection and the other six computations with suction. Results follow.

5.4.1 Effect of Blowing

We first consider a constant pressure boundary layer with uniform mass injection, $F = v_w/U_e = .00375$, where U_e is velocity at the boundary layer edge. Figures 31-34 show, respectively, skin friction, momentum thickness, displacement thickness, and four velocity profiles. As shown, computed and measured flow properties are quite close. The largest differences are in momentum and displacement thickness where computed differences are less than 10%.

5.4.2 Effect of Suction

Now we turn to suction where we performed a total of six computations. The first case had a mild adverse pressure gradient and a suction rate $F = -.004$. Figures 35-38 compare computed and measured skin friction, momentum thickness and velocity profiles. Computed skin friction is approximately 5% higher than measured while computed and measured velocity profiles differ by less than 7%. Although larger differences are present for momentum and displacement thickness, computed and measured shape factors are very close.

The other five cases are all at the same freestream flow conditions and have zero pressure gradient. Suction rate for the five cases ranges from $F = 0$ to $-.0144$. Figure 39 compares computed and measured velocity profiles for the unsucked case and for the highest suction rate. As shown, differences are slight. Figures 40-42

display predicted and measured Reynolds stresses (as with the homogeneous turbulent flow cases we used Equation 9 to compute the normal stresses). At the three highest suction rates the shear and streamwise-normal components are within 5% of their measured counterparts. The lateral-normal component shows larger discrepancies.

5.5 BOUNDARY LAYERS WITH ADVERSE PRESSURE GRADIENT

Our attention now turns to effects of adverse pressure gradient, the long standing nemesis of turbulence modelers. Applications included in this subsection are one incompressible computation and ten supersonic computations.

5.5.1 Incompressible Case

Our incompressible application is the carefully documented flow of Samuel and Joubert. Figure 43 exhibits skin friction, Figures 44-45 show shear stress profiles and Figure 46 displays velocity profiles. As a general observation, the computed boundary layer thickens more rapidly than measured and, rather than approaching separation, tends to recover more rapidly than measured as the pressure gradient is removed.

5.5.2 Compressible Cases

Our selection of compressible cases was more extensive including a round of nine computations at Mach 2.2 with three different Reynolds numbers (Acharaya, et al). The tenth computation was at Mach 4 (Zwarts).

Figures 47-49 compare computed and measured skin friction for the nine Mach 2.2 cases. As shown, for all Reynolds numbers, the computed skin friction begins to drop at about the same location as measured, fails to drop as low as measured, and recovers much more rapidly than measured as the adverse gradient is removed.

Figures 50-51 show shape factor for two of the cases. As illustrated the measurements indicate rapid variations in shape factor while the predicted shape factors vary much more gradually. Figures 52-57 display computed and measured velocity, turbulent energy and shear stress profiles. As in the incompressible case, the numerical boundary layers are thicker than measured.

Figures 58-61 compare our numerical results with measurements for Zwarts' Mach 4 boundary layer. While computed and measured shape factor distributions are quite close, all other flow properties show the same general trend as the other adverse pressure gradient cases. That is, the boundary layer tends to recover from the adverse pressure gradient much more rapidly than measured.

5.6 FLOW OVER TRANSONIC AIRFOILS

Continuing in our more advanced applications we turn now to transonic flow past two airfoils, the RAE 2822 design and the DSMA 523s. For the former, computations have been made for five different sets of flow conditions and three different sets of conditions for the latter. All computations have been done with our boundary-layer program EDDYBL using measured pressure distributions. To account for possible significant effects of streamline curvature, the Wilcox-Chambers curvature term (Equation 11) is included for both surfaces of the airfoil.

5.6.1 Airfoil RAE 2822

For this round of airfoil computations, freestream Mach number ranges from .676 to .730 while Reynolds number based on chord length ranges from 2.7 to 6.5 million. All computations are started at the stagnation point and the transition point adjusted to match the measured location by varying freestream turbulence intensity. Figures 62-64 compare computed and measured momentum thickness, shape factor and skin friction for the upper surfaces;

computed properties on the lower surface (dashed lines) are also displayed. As most clearly exhibited in the skin friction distributions, we again find that computed skin friction fails to drop as low as measured and the boundary layers all end up much farther from separation than measured. The latter point again suggests that the predicted boundary layer approaches an equilibrium state much more rapidly than measured as the adverse gradient eases.

5.6.2 Airfoil DSMA 523s

Mach number and Reynolds number range from .6 to .8 and from 2 to 4 million, respectively, for this round of airfoil computations. Figures 65-67 compare predicted and measured skin friction distributions for both airfoil surfaces. On the one hand, theory and experiment are reasonably close on the upper surface for all three cases. On the other hand, the measured boundary layer nearly separates on the lower surface for each case while the numerical boundary layer actually shows an increase in skin friction. Thus, we again observe a more rapid than measured return to equilibrium in an adverse pressure gradient. Figures 68-73 display computed and measured velocity profiles. Except very close to the trailing edge, predicted upper surface profiles differ from those measured by less than 5%. Lower surface profiles show larger differences, particularly in the nearly separated zone.

5.7 DIFFUSER FLOWS

Thus far all of our applications have been to external flows (with the exception of the Samuel-Joubert case which was treated however as an external flow). As part of our overall objective to cover as wide a range of turbulence phenomena, we now focus on two internal flow geometries, viz, flow through a six degree conical diffuser. The first case has low-core turbulence while the second is for high-core turbulence.

5.7.1 Low-Core Turbulence

Figures 74-76 show computed and measured skin friction, velocity profiles and shear stress profiles, respectively. As illustrated in Figure 74, computed skin friction initially falls off at about the same rate as measured but then, in contrast to the measured trend, begins to increase slowly rather than continuing toward separation. The velocity and shear stress profiles (Figures 75-76) show clearly that the numerical boundary layer ceases to grow as rapidly as measured beyond the point where the computed skin friction begins to rise. Again, numerical results suggest the numerical boundary layer heads toward an equilibrium state differing from the measured state. In this case it is unclear whether we are approaching a different equilibrium state or approaching equilibrium more rapidly than measured.

5.7.2 High-Core Turbulence

Computed results for this case are compared with corresponding measurements in Figures 77-79. Although computed and measured skin friction differences are smaller in this case than in the low-core turbulence case, computed skin friction variation again stands in contrast to the measured distribution in a similar manner. That is, rather than decreasing monotonically, the numerical c_f begins to increase slowly as we approach the outlet. As with the low-core turbulence case, velocity and shear stress profiles indicate the numerical boundary layer is much thinner than measured. Again we are either numerically approaching a different equilibrium state than measured or approaching equilibrium much more rapidly.

5.8 BACKWARD FACING STEP

Our final application, flow past a backward-facing step, differs from all of our other applications in a very important way. Specifically, this flow includes boundary-layer separation while the boundary layers in all of our other applications remain attached. Computationally there is also a significant difference between this case

and all of our other computations, viz, we have used "surface" boundary conditions based on the law of the wall (Equation 15) rather than integrating through the viscous sublayer (Equations 12-14). The use of so-called "wall functions" was necessitated by limited time and funds for this project; there is no fundamental reason, however, why Equations (12-14) can't be used.

Figures 80-83 compare computed and measured flow properties including surface pressure distributions, maximum shear stress variation, velocity profiles and shear stress profiles. Predicted reattachment length is 3.7 step heights compared to a measured reattachment length of 7.0 step heights. As shown in Figure 81, computed maximum shear stress is considerably higher than measured through the separated region. As the flow proceeds downstream of reattachment the numerical boundary layer returns to equilibrium at about the same rate as measured, although substantial differences persist to the final station to which computation continues. In this flow the computed boundary layer responds more rapidly to the strong adverse pressure (much stronger than measured) and then returns (from a quite different disturbed state) to equilibrium at about the same rate as measured.

6. SUMMARY AND CONCLUSIONS

The model employed in our computations predicts flow properties in quite close agreement with experimental data for the constant-pressure boundary-layer, the incompressible mixing layer and for flows with surface mass transfer. Additionally, predicted effects Mach number and surface cooling on a constant-pressure boundary layer are close to measured effects.

For flows with strong adverse pressure gradient, most notably the backward-facing step, the model's predictions differ substantially from corresponding measurements. As an almost uniform trend, the model responds to an adverse pressure gradient in a manner similar to that which has been experimentally observed initially, but, upon removal of the gradient, returns to equilibrium more rapidly than measured (e.g., Flows 0142, 0143, 8621, 8623).

Our success with the flows with suction and blowing is in part due to the careful research which has gone into developing appropriate surface boundary conditions for such flows. This success is perhaps an argument in favor of integrating to the surface (as opposed to using wall functions) for this type of flow.

Our relative lack of success in computing flows with strong adverse pressure gradient is less easy to explain. Perhaps we should expect to do poorly when the flow departs even slightly from equilibrium upon observing the gross discrepancies between computed and measured Reynolds stress development for the homogeneous cases. Yet, this would be too easy an explanation as the primary culprit is the eddy-viscosity approximation in the homogeneous case. More plausibly, with a two-equation turbulence model, we may be attempting to describe too much with too little in the turbulent boundary layer. That is, the near-wall portion of the boundary layer responds on a grossly different scale from that of the defect layer. Yet, we attempt, from a single equation (the equation for w) to deduce the scales on which the entire boundary layer will respond and change.

This problem could actually be partly accomodated by using wall functions! A more satisfactory approach, however, might be to use more than a single dissipation rate. In this way we could concentrate more of the physics of the boundary layer (e.g., response of large-scale structure) into the equations of motion.

FIGURES

All figures following are in the form submitted to the 1981 Stanford Olympics. All experimental data references can be obtained from the proceedings of the Conference. Unless otherwise indicated, our computational results are indicated by lines with heavy dots ($\bullet\text{---}\bullet\text{---}\bullet$). Experimental data generally are indicated by open symbols.

PLOT 1 CASE 0371 FILE 2

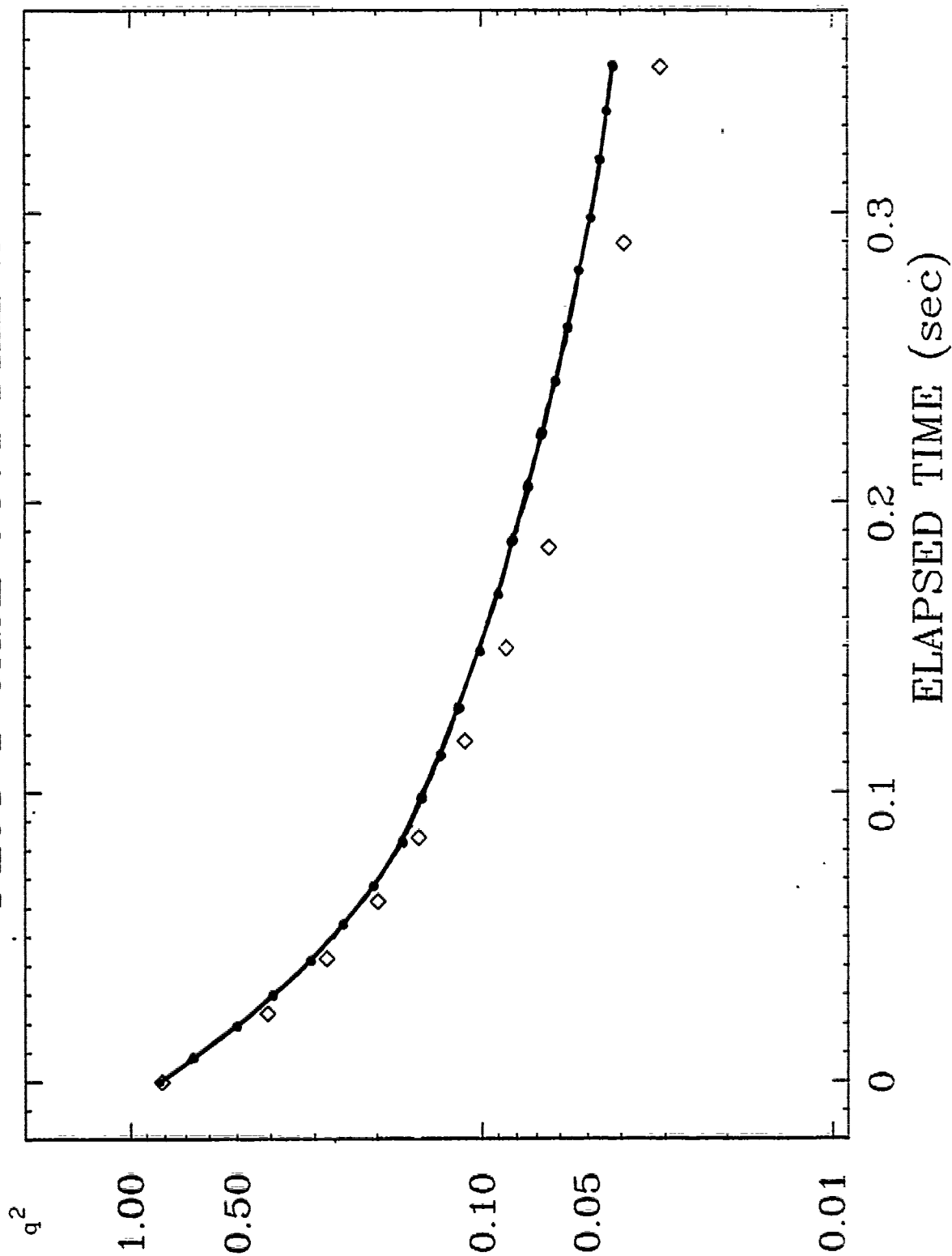


Figure 1. Decay of homogeneous isotropic turbulence.

PLOT 1 CASE 0372A FILE 3

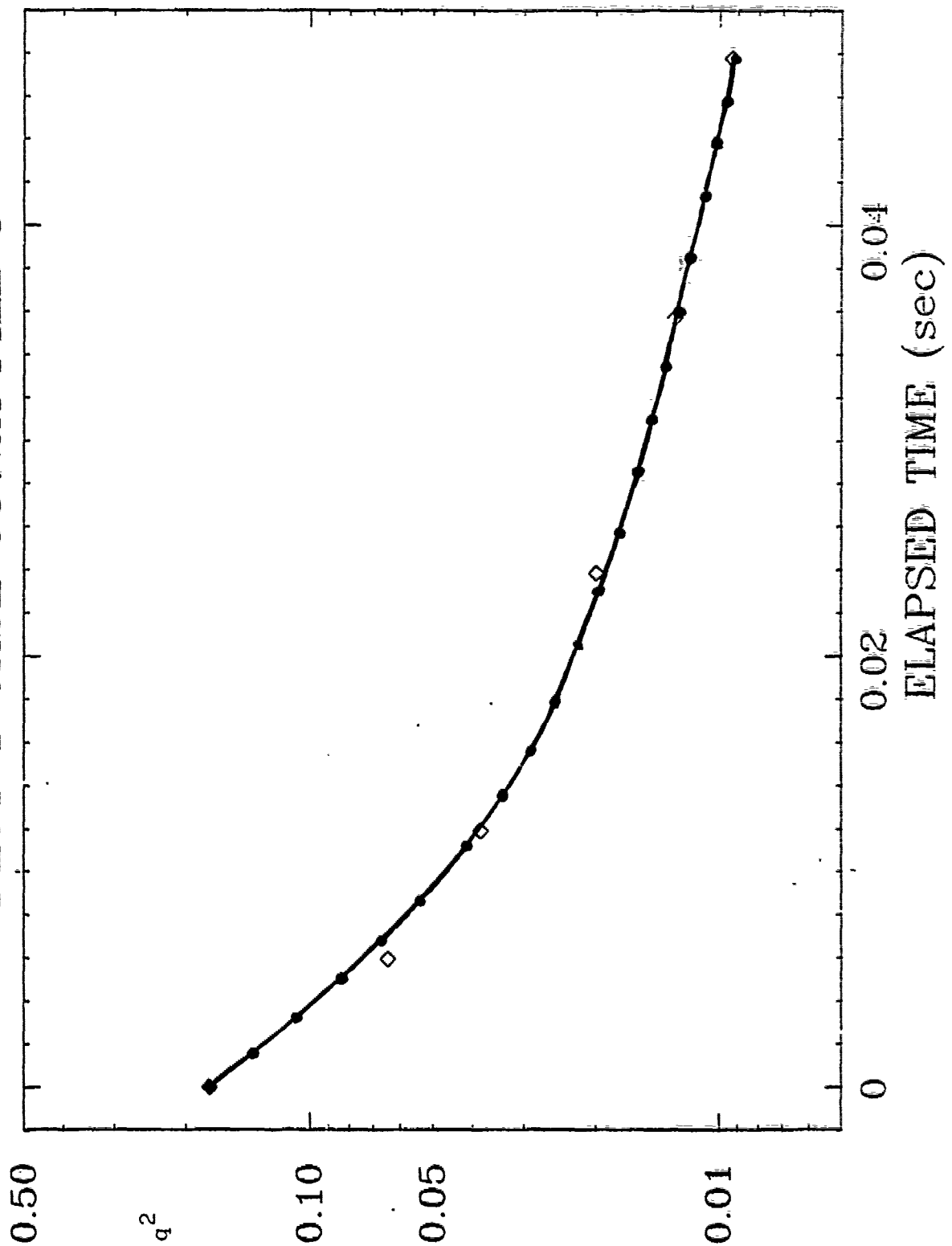


Figure 2. Homogeneous rotating turbulence; $\Omega = 0$.

PLOT 1 CASE 0372B FILE 4

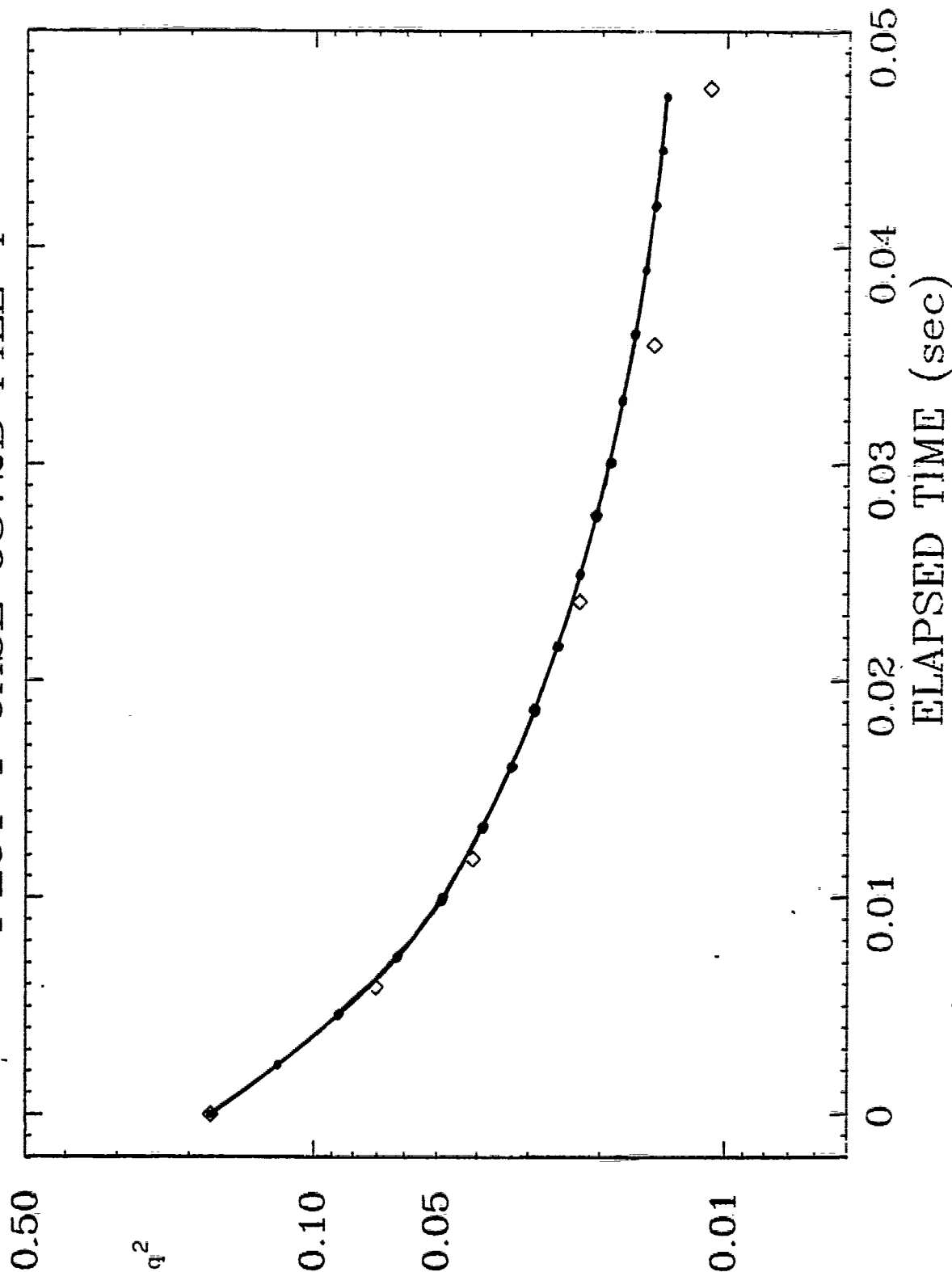


Figure 3. Homogeneous rotating turbulence; $\Omega = 20 \text{ sec}^{-1}$.

PLOT 1 CASE 0372C FILE 5

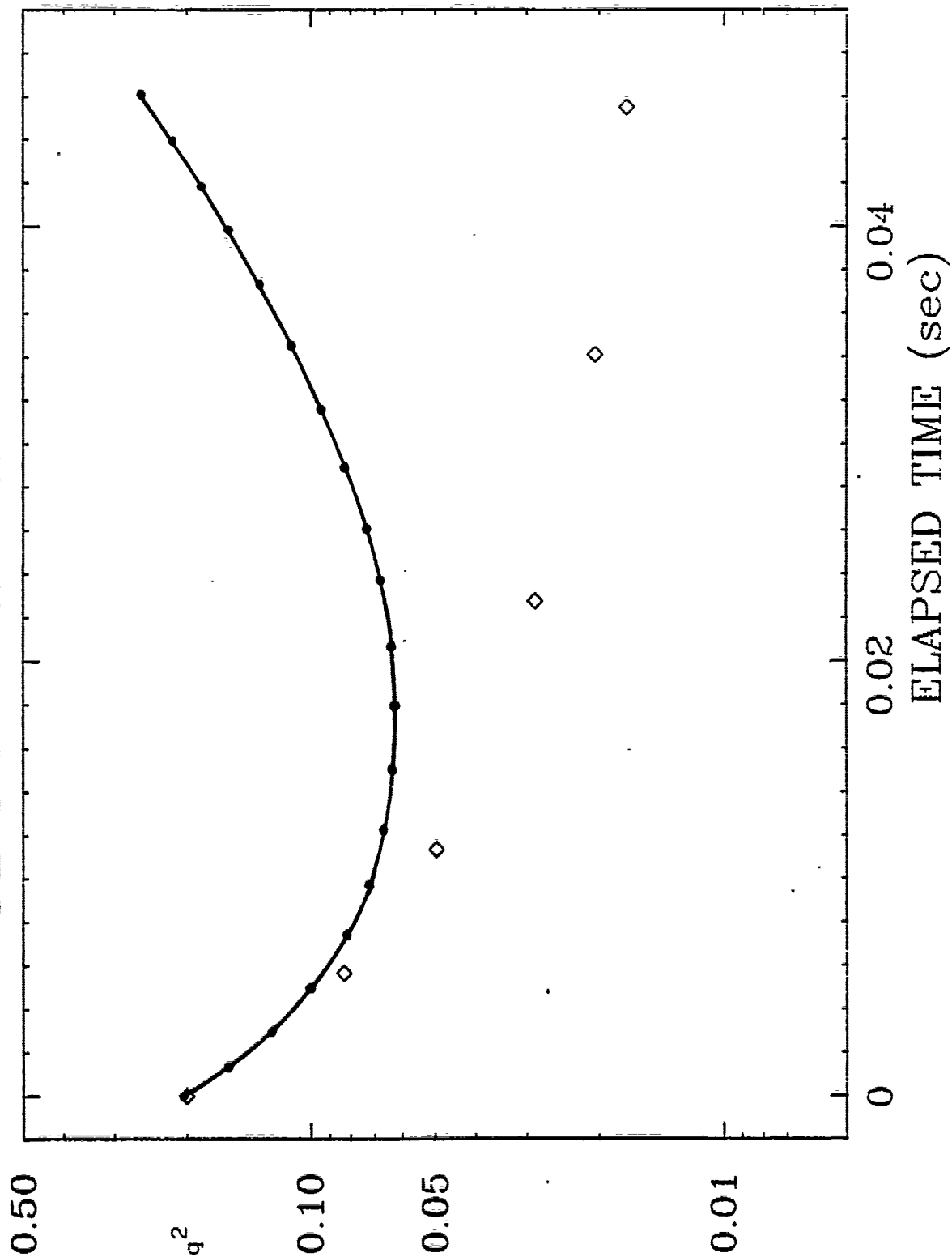


Figure 4. Homogeneous rotating turbulence; $\Omega = 80 \text{ sec}^{-1}$.

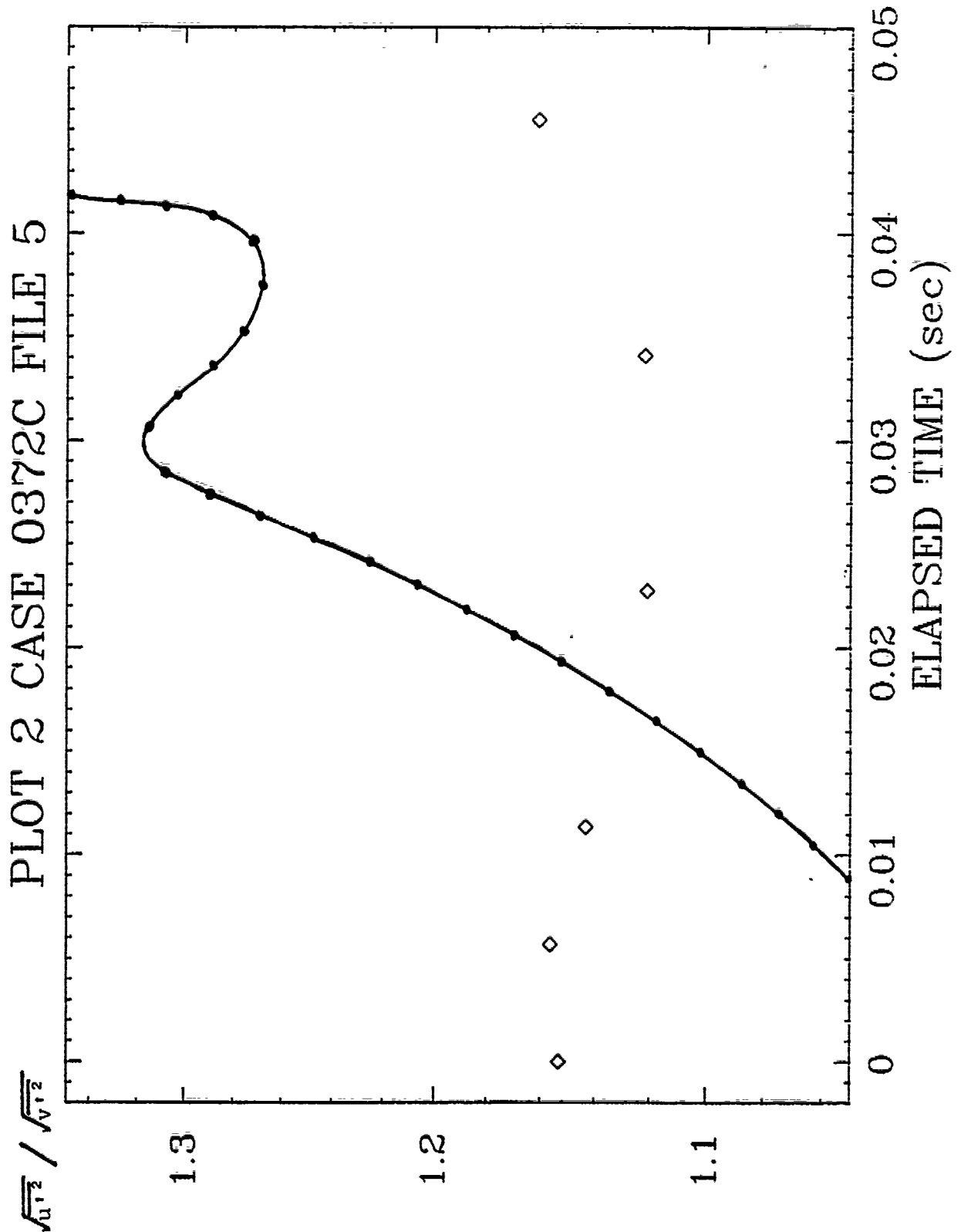


Figure 5. Homogeneous rotating turbulence; $\Omega = 80 \text{ sec}^{-1}$.

THE 1980-81 AFOSR-HTTM-STANFORD CONFERENCE ON COMPLEX TURBULENT FLOWS:
COMPARISON OF COMPUTATION AND EXPERIMENT

PLOT 1 CASE 0374A FILE 11

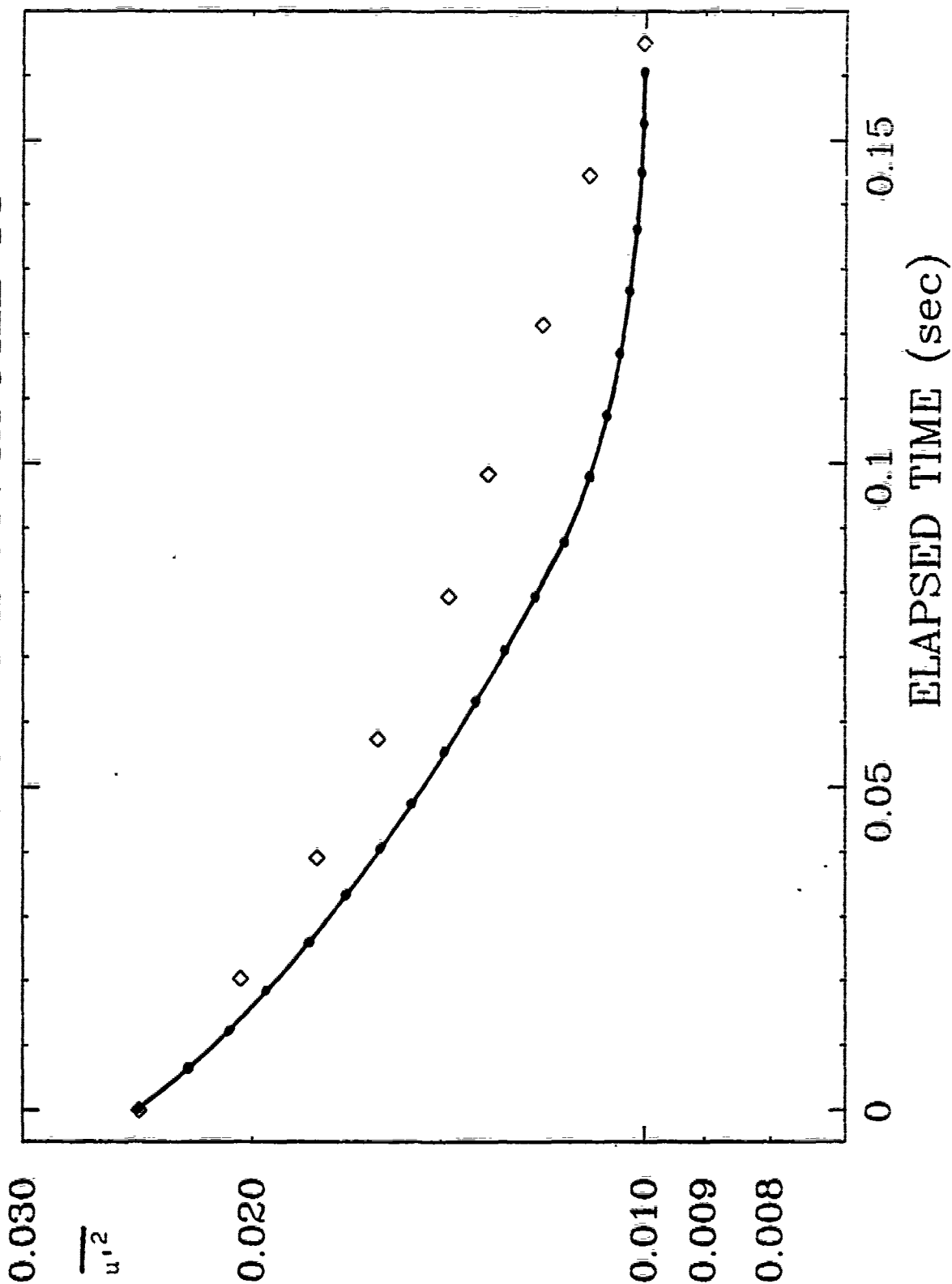


Figure 6. Homogeneous plane strain; strain rate = 9.44 sec^{-1} .

THE 1980-81 AFOSR-HITM-STANFORD CONFERENCE ON COMPLEX TURBULENT FLOWS:
COMPARISON OF COMPUTATION AND EXPERIMENT

PLOT 2 CASE 0374A FILE 11

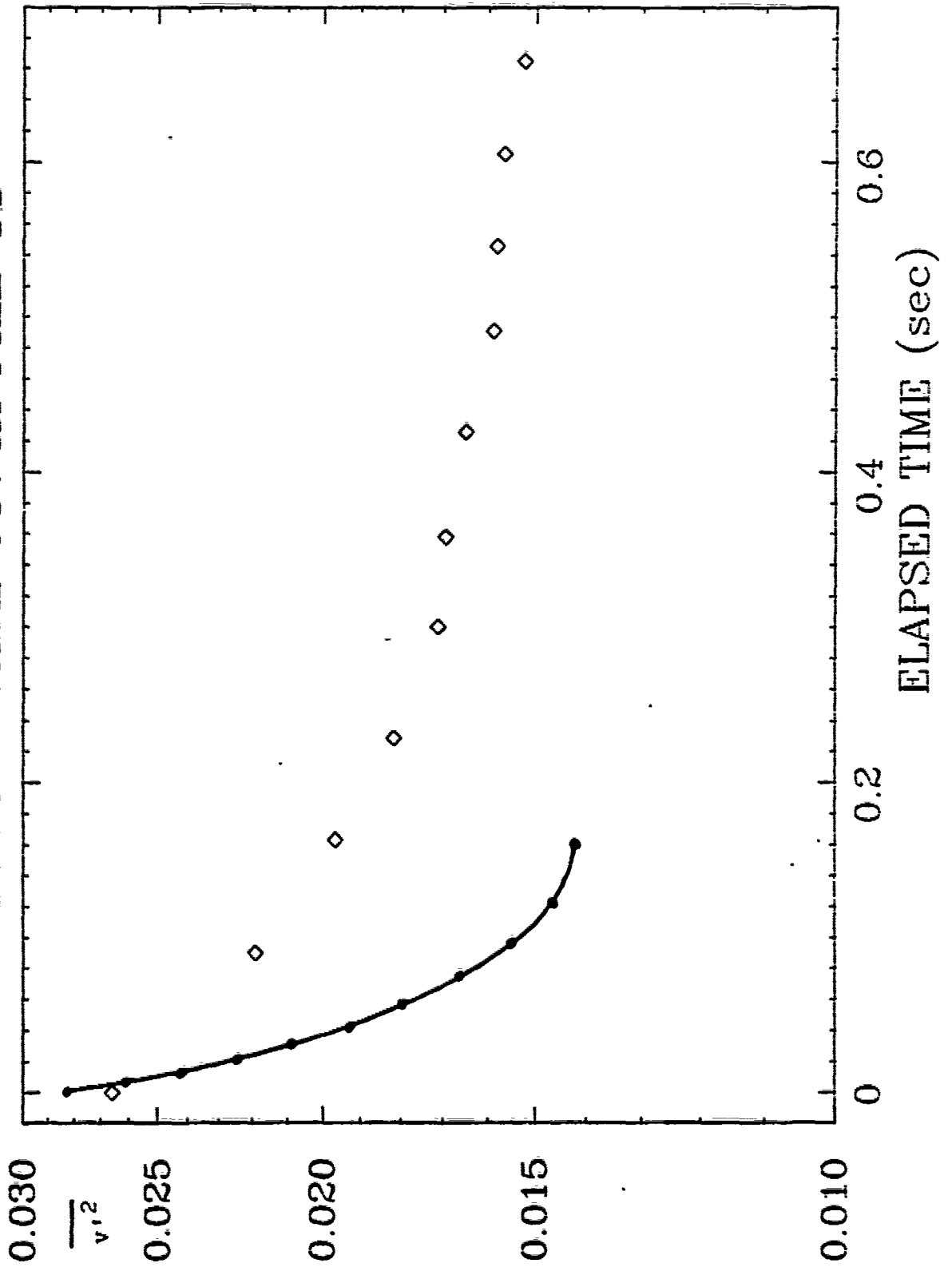


Figure 7. Homogeneous plane strain; strain rate = 9.44 sec^{-1} .

PLOT 3 CASE 0374A FILE 11

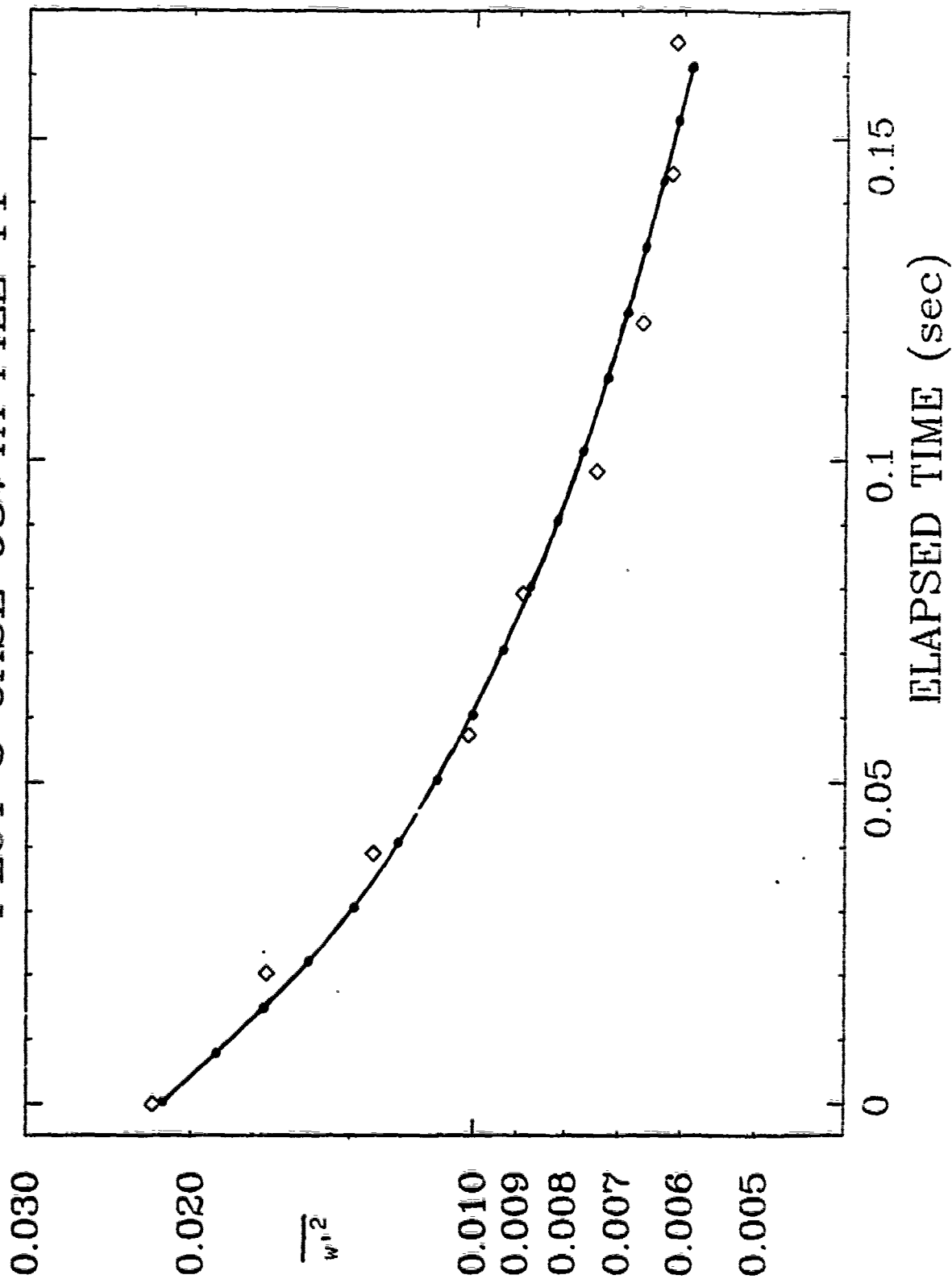


Figure 8. Homogeneous plane strain; strain rate = 9.44 sec^{-1} .

PLOT 1 CASE 0374B FILE 12

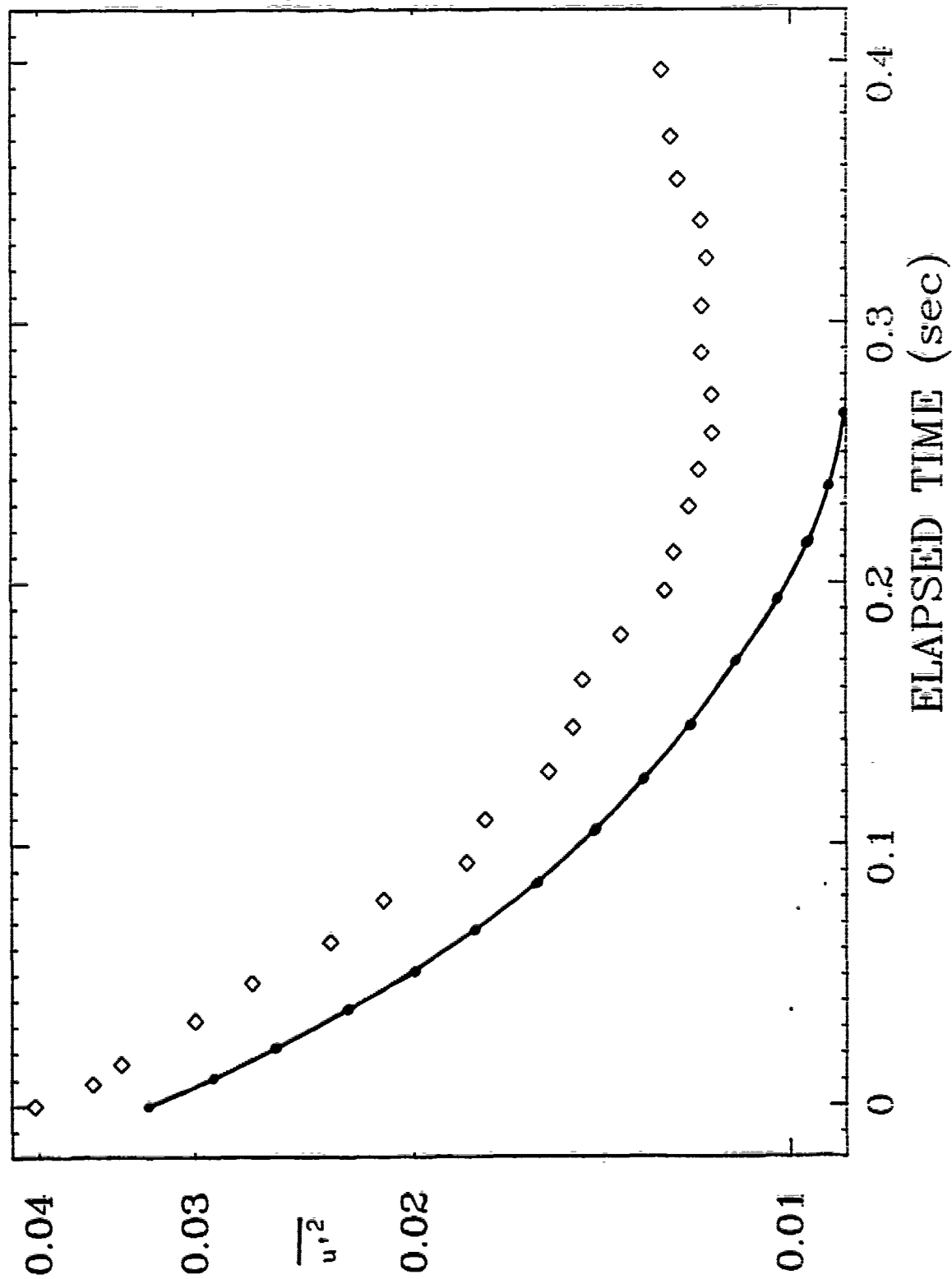


Figure 9. Homogeneous plane strain; strain rate = 4.45 sec^{-1} .

PLOT 2 CASE 0374B FILE 12

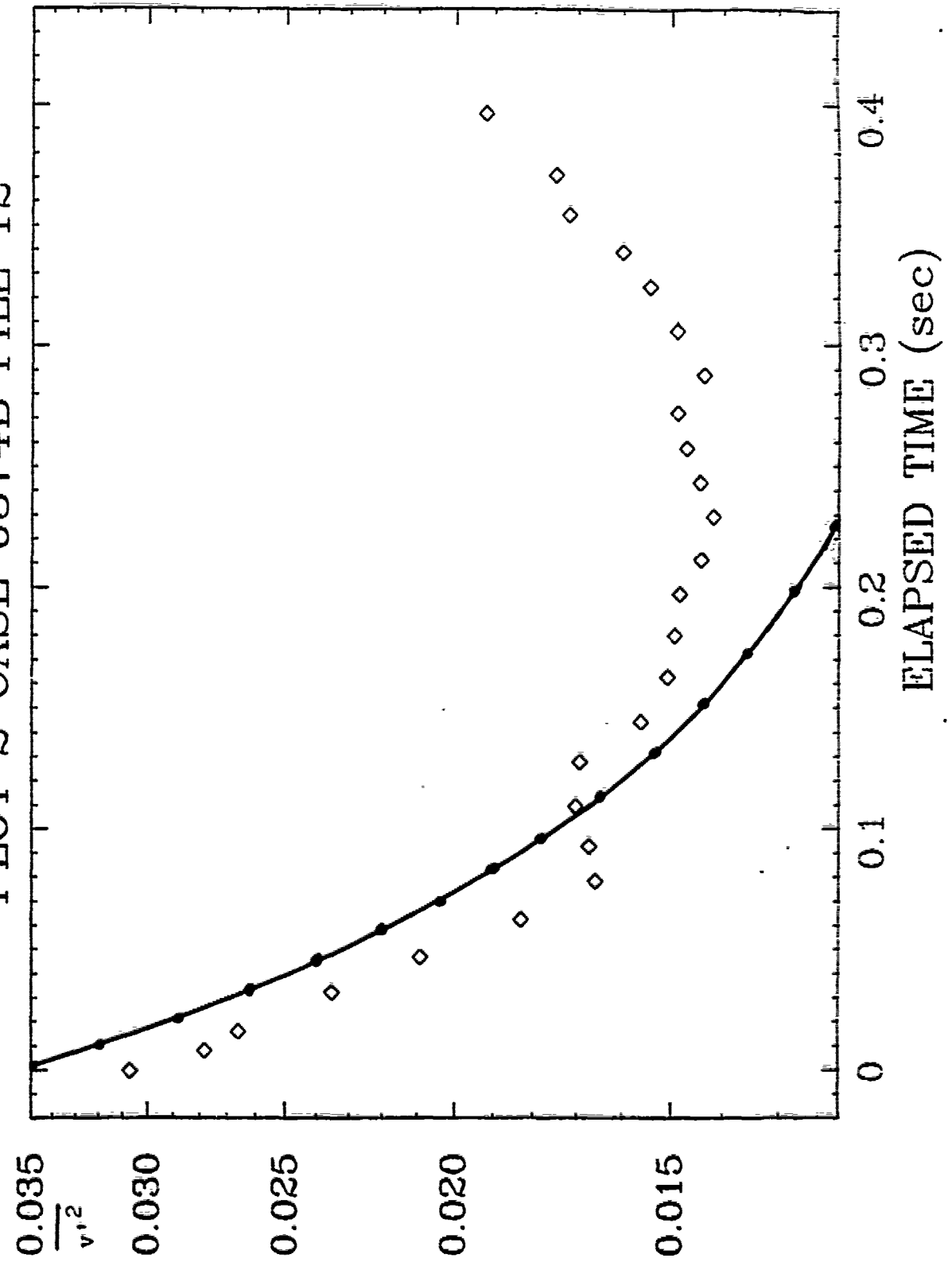


Figure 10. Homogeneous plane strain; strain rate = 4.45 sec^{-1} .

PLOT 3 CASE 0374B FILE 12

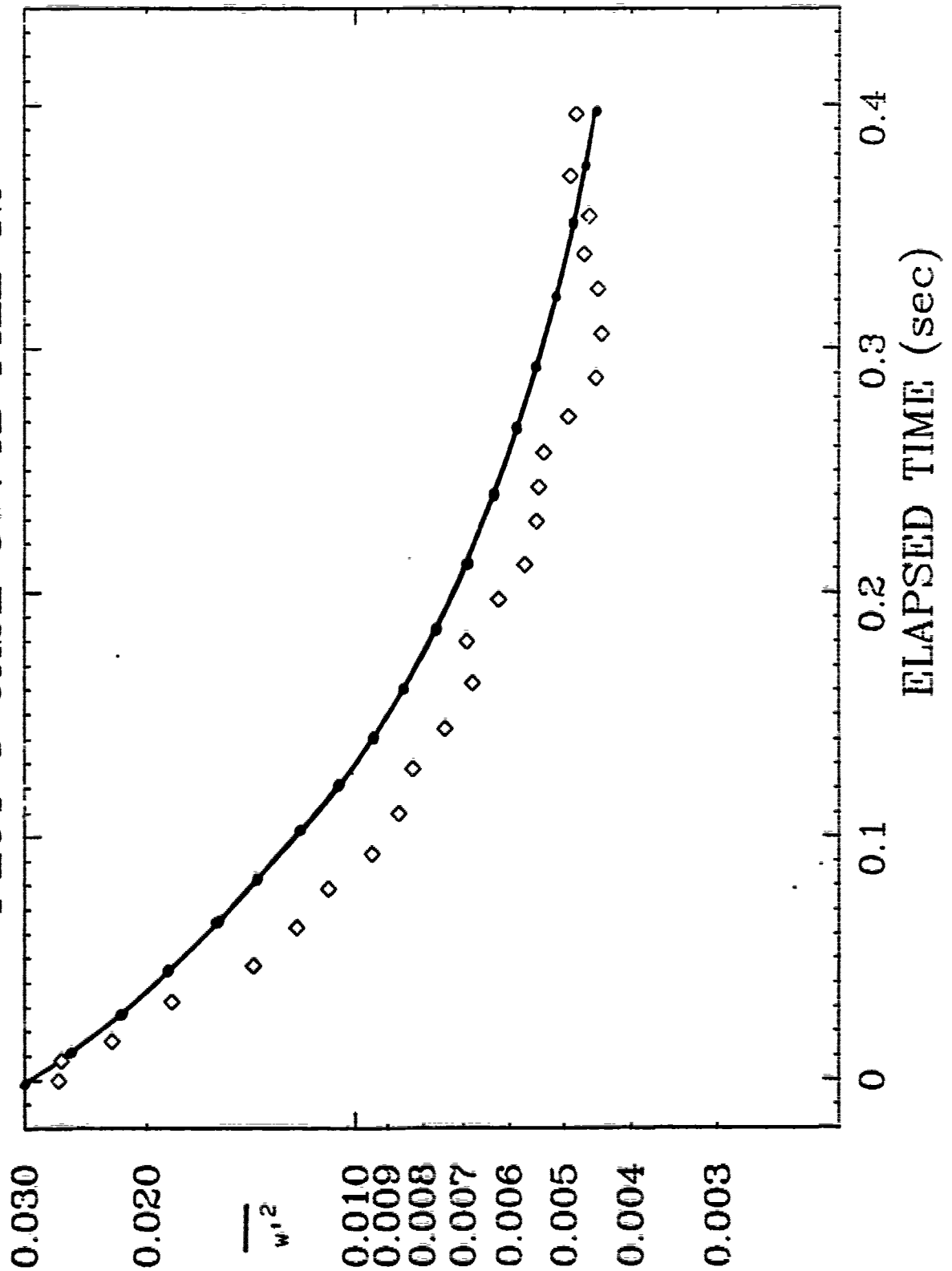


Figure 11. Homogeneous plane strain; strain rate = 4.45 sec^{-1} .

PLOT 1 CASE 0376A FILE 18

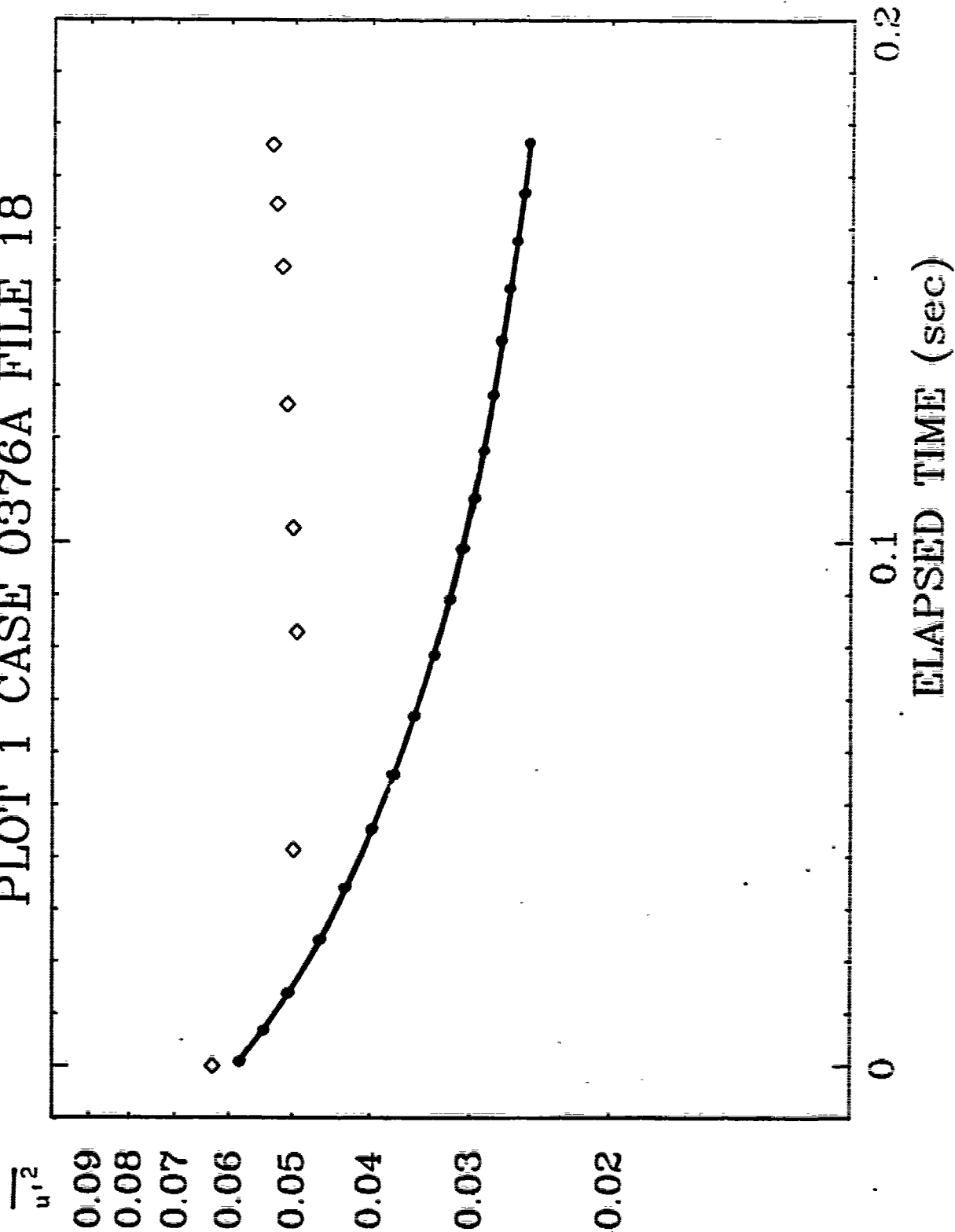


Figure 12. Homogeneous shear; shearing rate = 12.9 sec^{-1} .

THE 1980-81 APOSR-HTTM-STANFORD CONFERENCE ON COMPLEX TURBULENT FLOWS:
 COMPARISON OF COMPUTATION AND EXPERIMENT

PLOT 2 CASE 0376A FILE 18

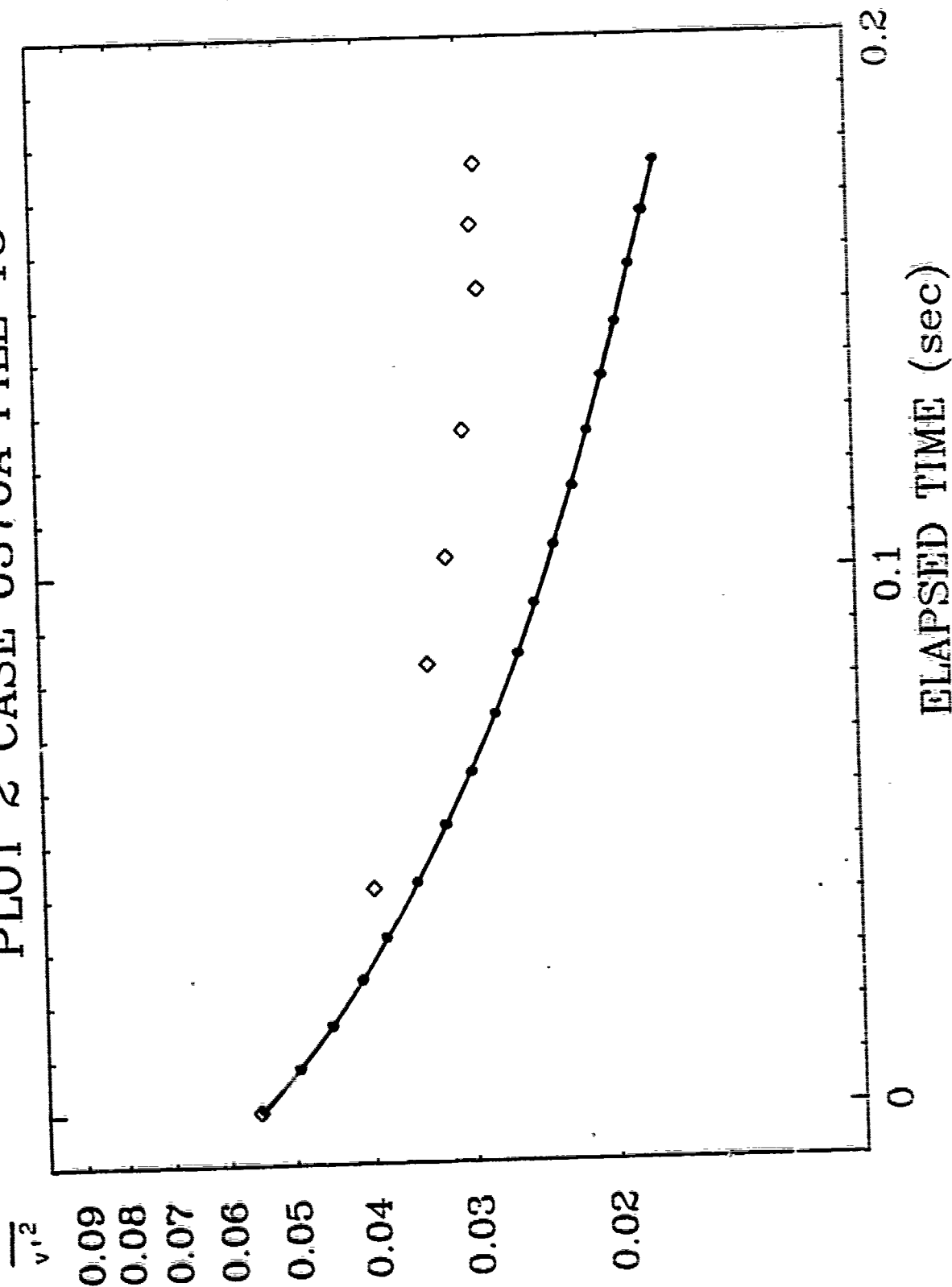


Figure 13. Homogeneous shear; shearing rate = 12.9 sec^{-1} .

THE 1980-81 AFOSR-HTTM-STANFORD CONFERENCE ON COMPLEX TURBULENT FLOWS:
COMPARISON OF COMPUTATION AND EXPERIMENT

PLOT 3 CASE 0376A FILE 18

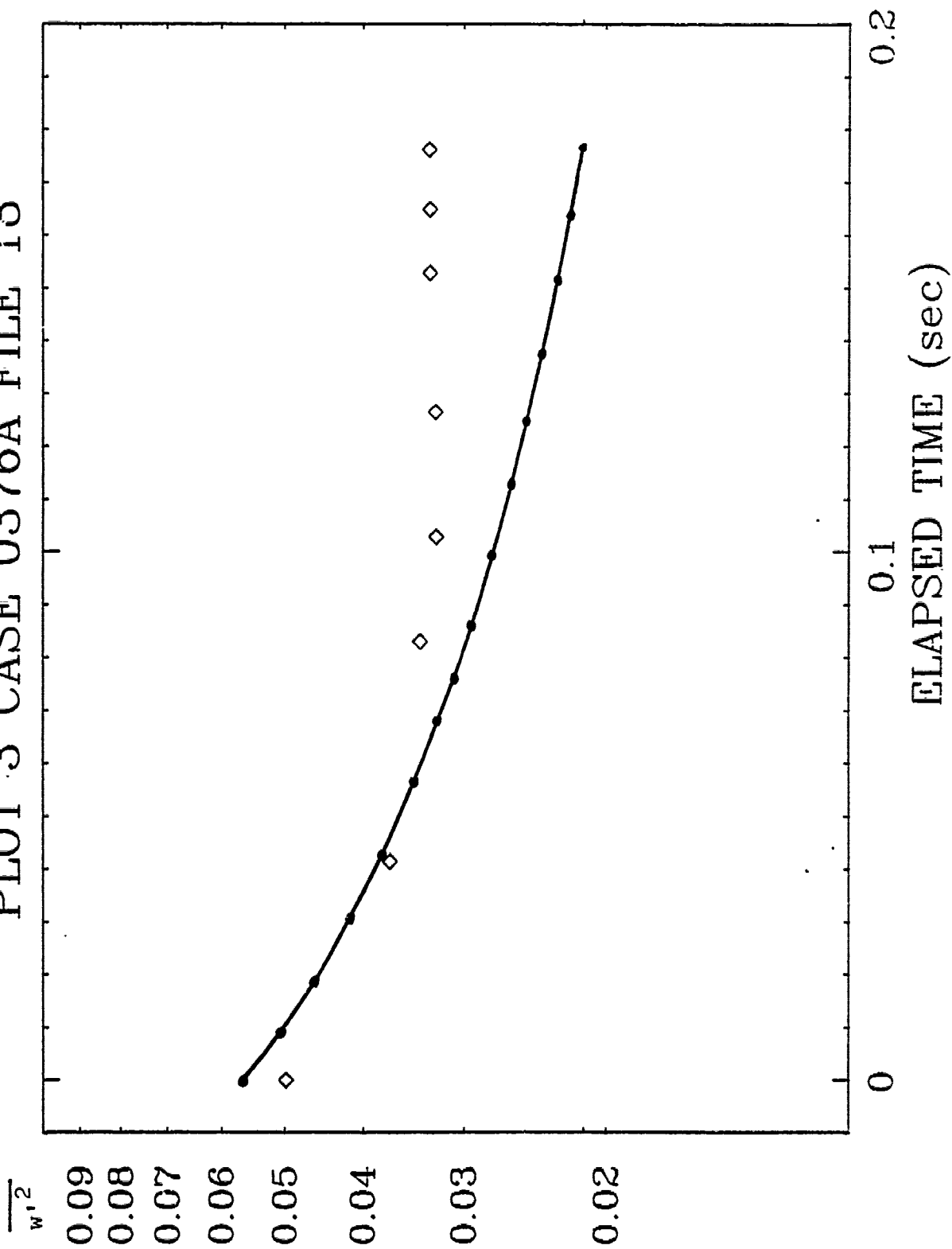


Figure 14. Homogeneous shear; shearing rate = 12.9 sec^{-1} .

PLOT 4 CASE 0376A FILE 18

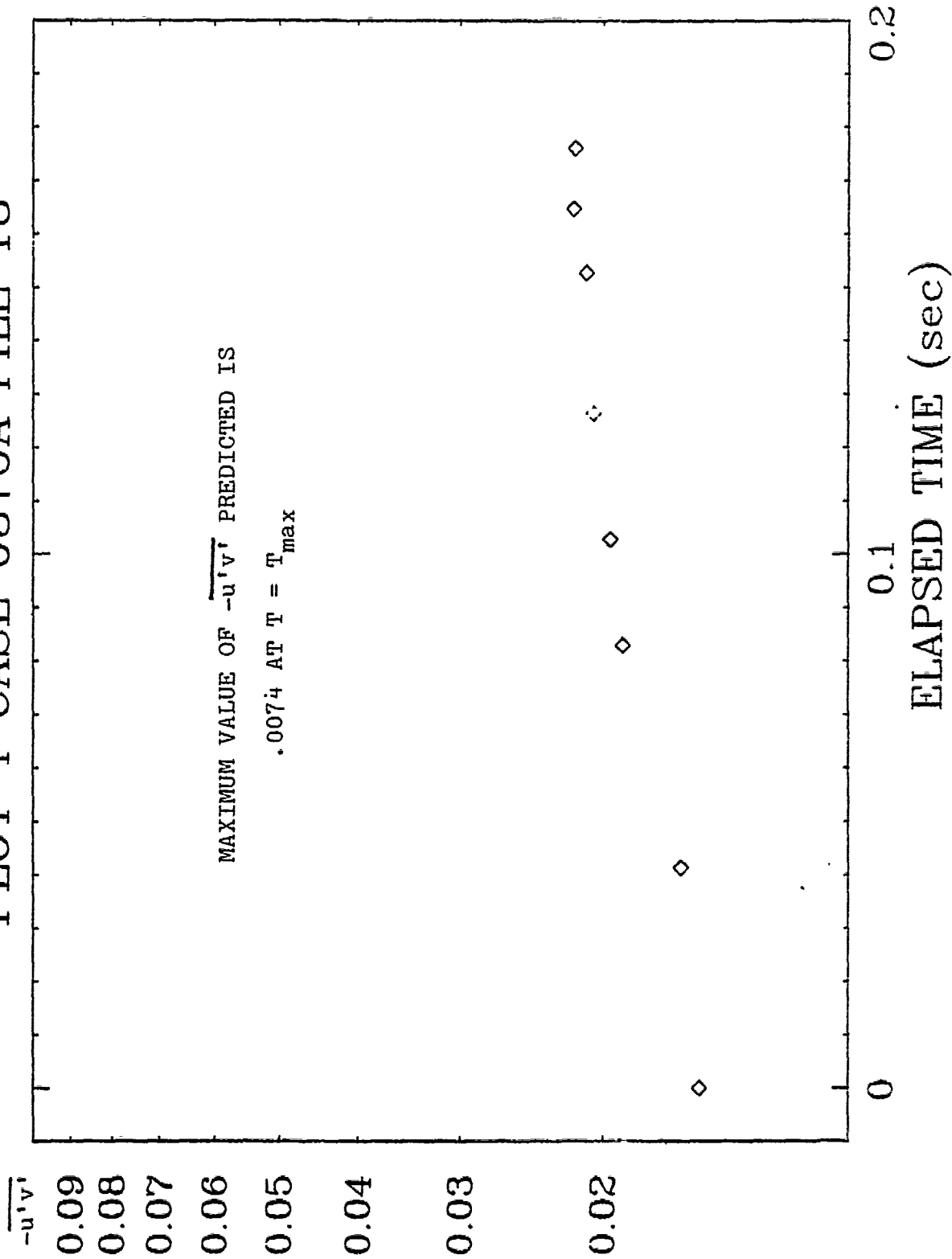


Figure 15. Homogeneous shear; shearing rate = 12.9 sec^{-1} .

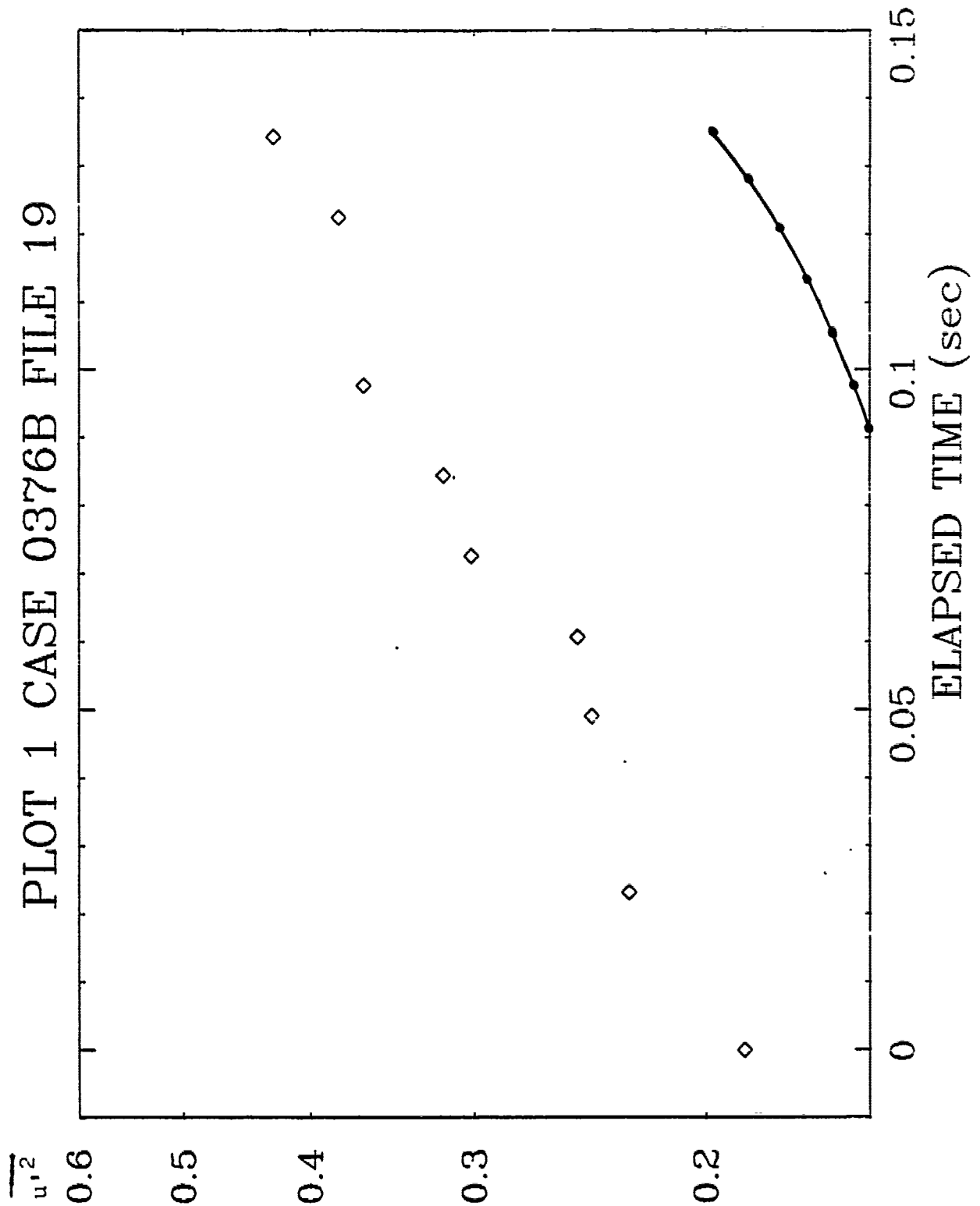


Figure 16, Homogeneous shear; shearing rate = 48 sec^{-1} .

PLOT 2 CASE 0376B FILE 19

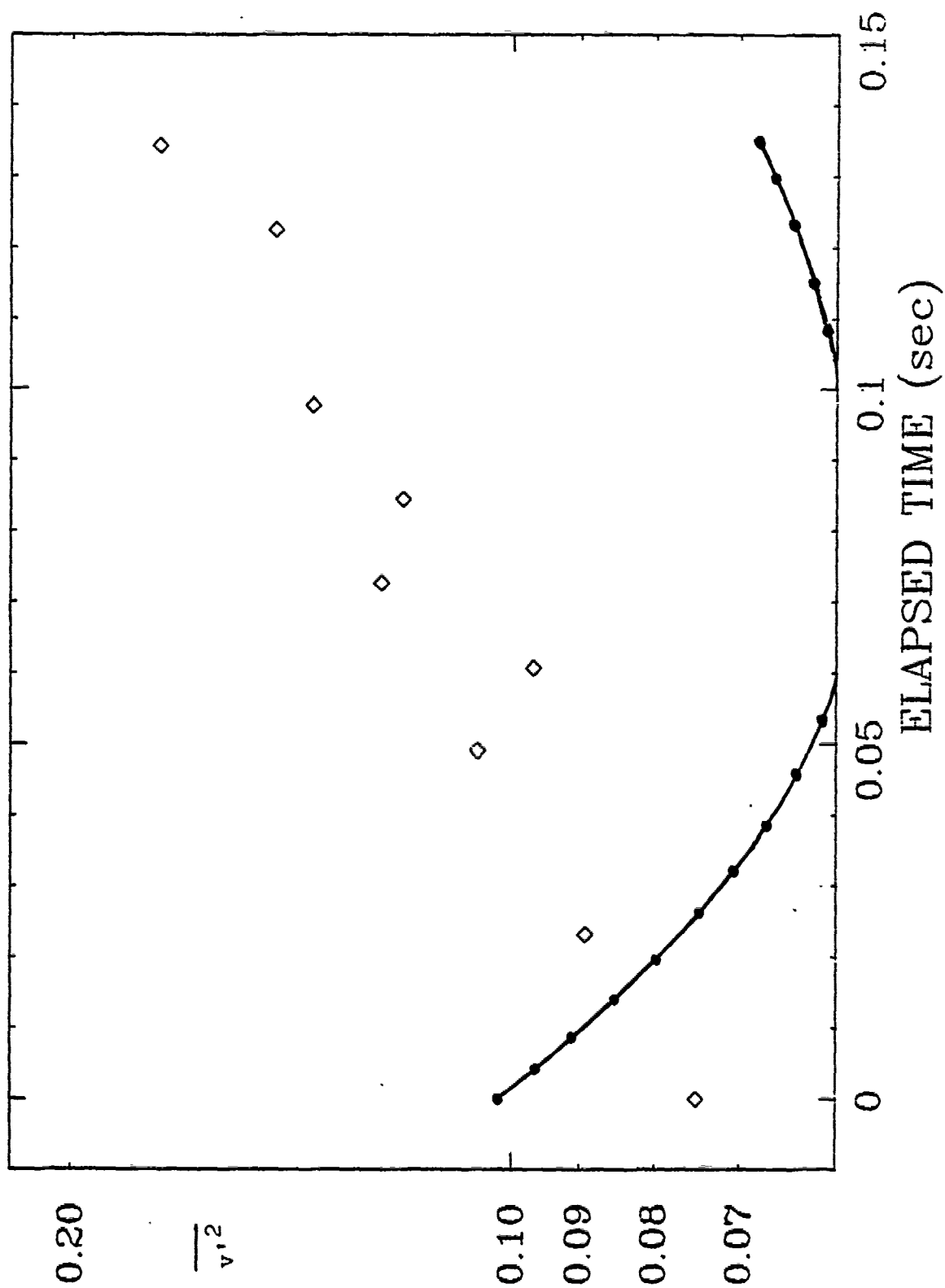


Figure 17. Homogeneous shear; shearing rate = 48 sec^{-1} .

PLOT 3 CASE 0376B FILE 19

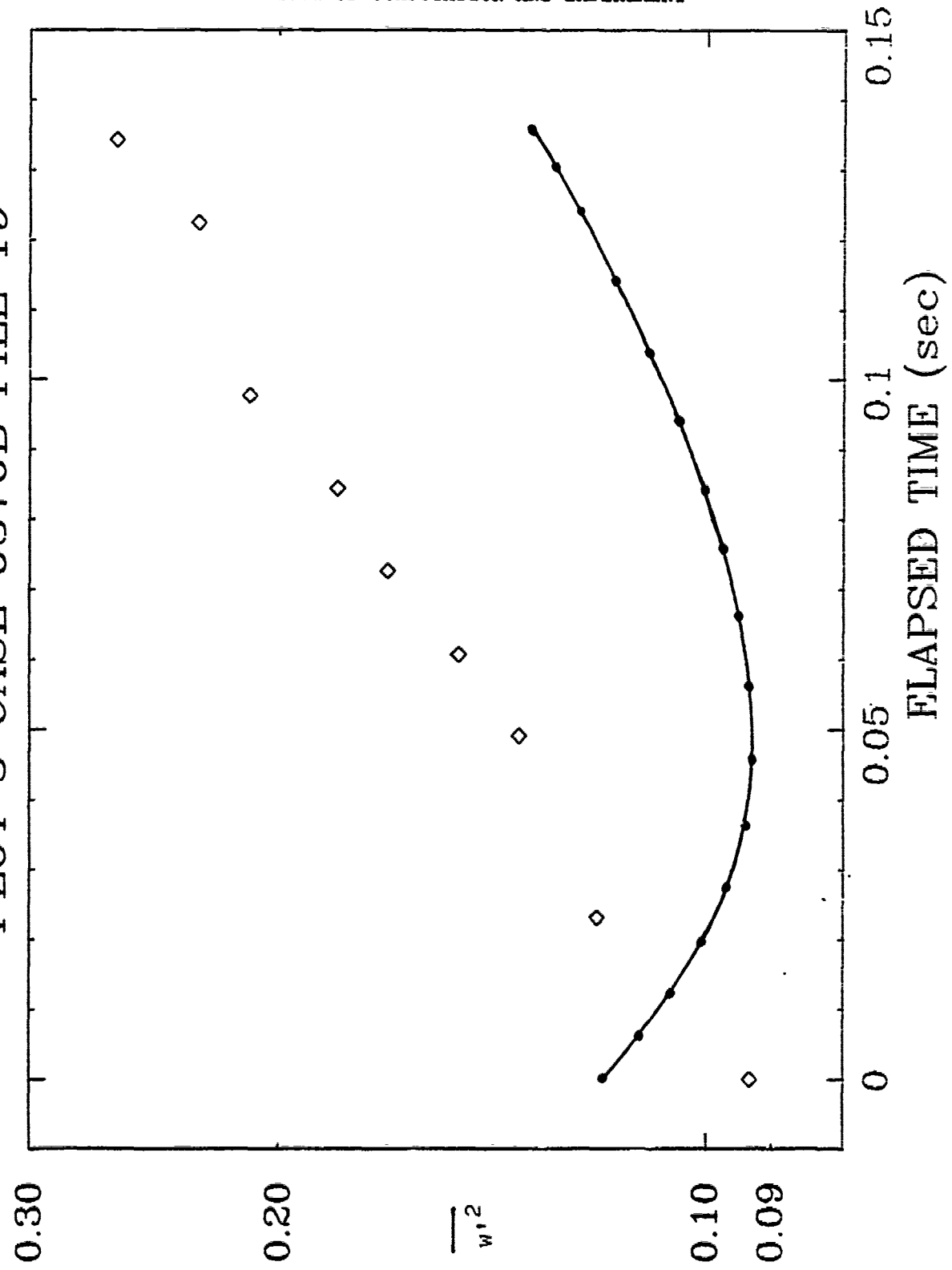


Figure 18. Homogeneous shear; shearing rate = 48 sec^{-1} .

PLOT 4 CASE 0376B FILE 19

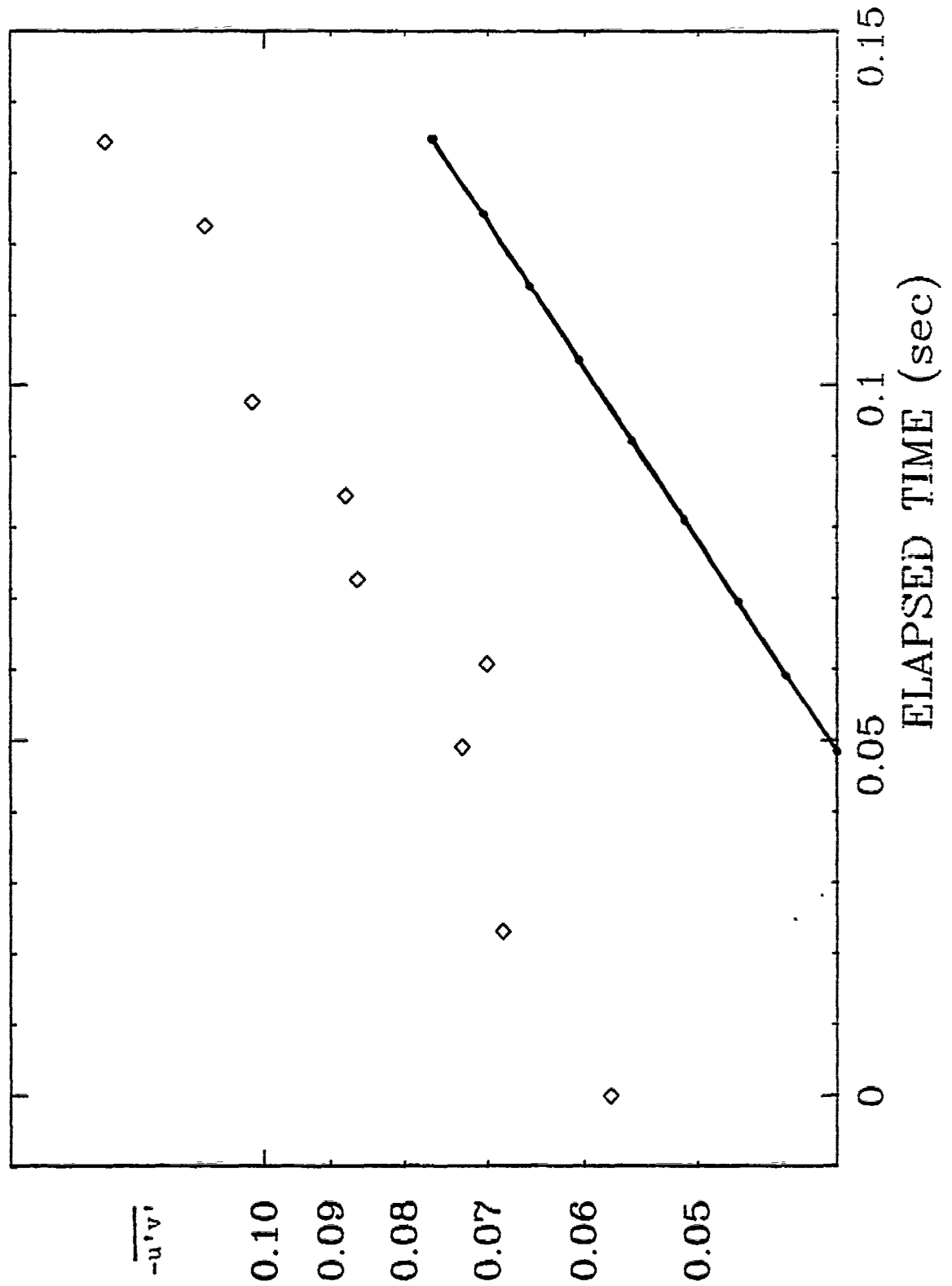


Figure 19. Homogeneous shear; shearing rate = 48 sec^{-1} .

PLOT 1 CASE 0612 FILE 25

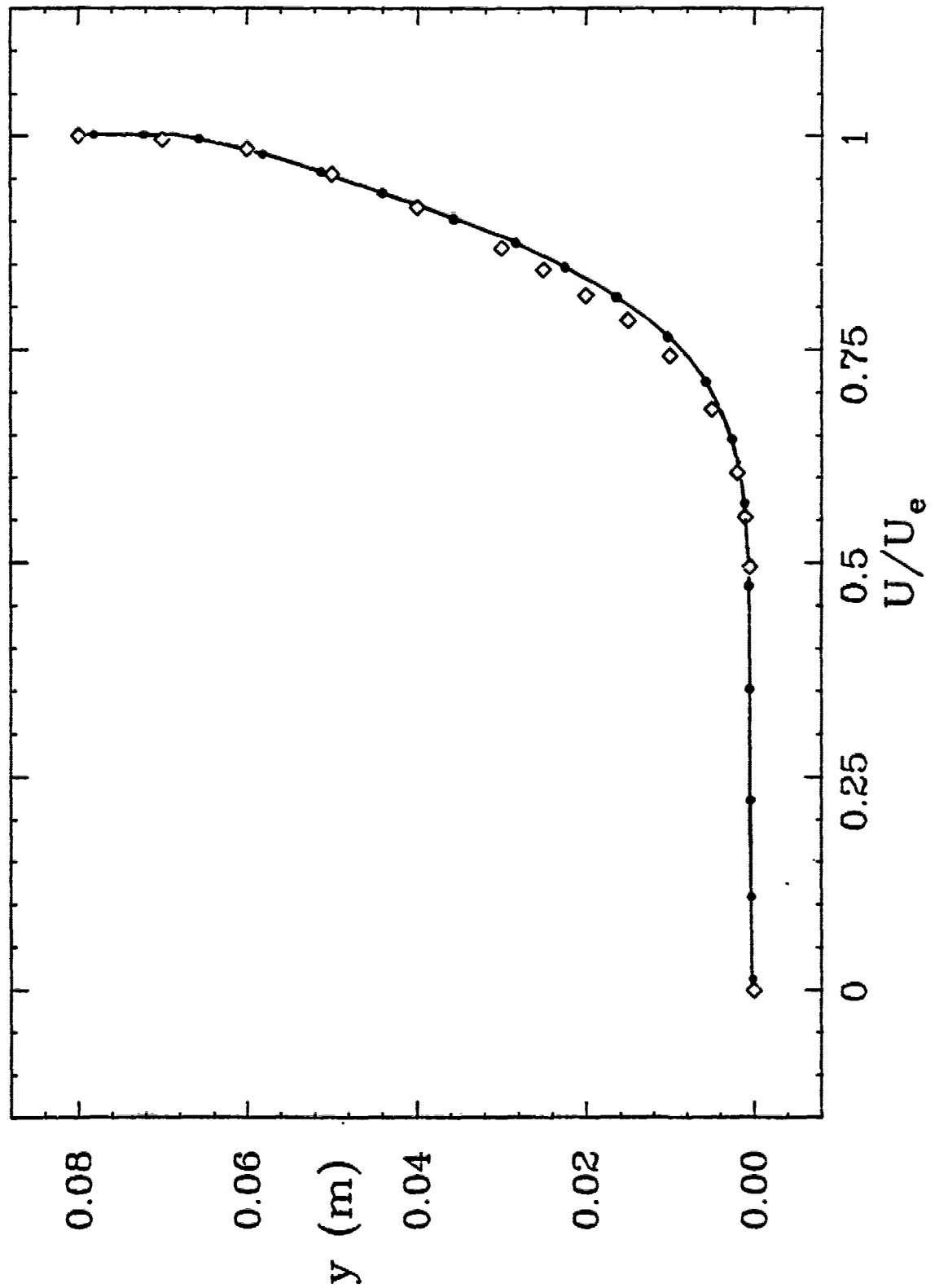


Figure 20. Incompressible flat-plate boundary layer.

PLOT 2 CASE 0612, FILE 2

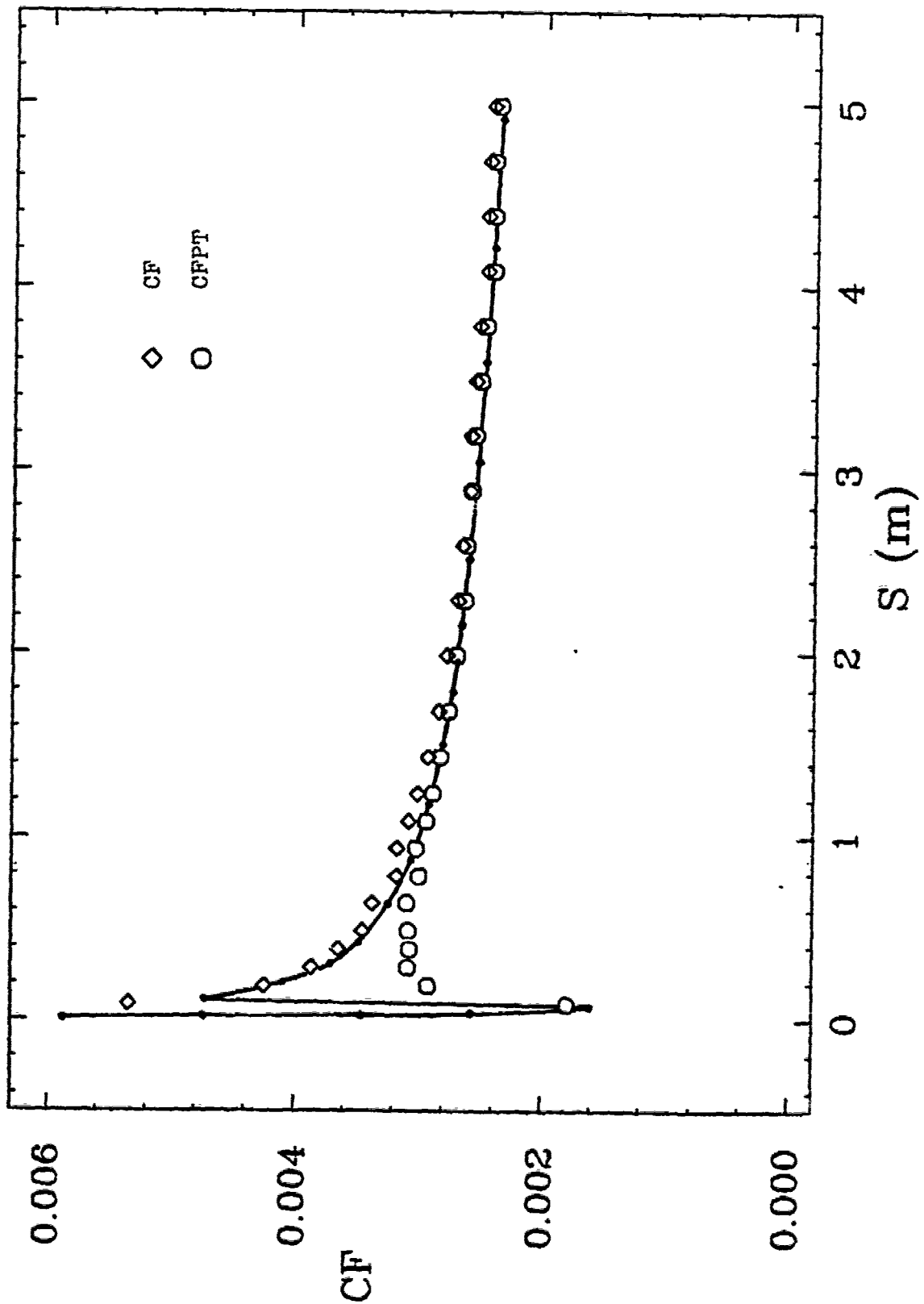


Figure 21. Incompressible flat-plate boundary layer.

PLOT 3 CASE 0612 FILE 2

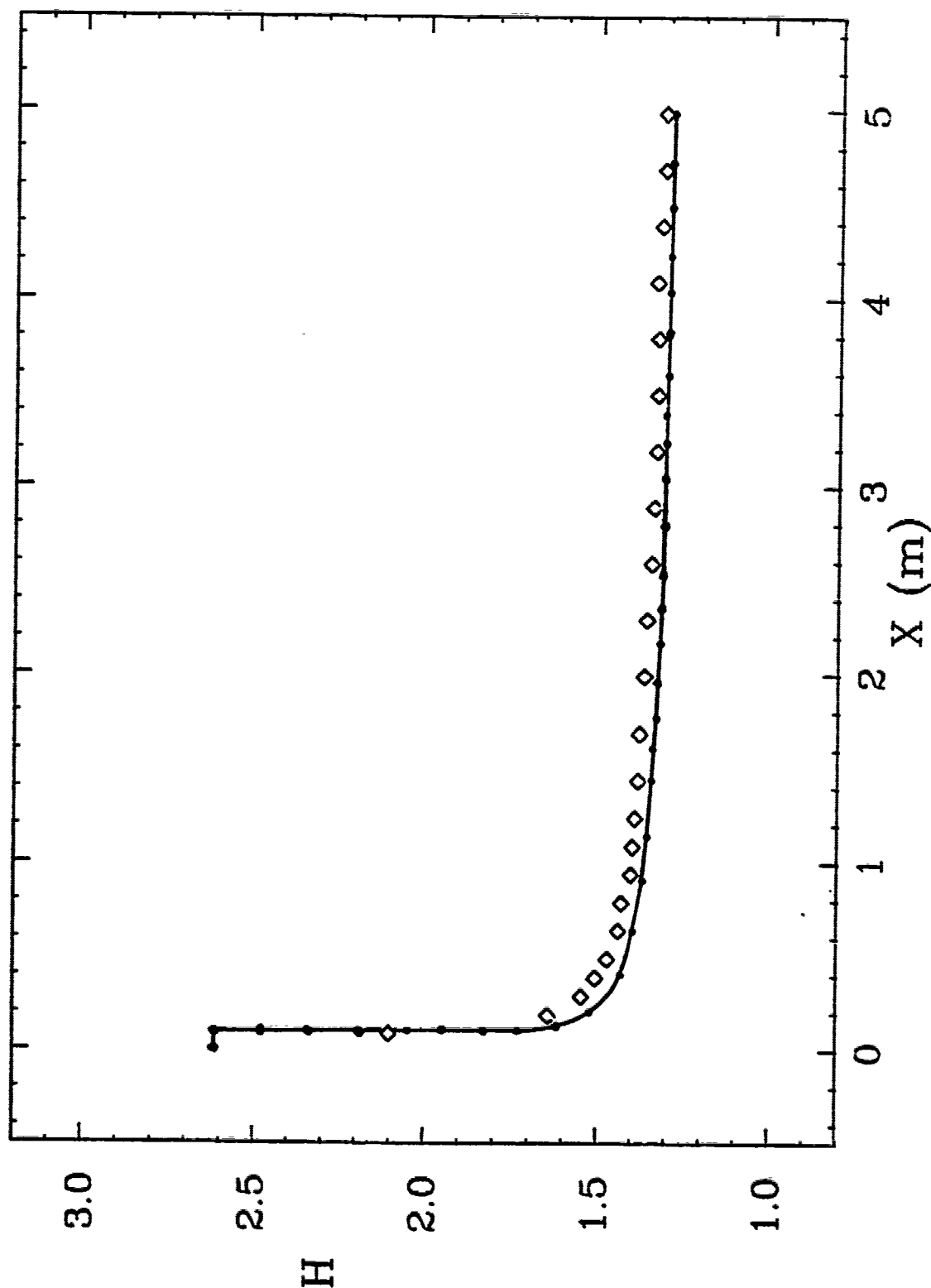


Figure 22. Incompressible flat-plate boundary layer.

THE 1980-81 AFOSR-HITM-STANFORD CONFERENCE ON COMPLEX TURBULENT FLOWS:
COMPARISON OF COMPUTATION AND EXPERIMENT

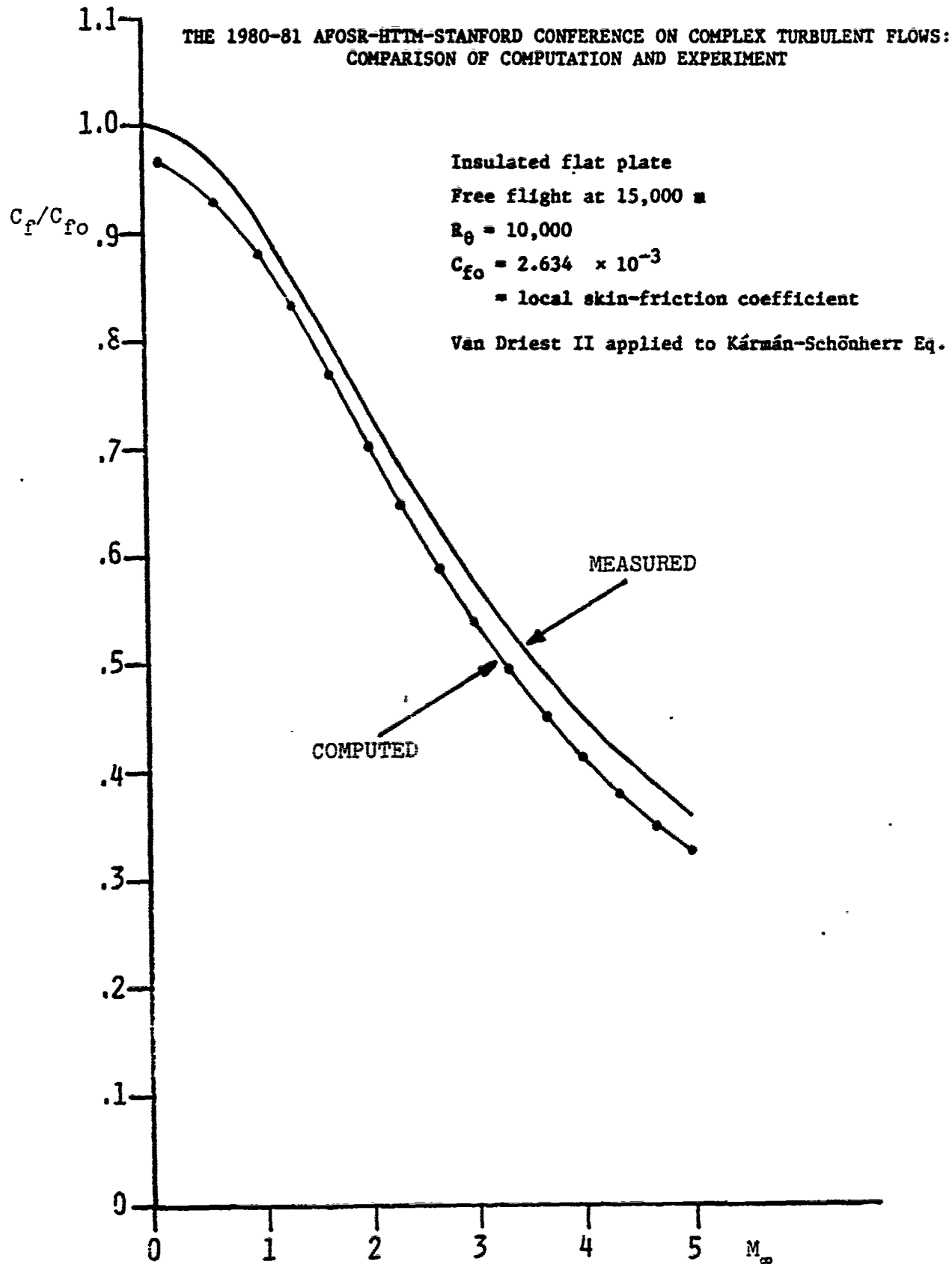


Figure 23. Effect of Mach number on FPBL skin friction.

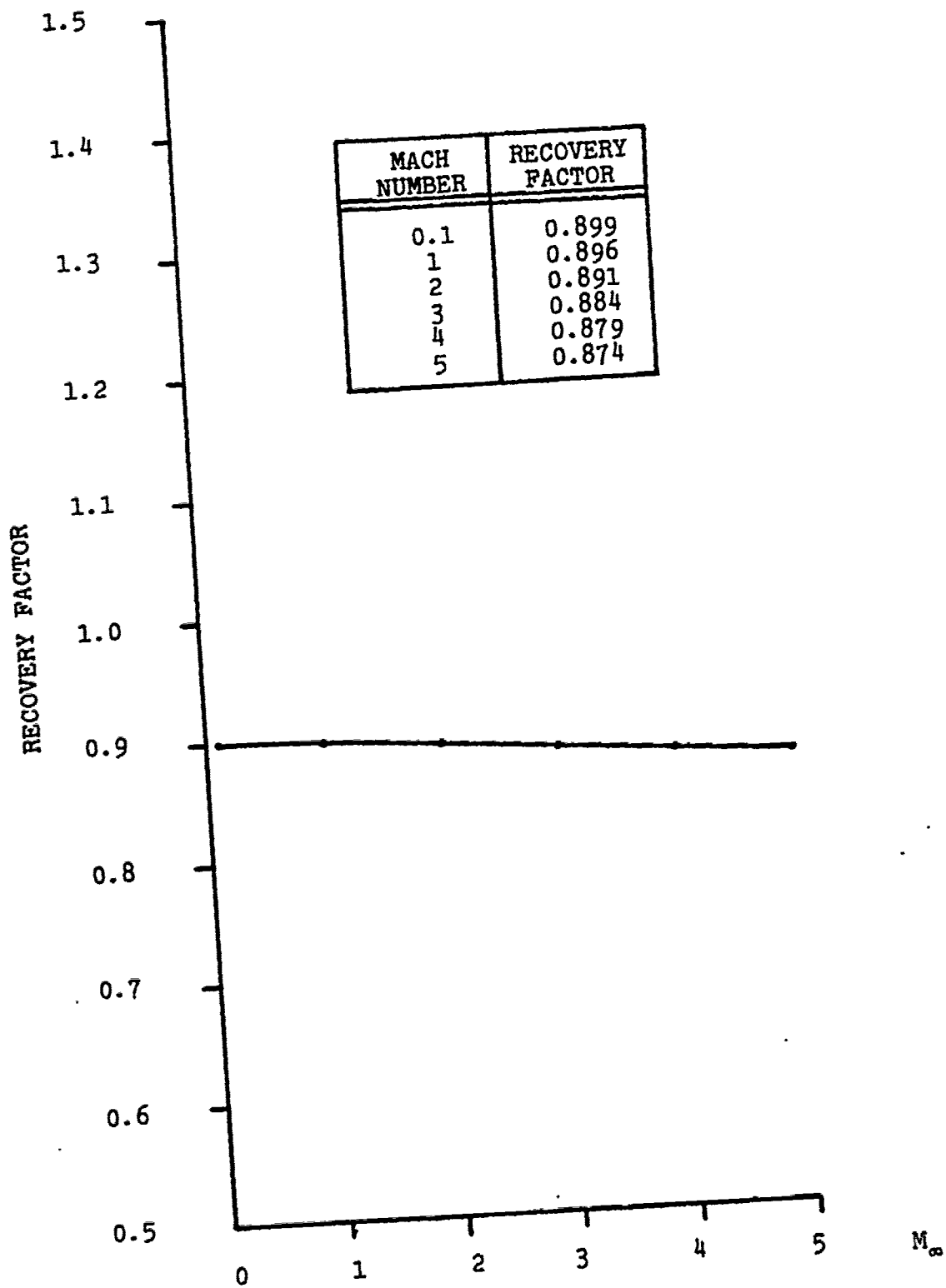


Figure 24. Computed recovery factor for a flat-plate boundary layer as a function of Mach number.

THE 1980-81 AFOSR-HTTM-STANFORD CONFERENCE ON COMPLEX TURBULENT FLOWS:
COMPARISON OF COMPUTATION AND EXPERIMENT

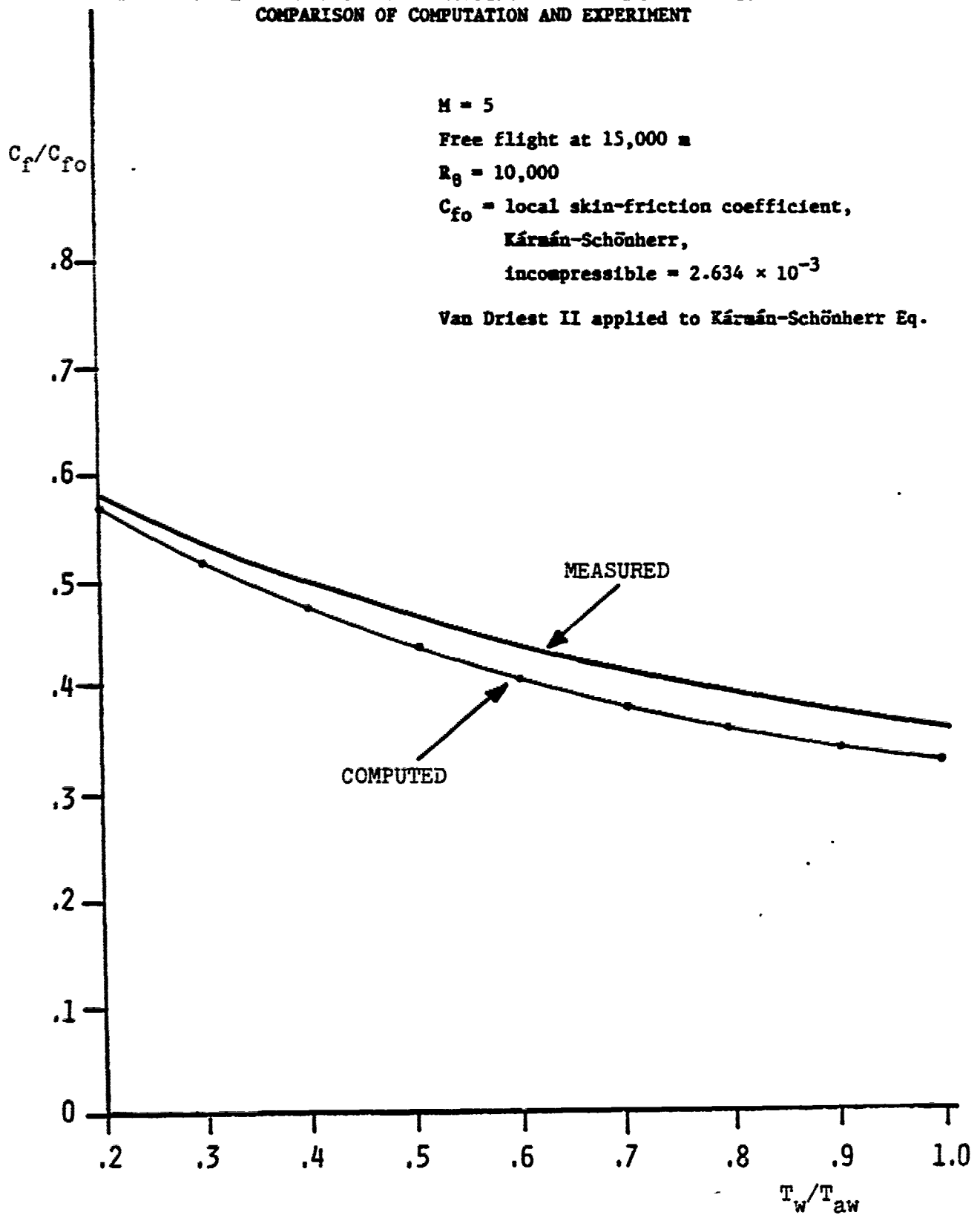


Figure 25. Effect of surface cooling on FPBL skin friction.

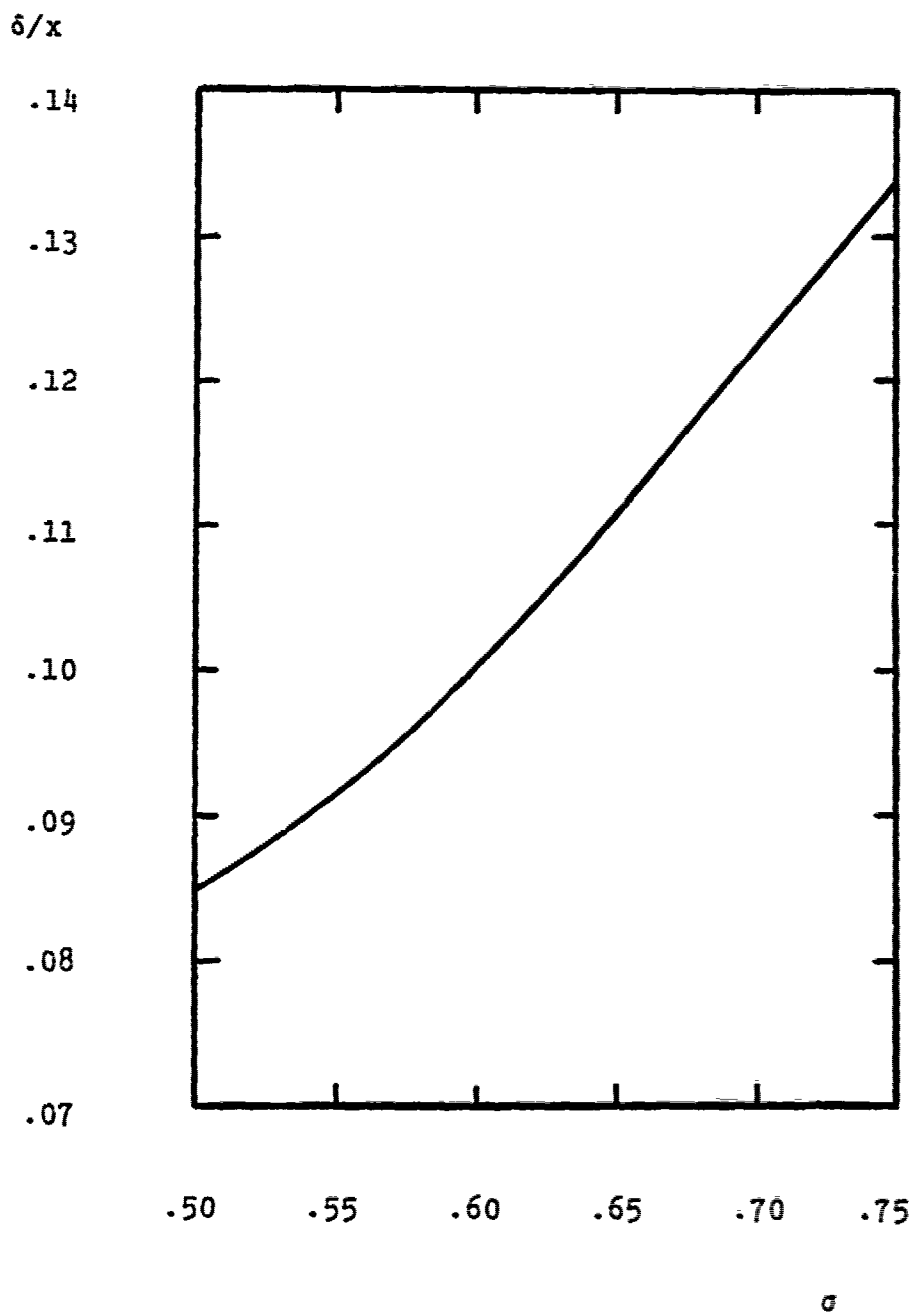


Figure 26. Computed effect of turbulence-model closure coefficient σ ($=\sigma^*$) on mixing layer spreading rate.

δ/x

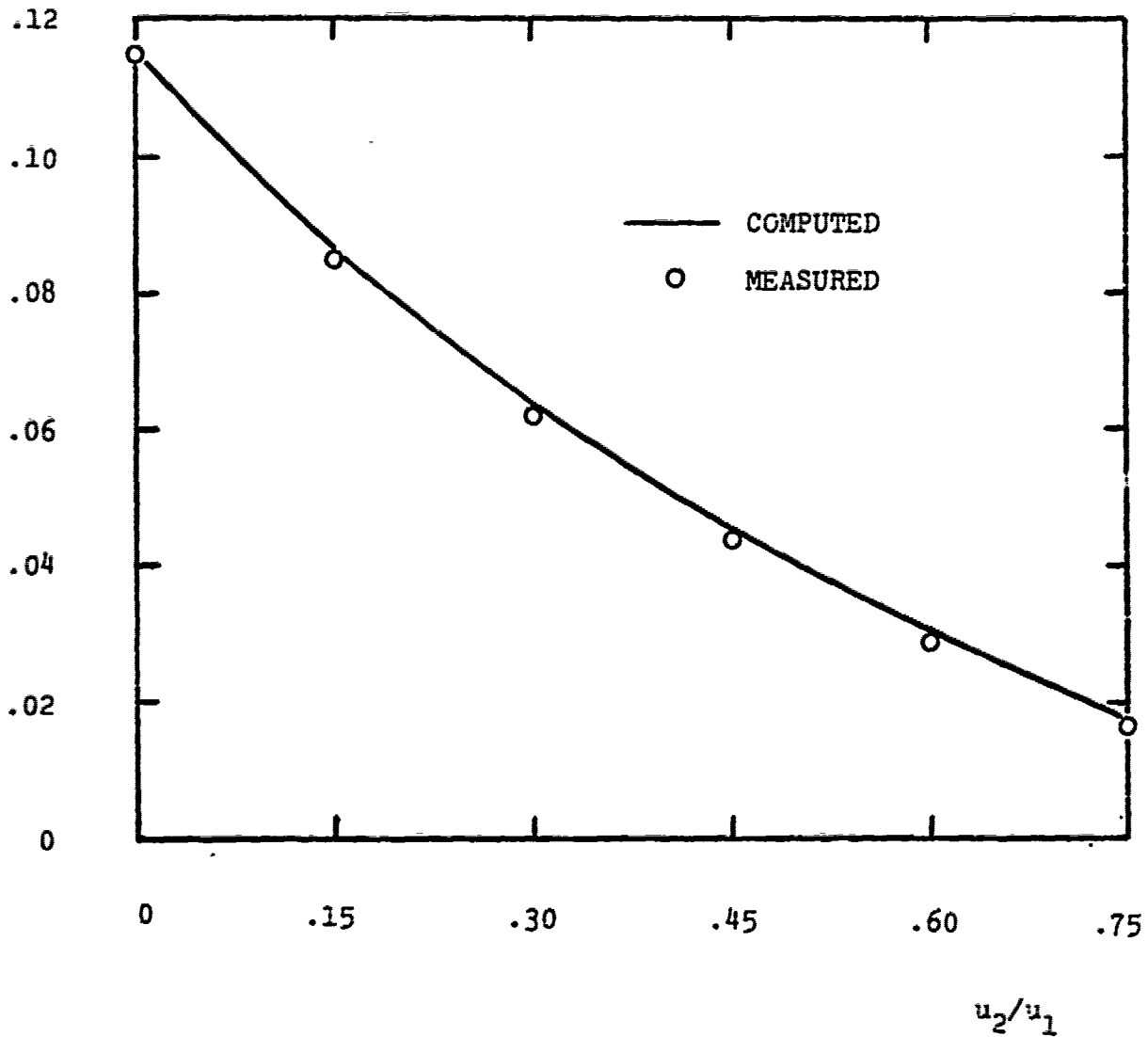


Figure 27. Variation with velocity ratio of asymptotic spreading rate for an incompressible mixing layer.

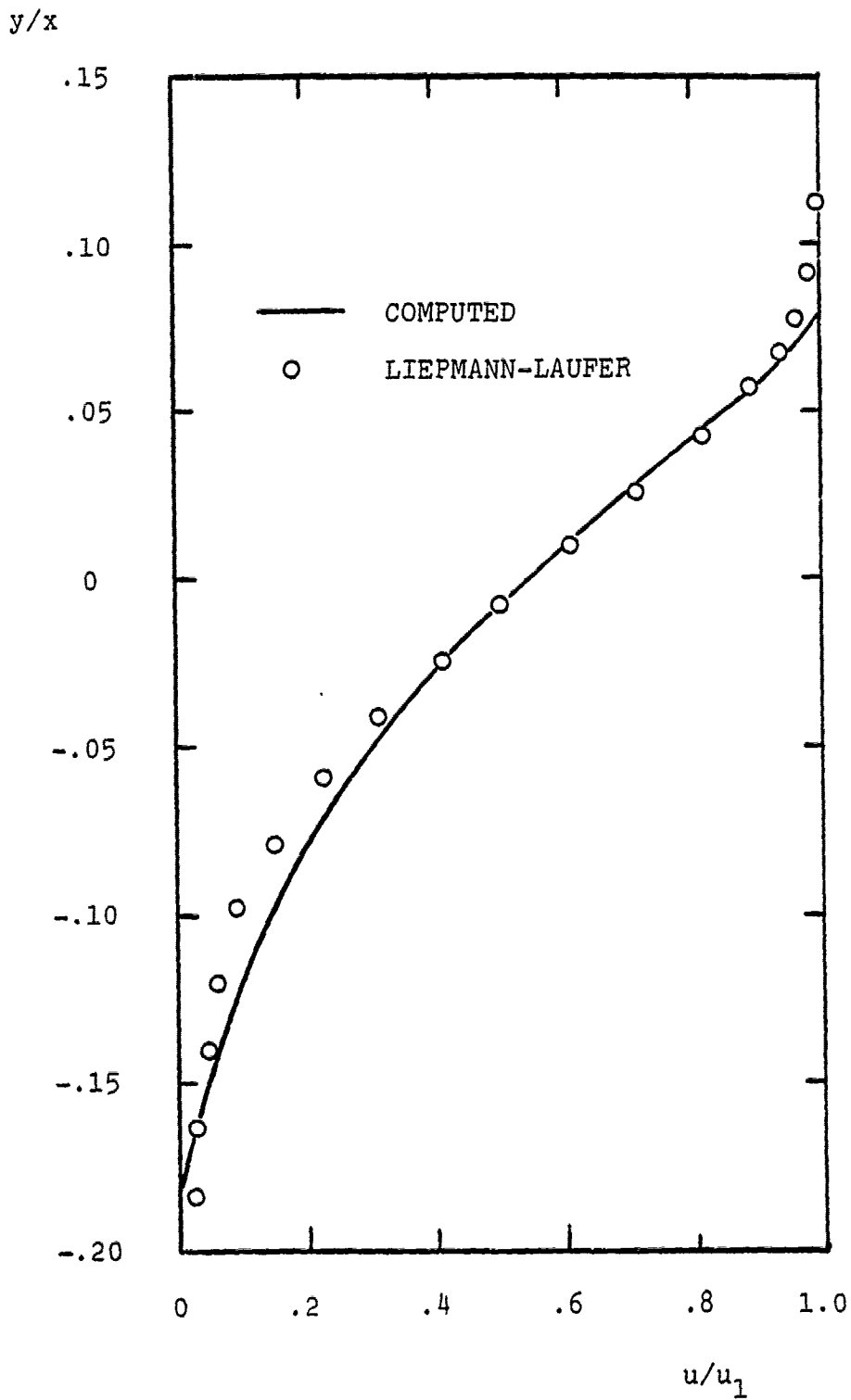


Figure 28. Comparison of computed and measured velocity profiles for an incompressible mixing layer.

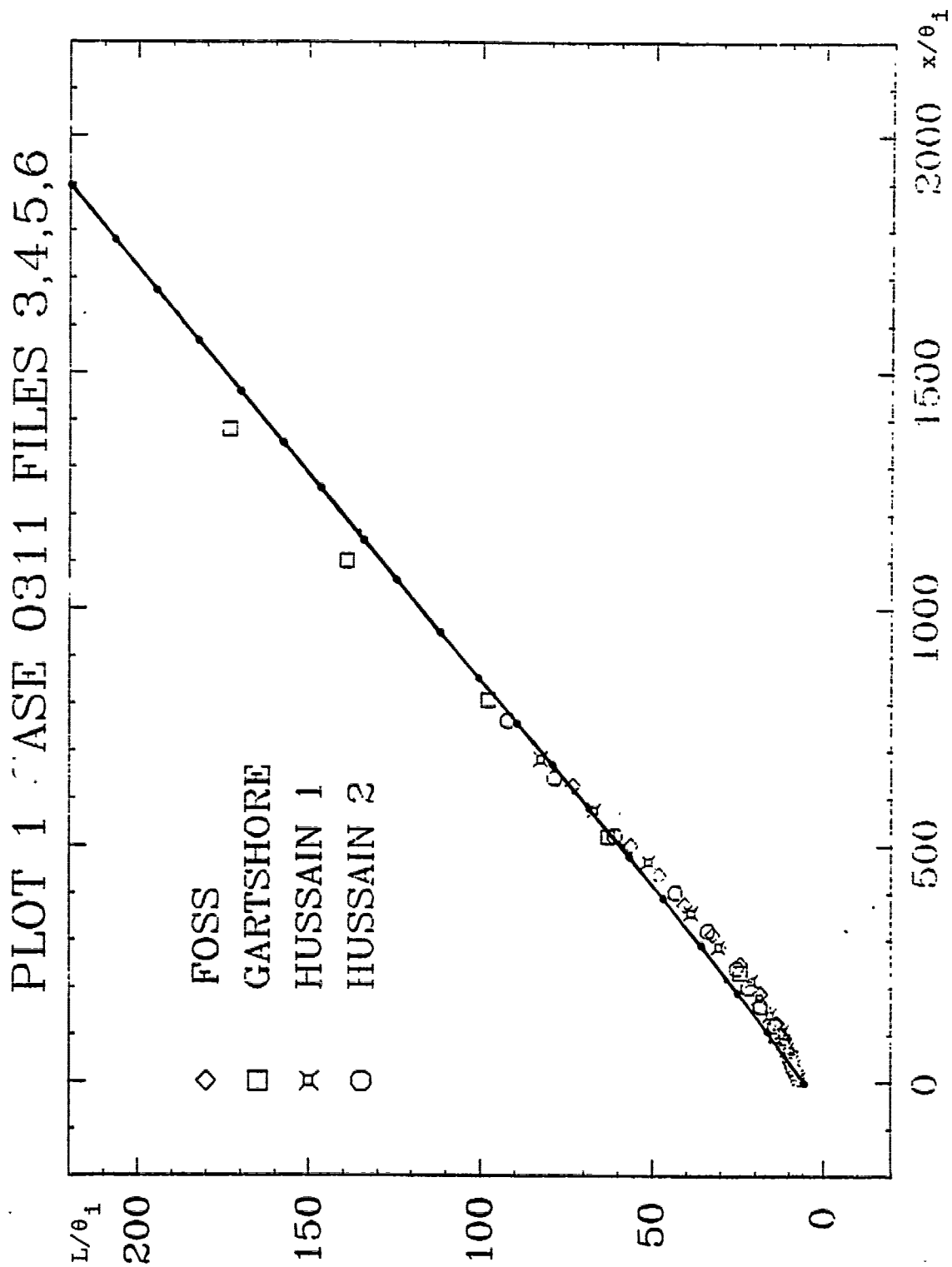


Figure 29. Development of an incompressible mixing layer.

PLOT 1 CASE 8501 FILE 2

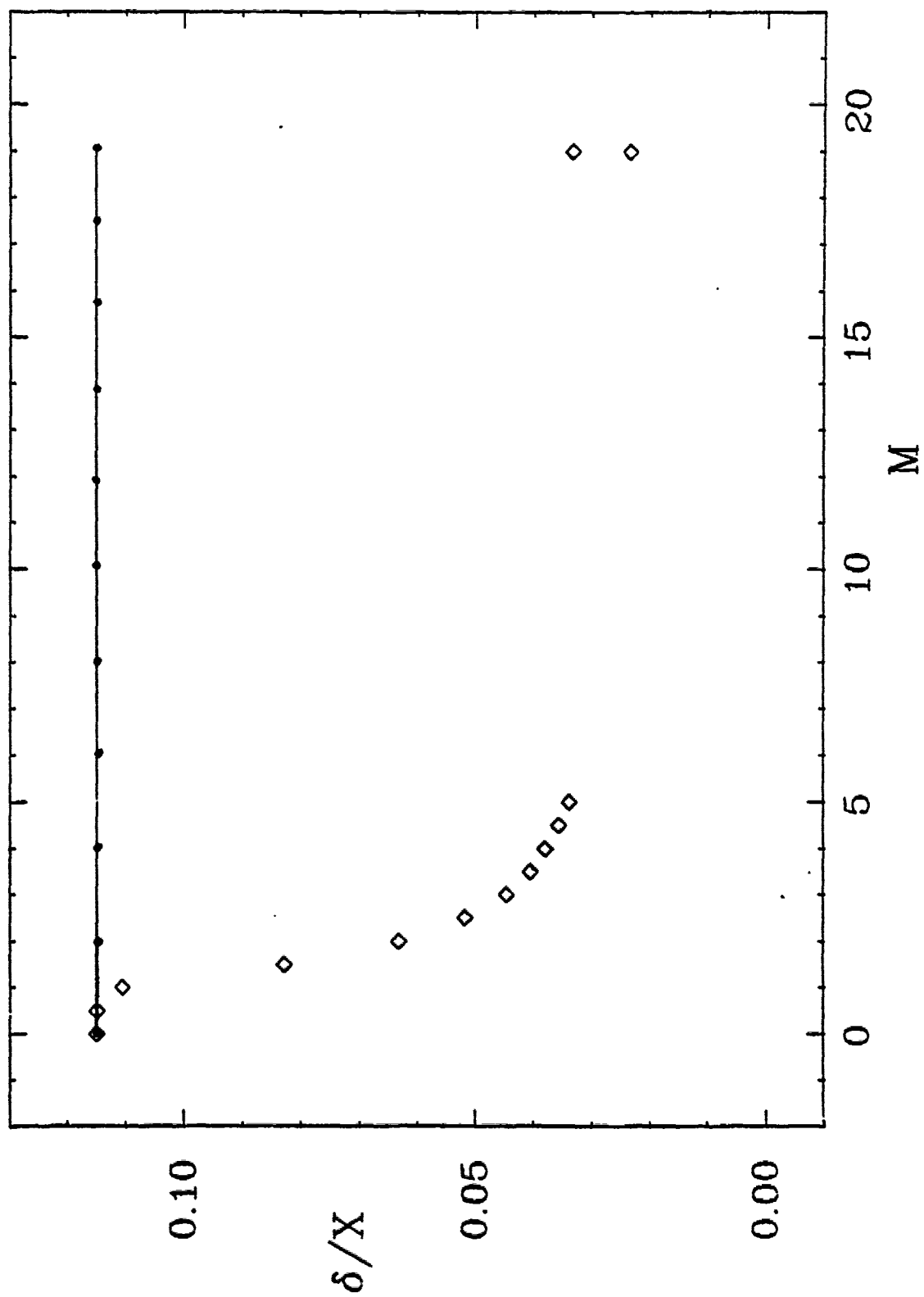


Figure 30. Effect of Mach number on mixing-layer growth.

PLOT 1 CASE 0241 FILE 2

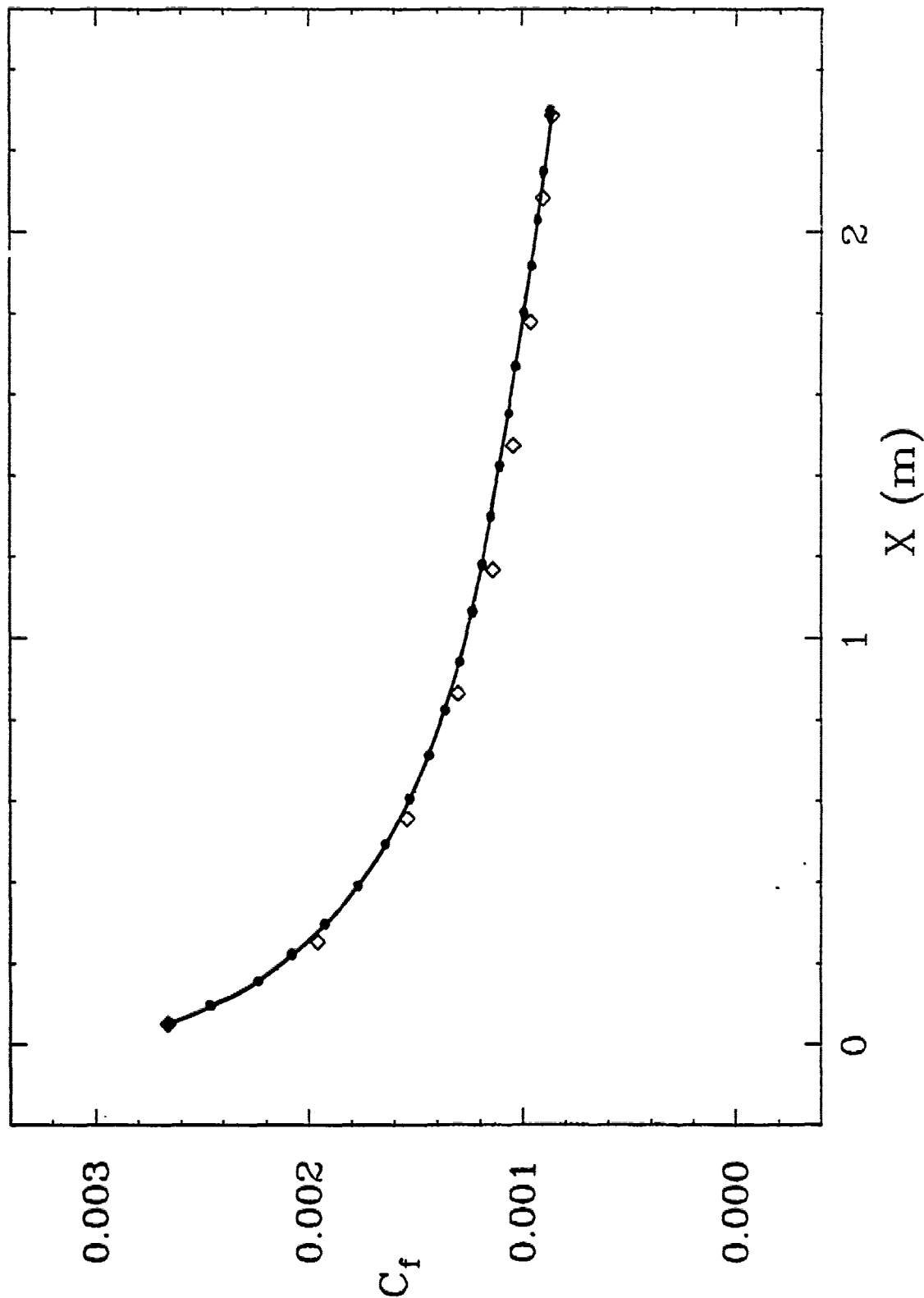


Figure 31. Incompressible boundary layer with uniform blowing.

PLOT 2 CASE 0241 FILE 2

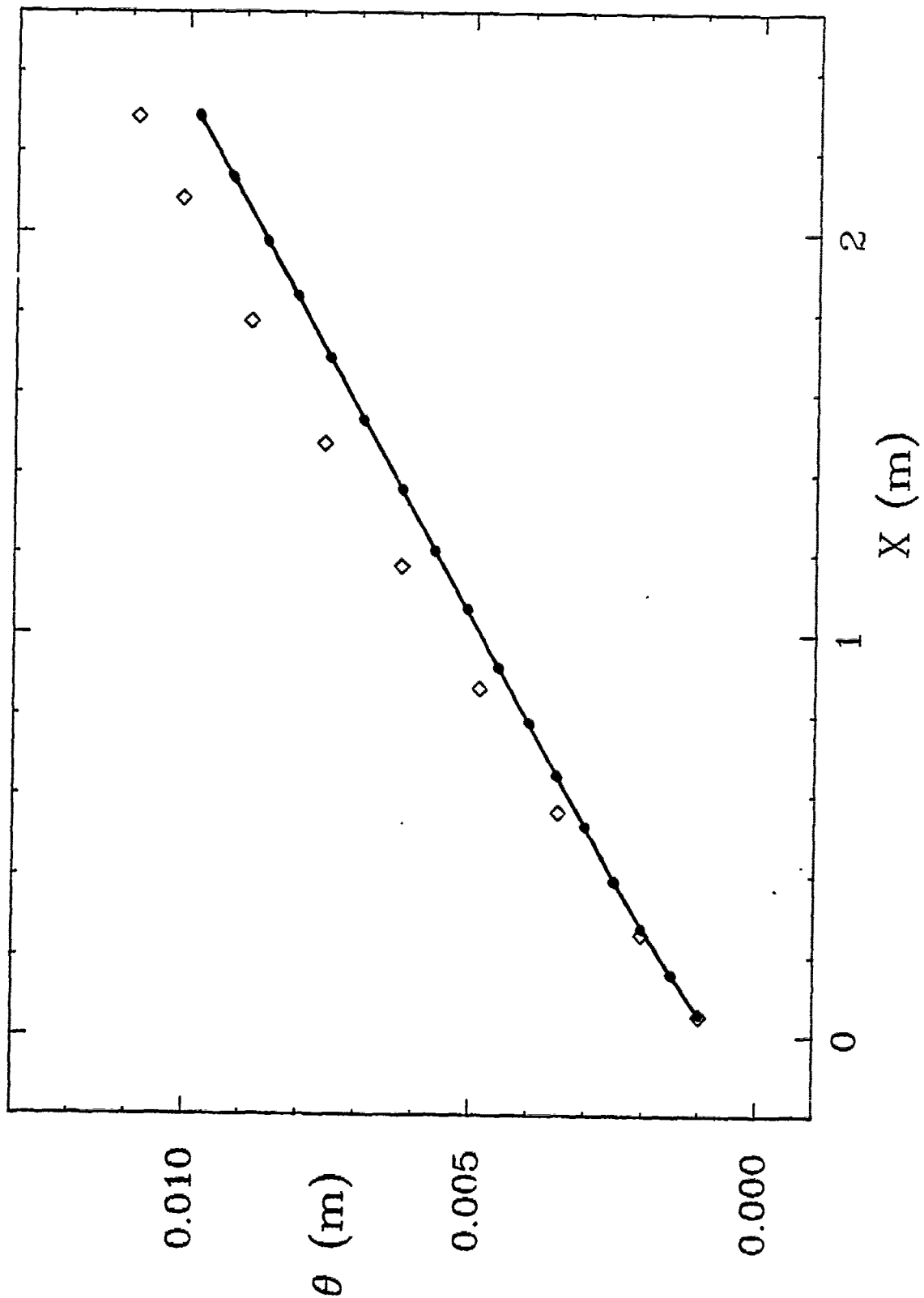


Figure 32. Incompressible boundary layer with uniform blowing.

PLOT 3 CASE 0241 FILE 2

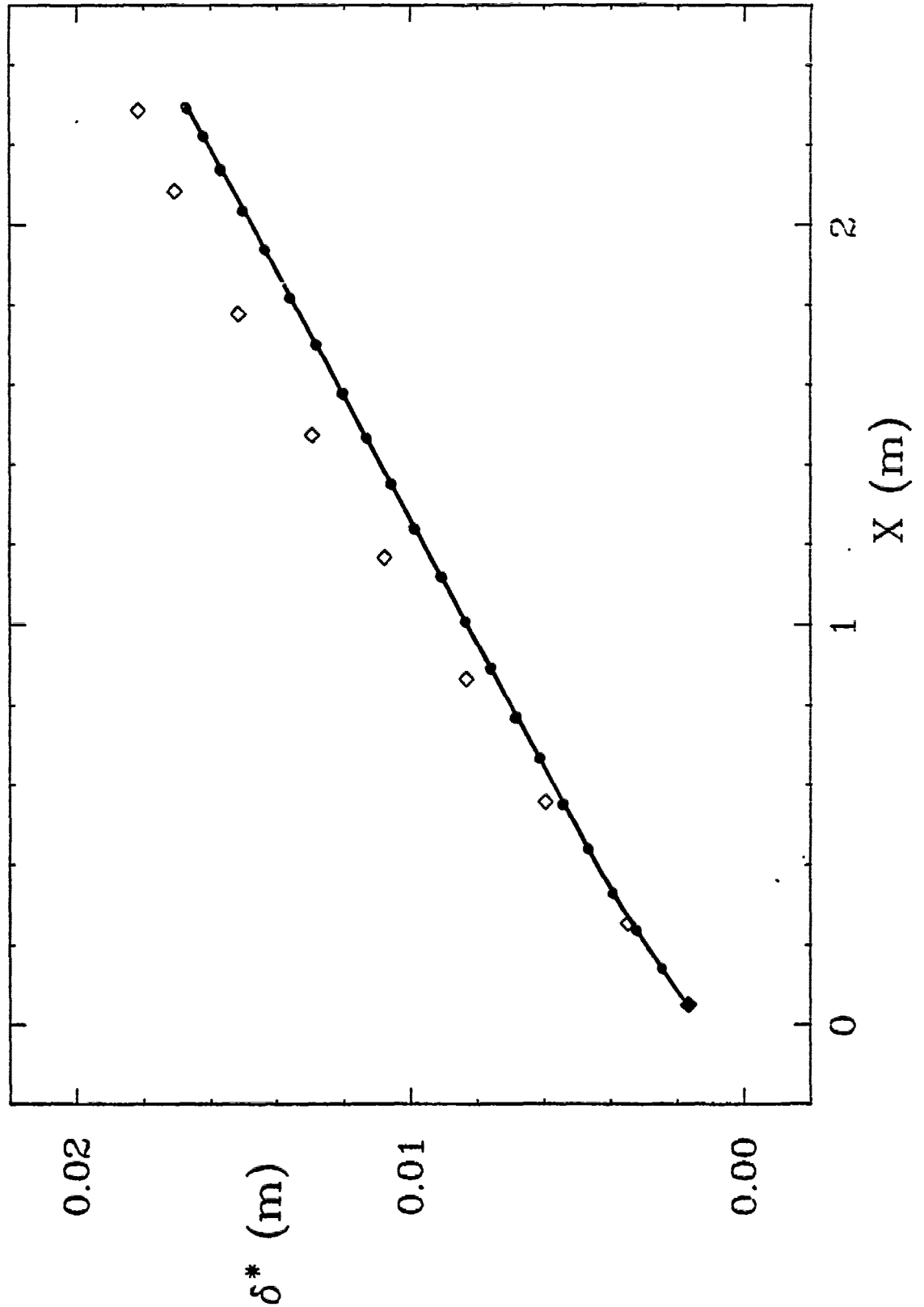


Figure 33. Incompressible boundary layer with uniform blowing.

PLOT 4 CASE 0241 FILES 5,7,9,11

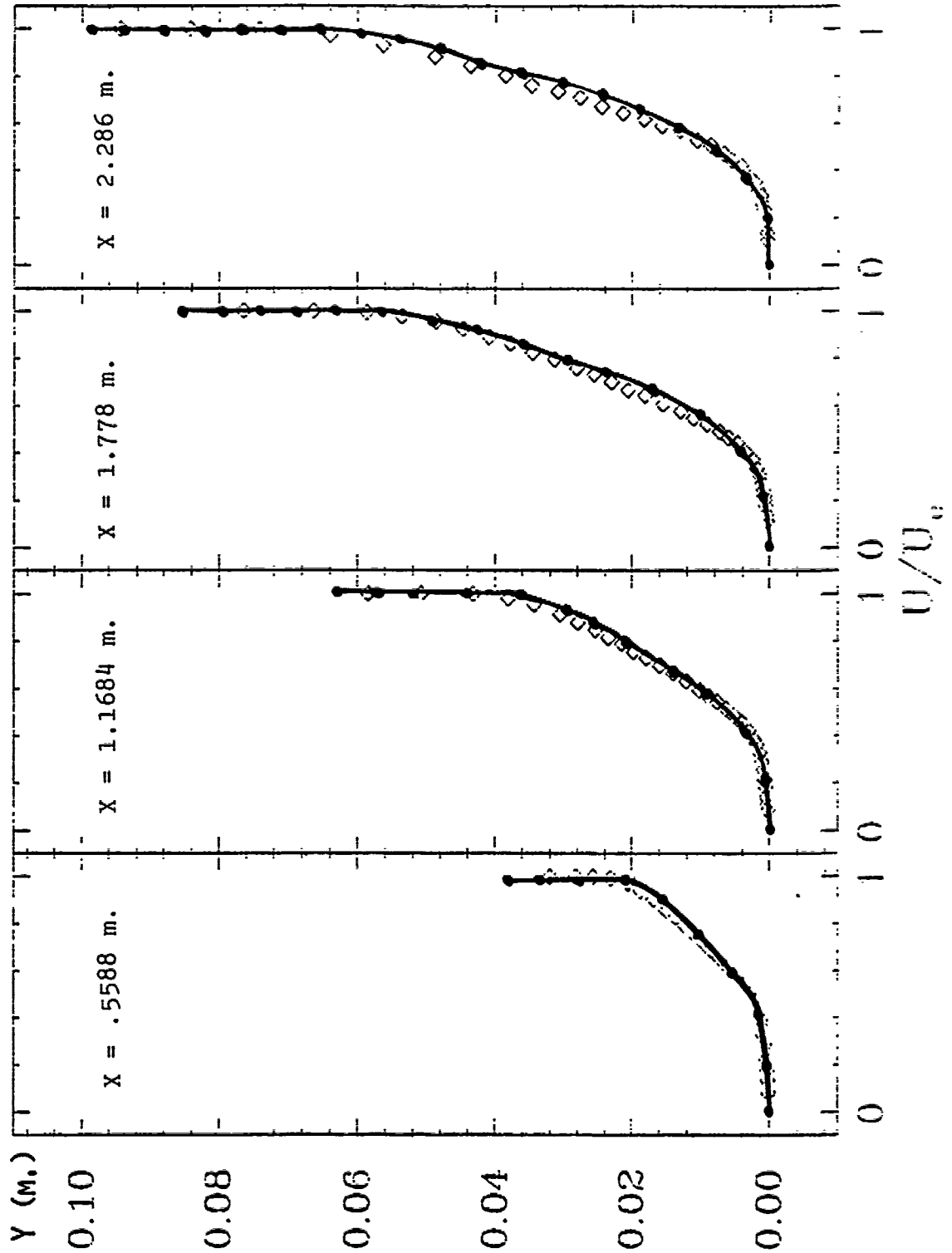


Figure 34. Incompressible boundary layer with uniform blowing.

PLOT 1 CASE 0242 FILE 2

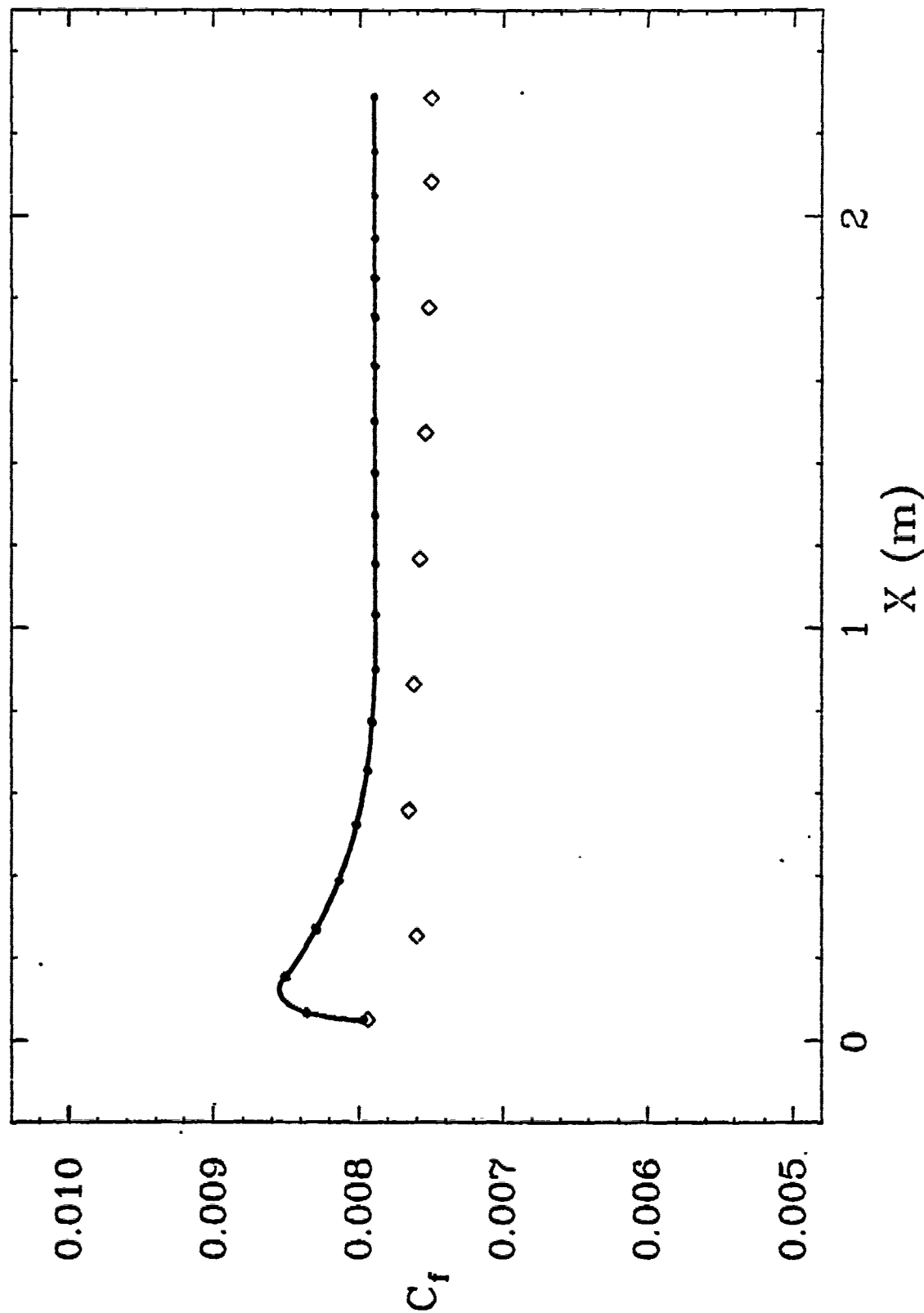


Figure 35. Incompressible boundary layer with suction.

PLOT 2 CASE 0242 FILE 2

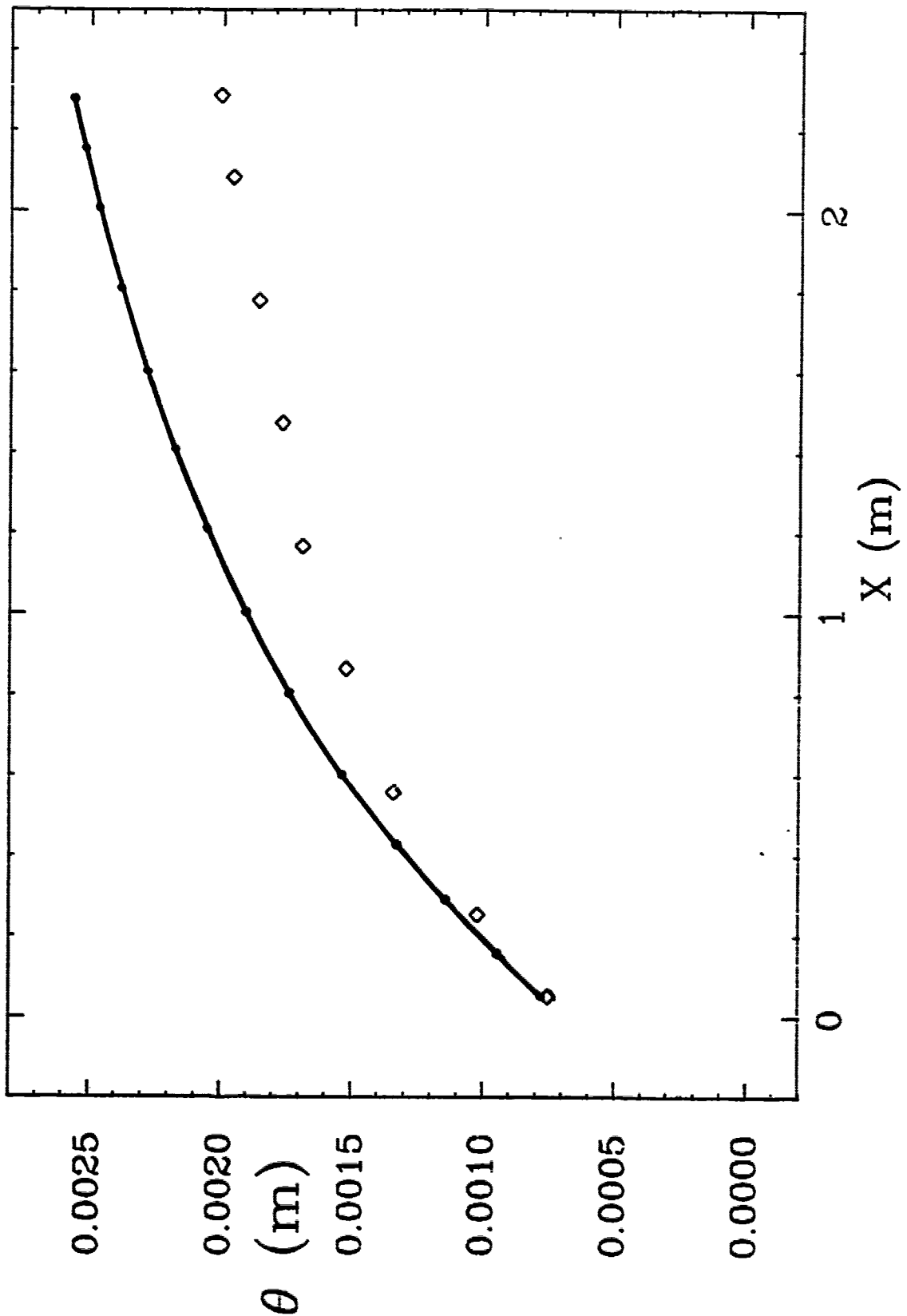


Figure 36. Incompressible boundary layer with suction.

PLOT 3 CASE 0242 FILE 2

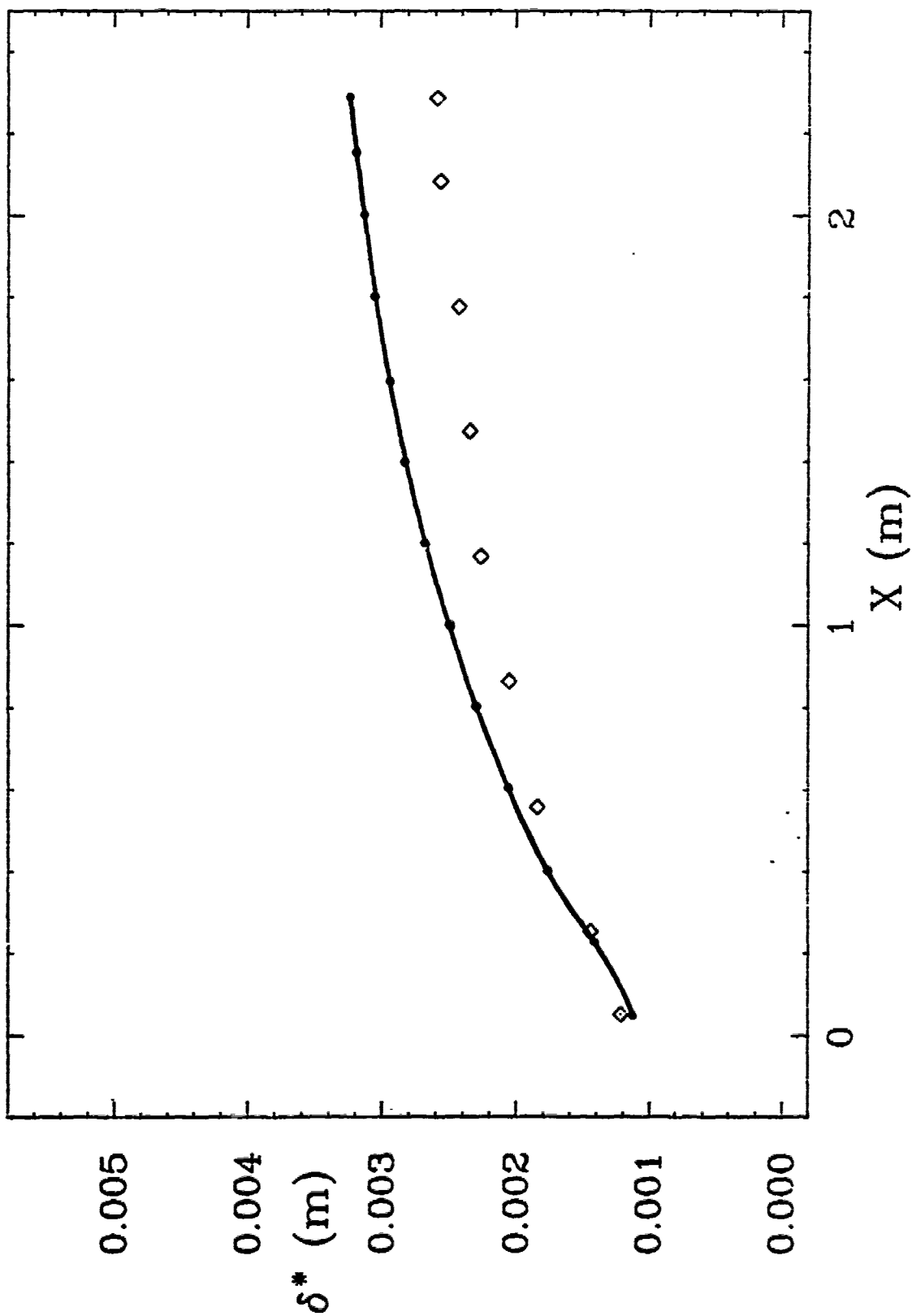


Figure 37. Incompressible boundary layer with suction.

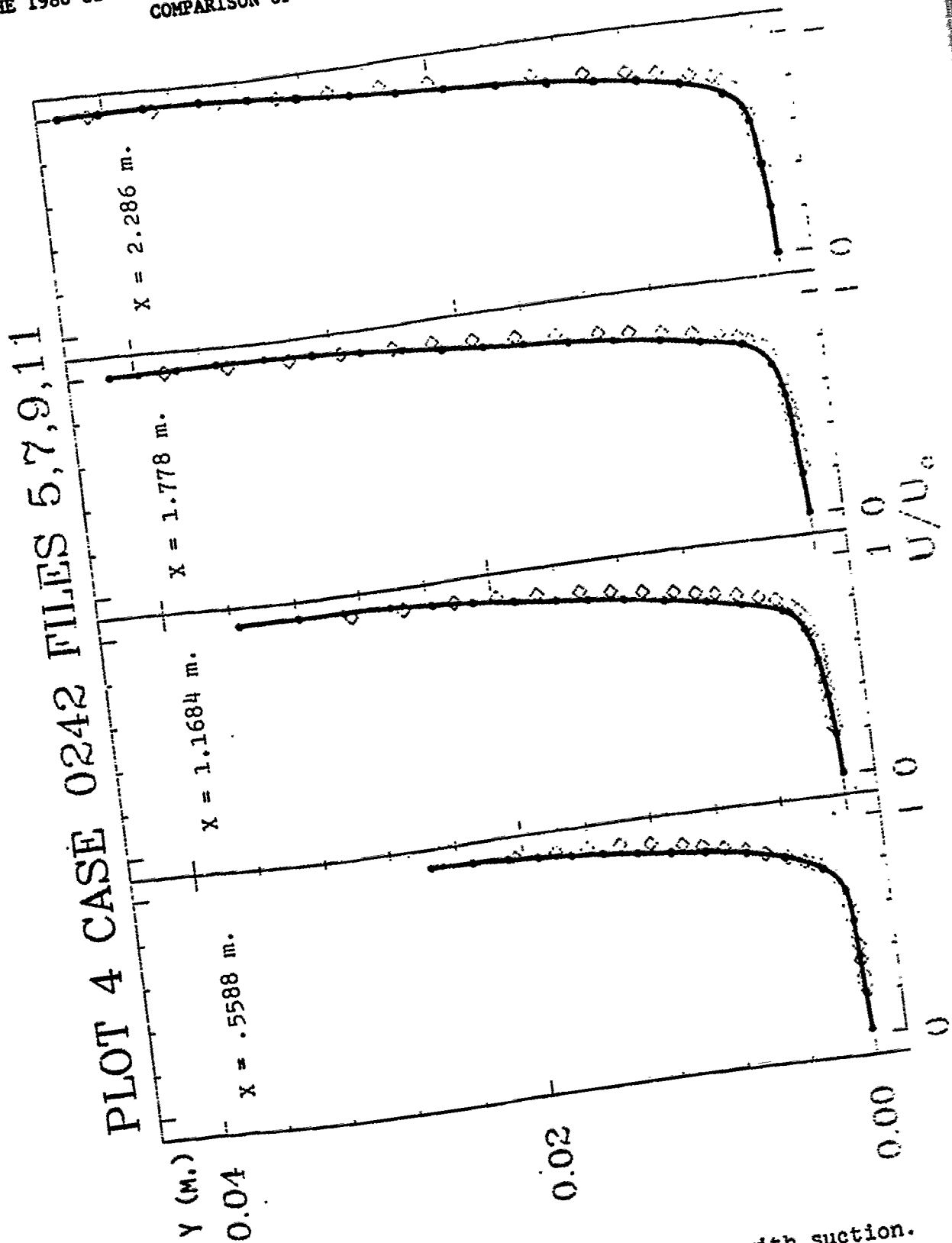


Figure 38. Incompressible boundary layer with suction.

PLOT 1 CASE 0244 FILES 8,9

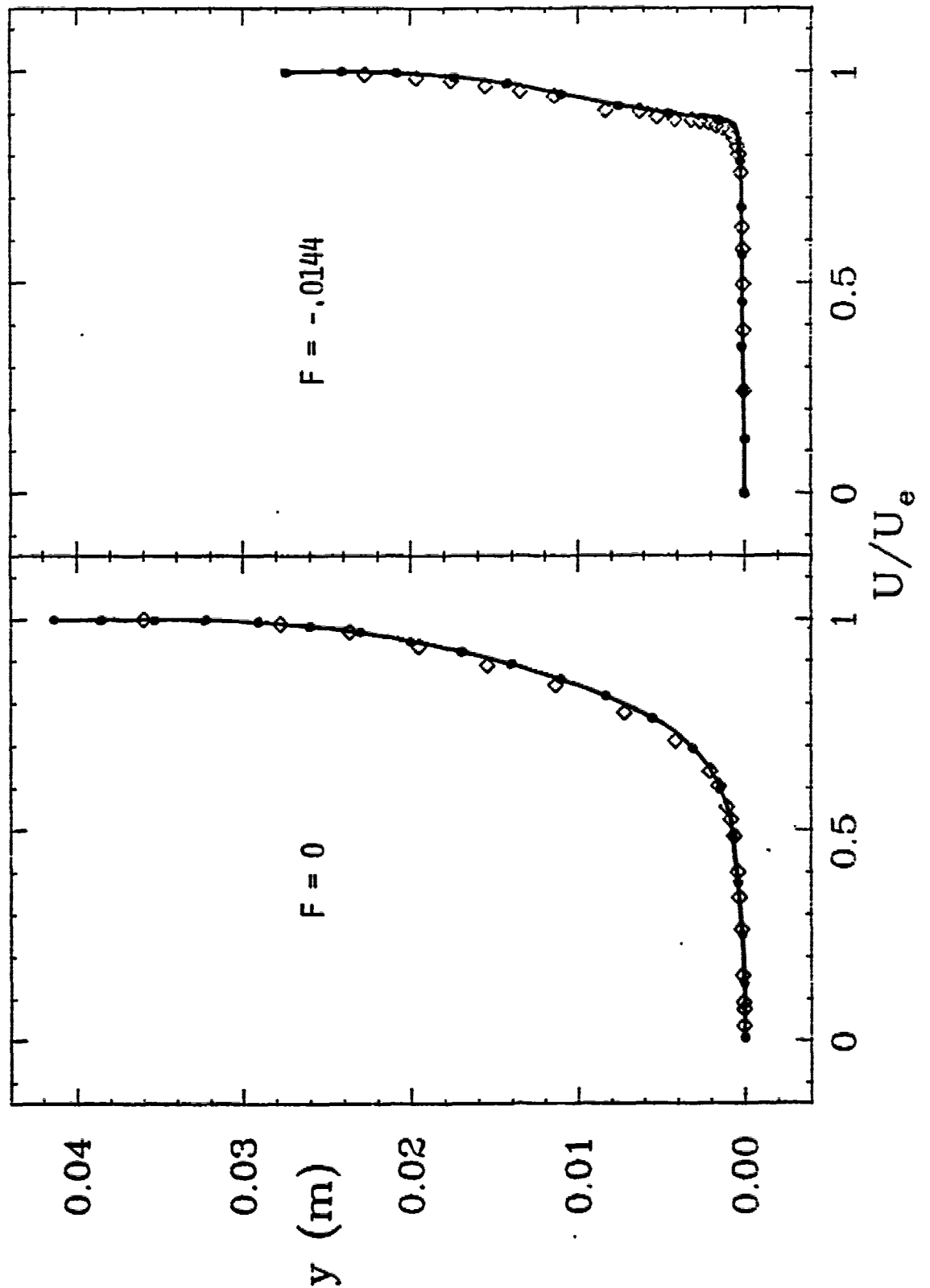


Figure 39. Incompressible boundary layers with uniform suction.

PLOT 2 CASE 0244 FILES 3-7

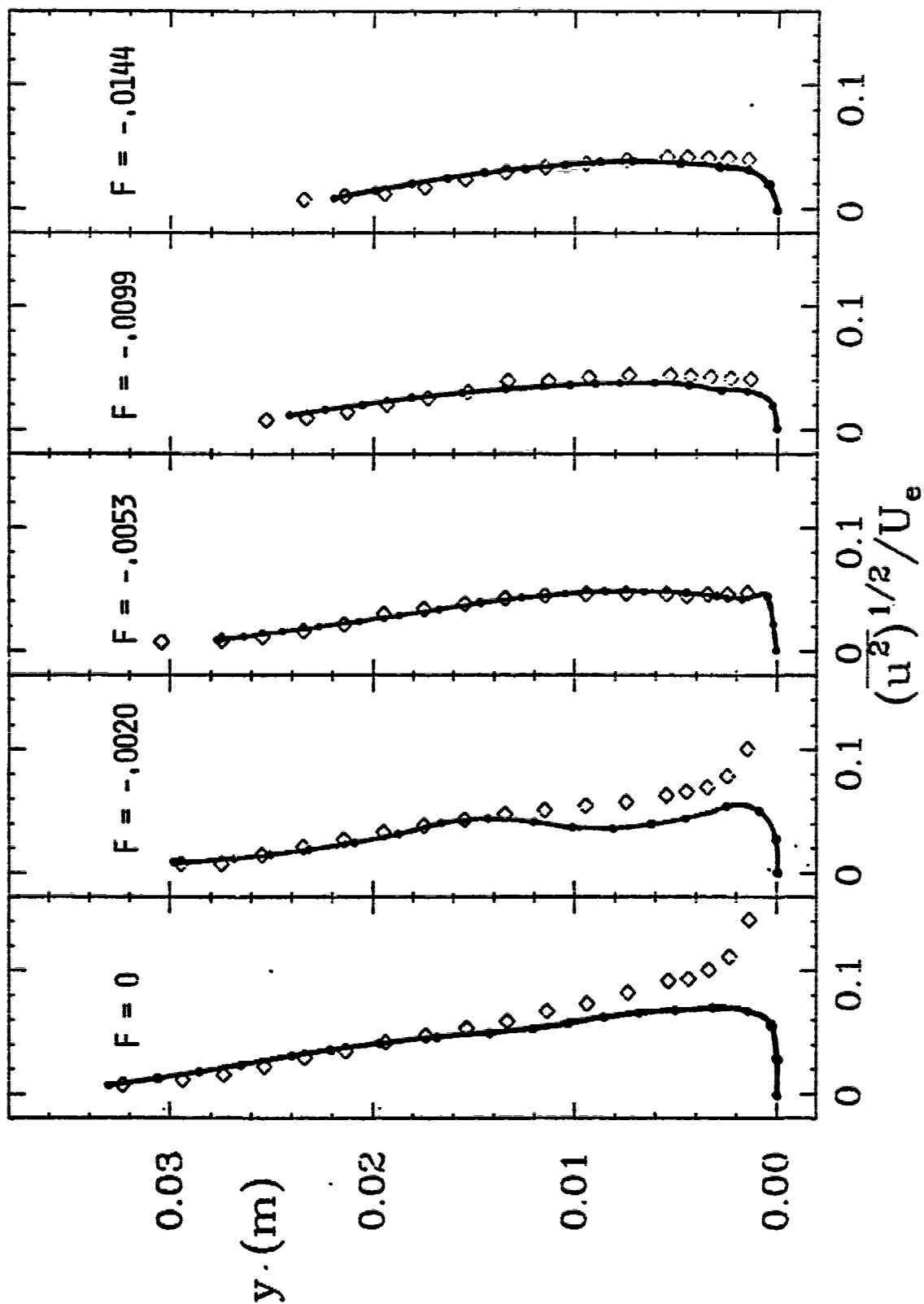


Figure 40. Incompressible boundary layers with uniform suction.

PLOT 3 CASE 0244 FILES 3-7

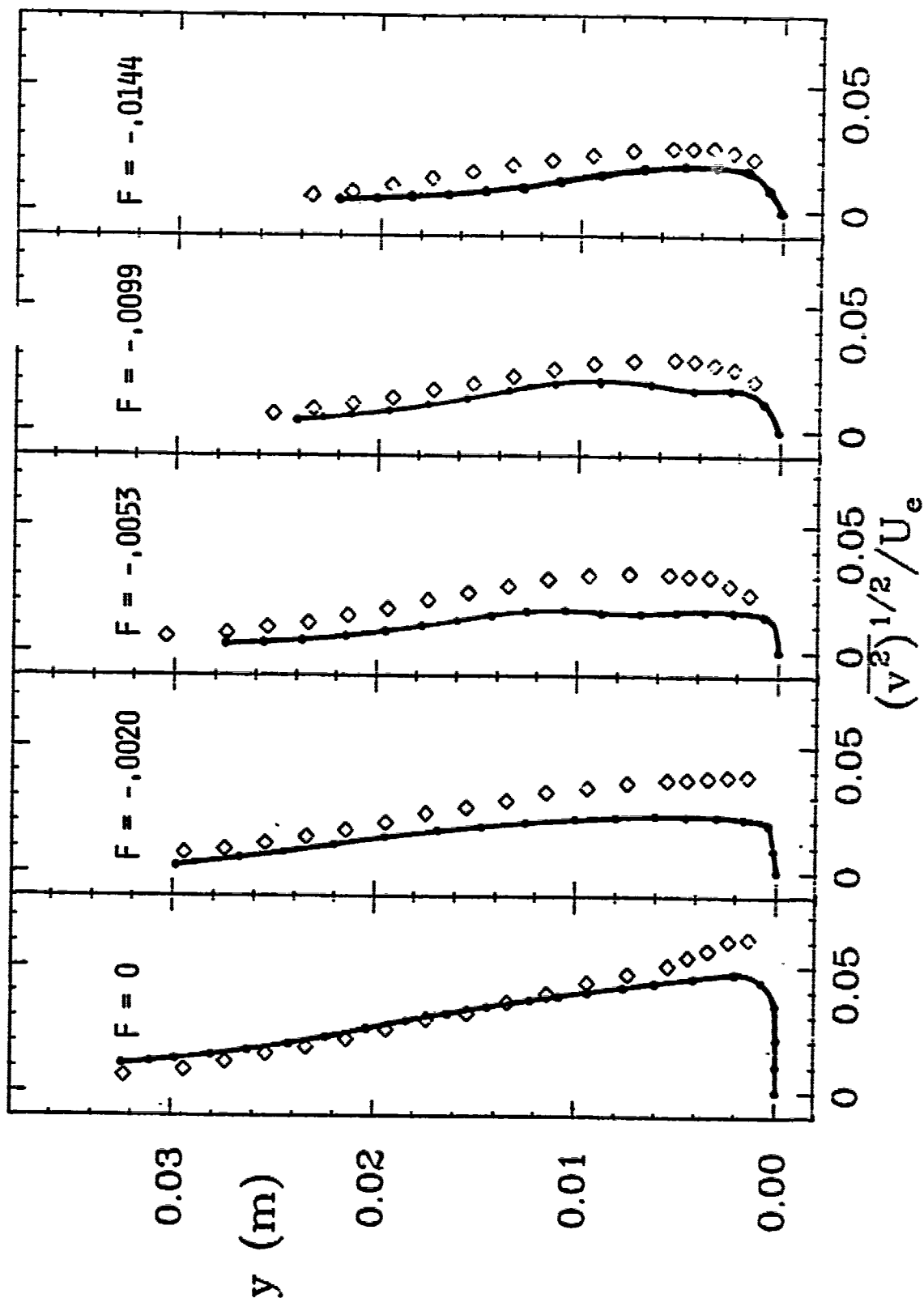


Figure 41. Incompressible boundary layers with uniform suction.

PLOT 4 CASE 0244 FILES 3-7

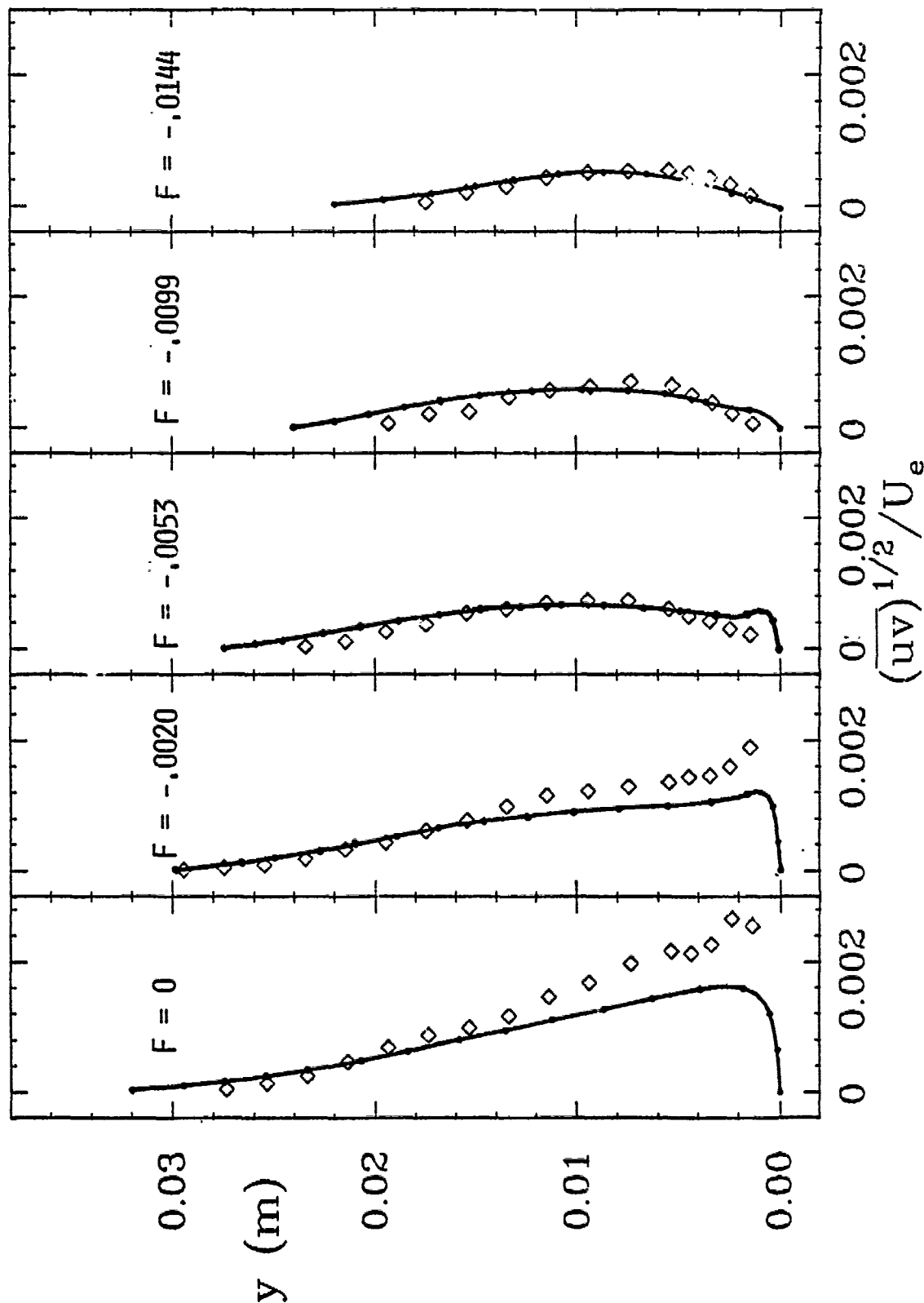


Figure 42. Incompressible boundary layers with uniform suction.

PLOT 1 CASE 0141 FILE 4

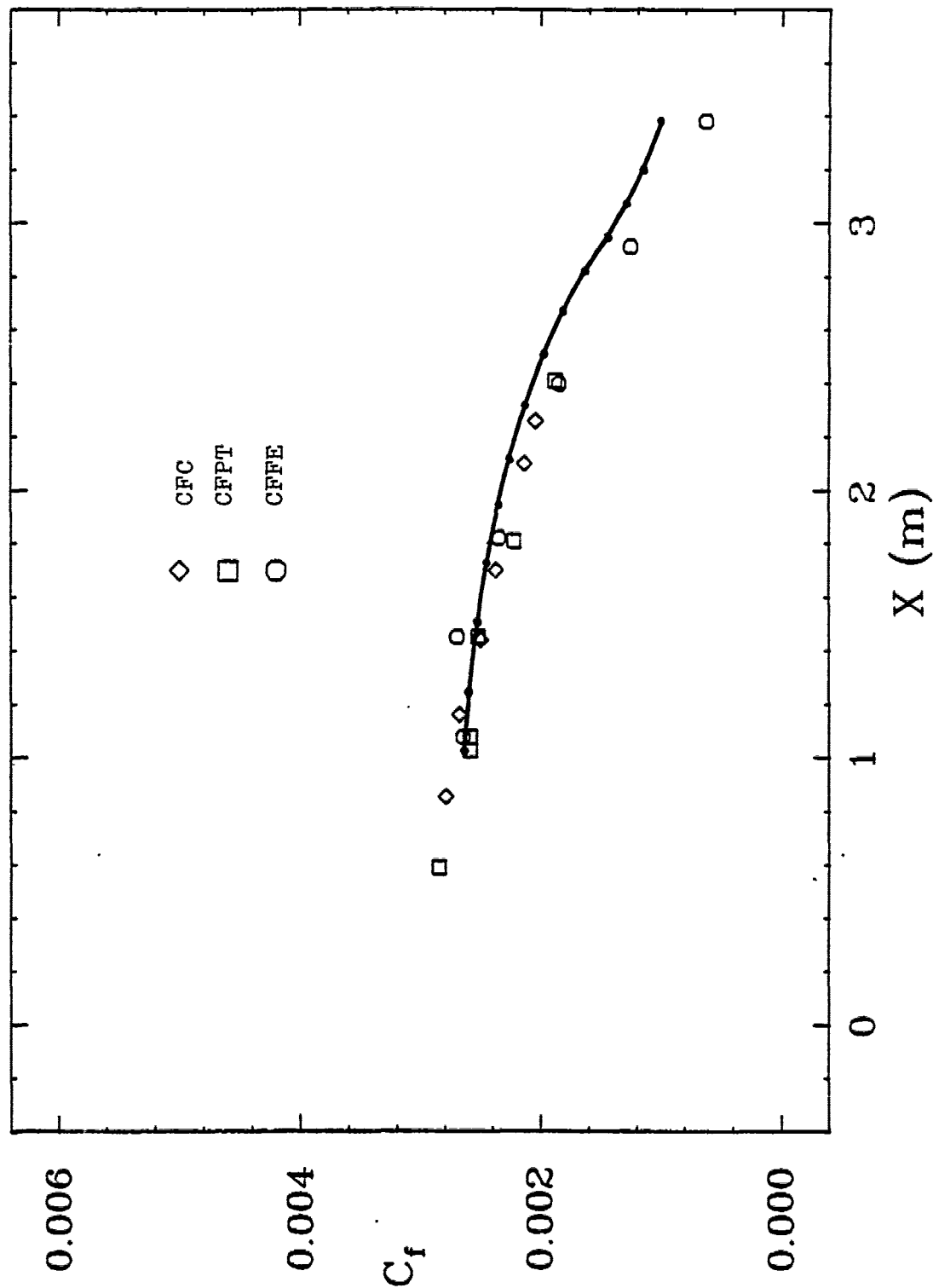


Figure 43. Incompressible boundary layer with adverse pressure gradient.

PLOT 2 CASE 0141 FILE 25,26,27

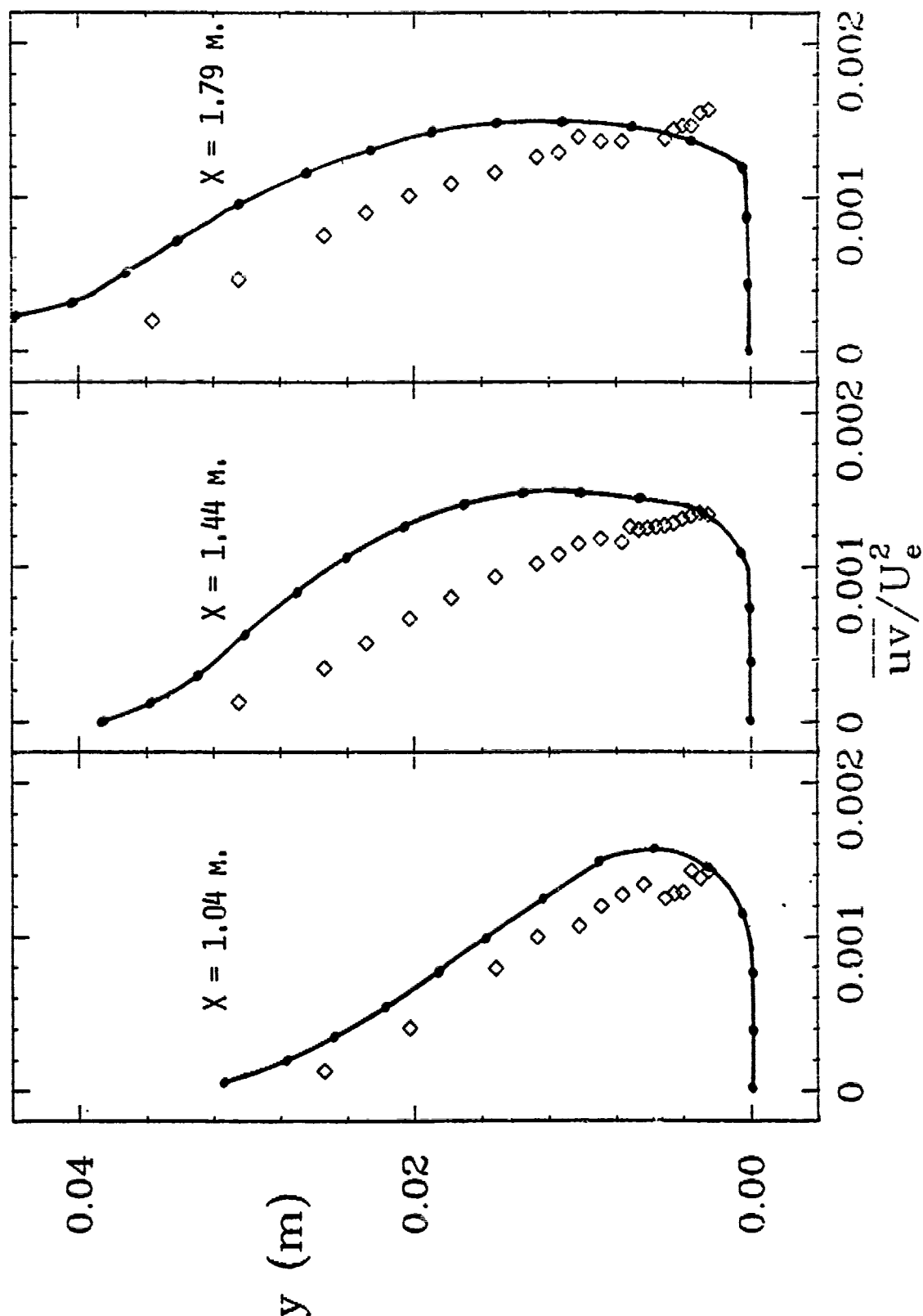


Figure 44. Incompressible boundary layer with adverse pressure gradient.

PLOT 3 CASE 0141 FILE 28,29,30

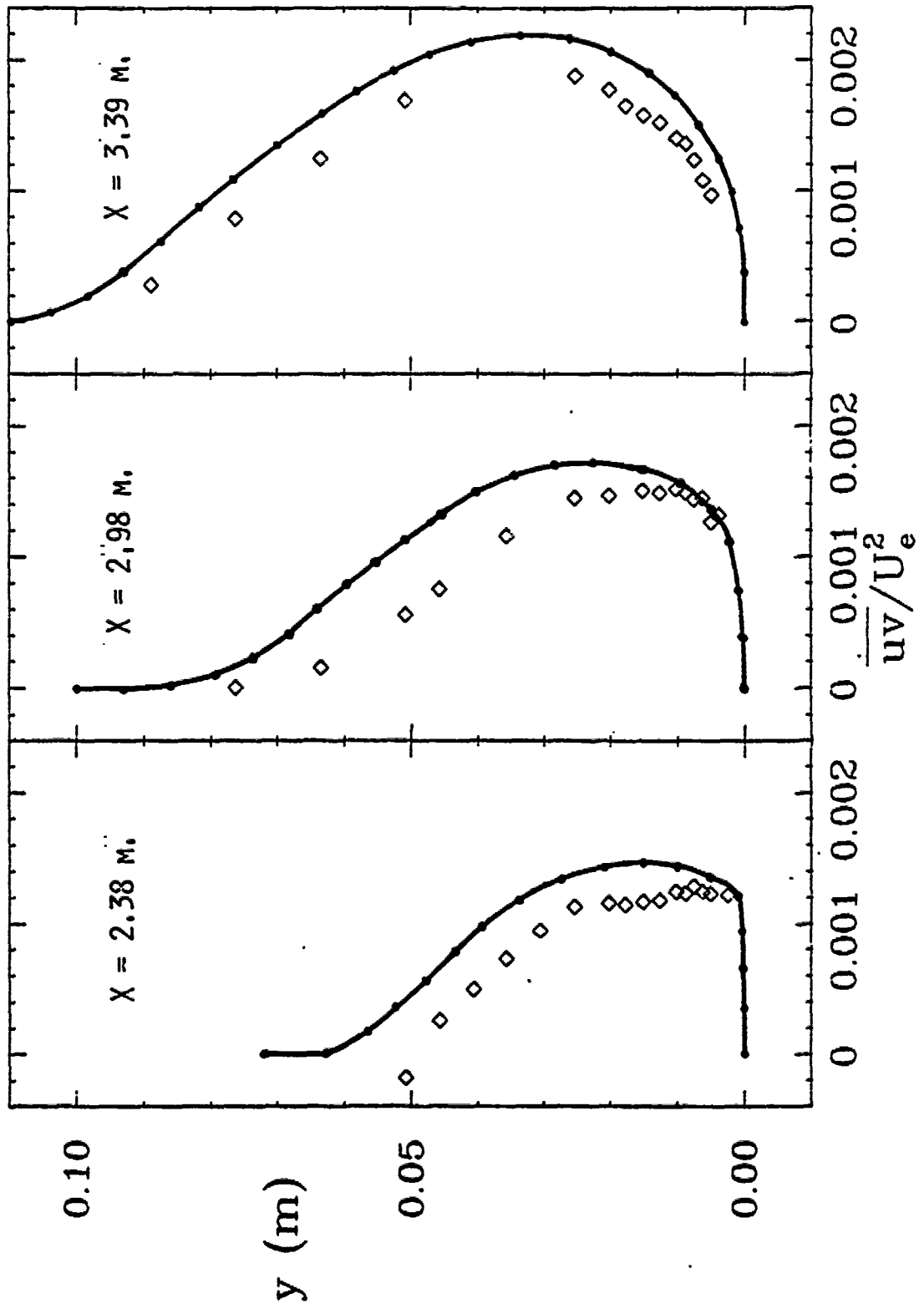


Figure 45. Incompressible boundary layer with adverse pressure gradient.

PLOT 4 CASE 0141 FILES 14,16

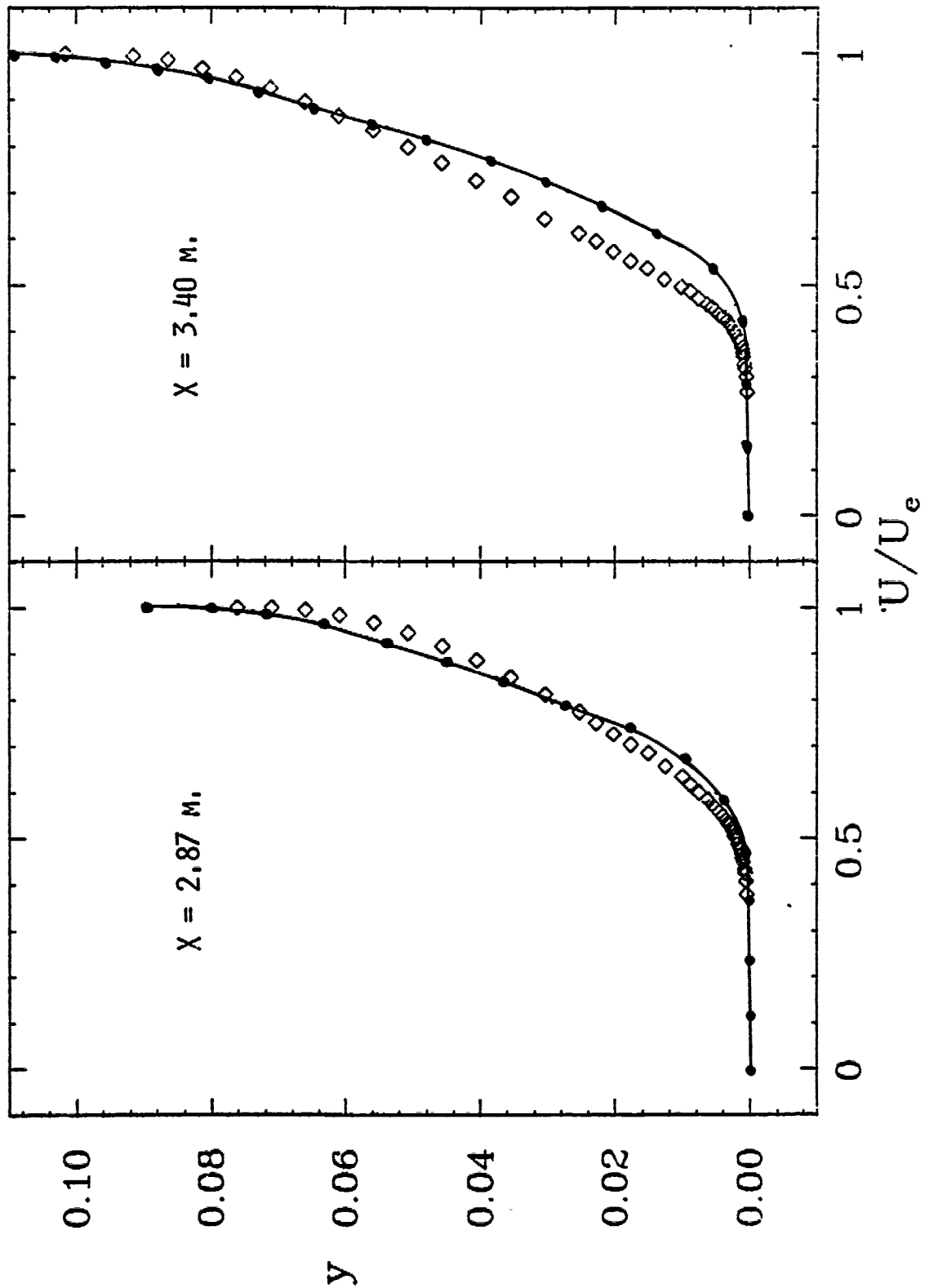


Figure 46. Incompressible boundary layer with adverse pressure gradient.

PLOT 1 CASE 8403 FILES 2,3,5 CENTERBODY II

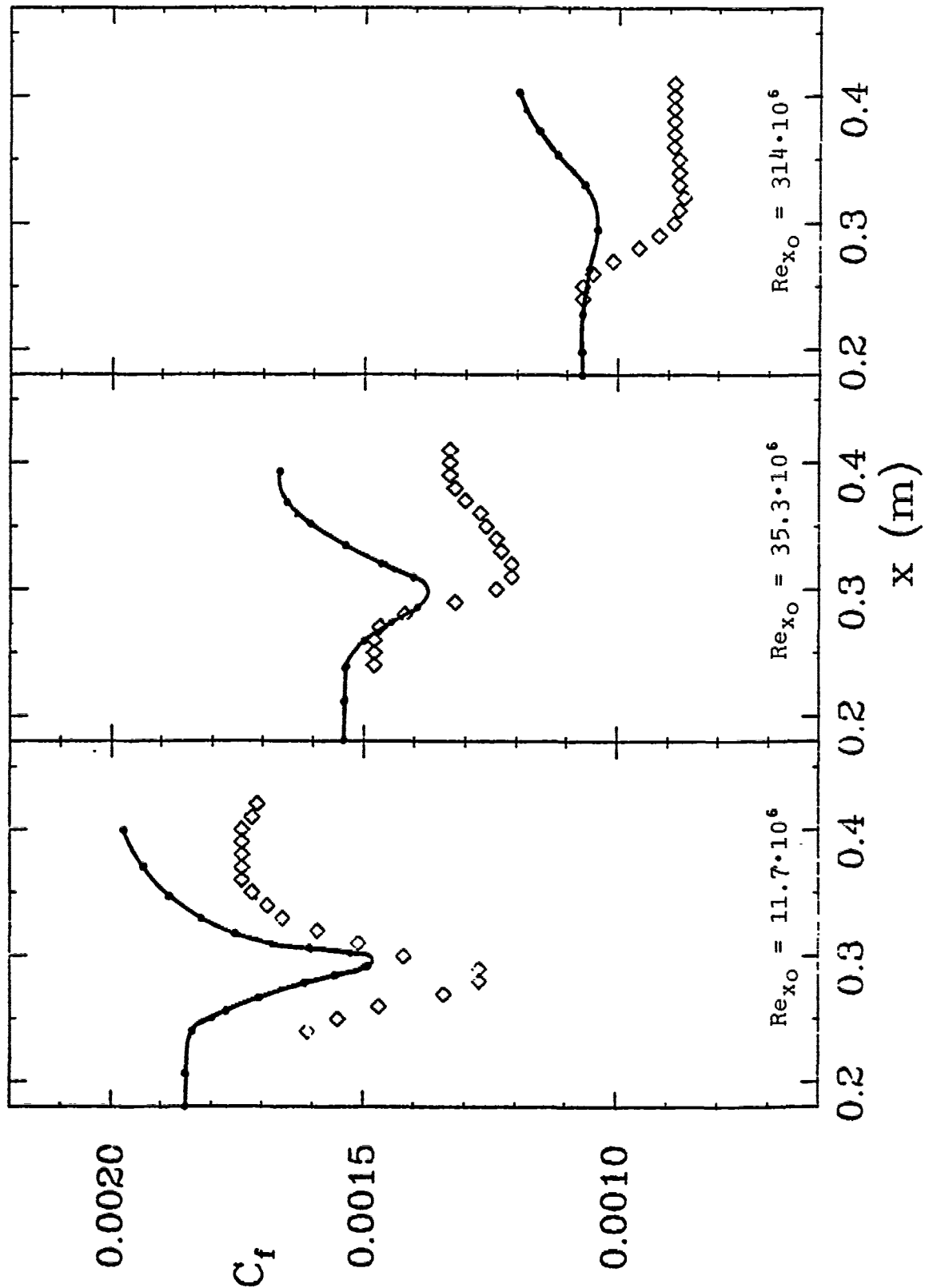


Figure 47. Mach 2.2 boundary layers with adverse pressure gradient.

PLOT 2 CASE 8403 FILES 6,7,9 CENTERBODY IV

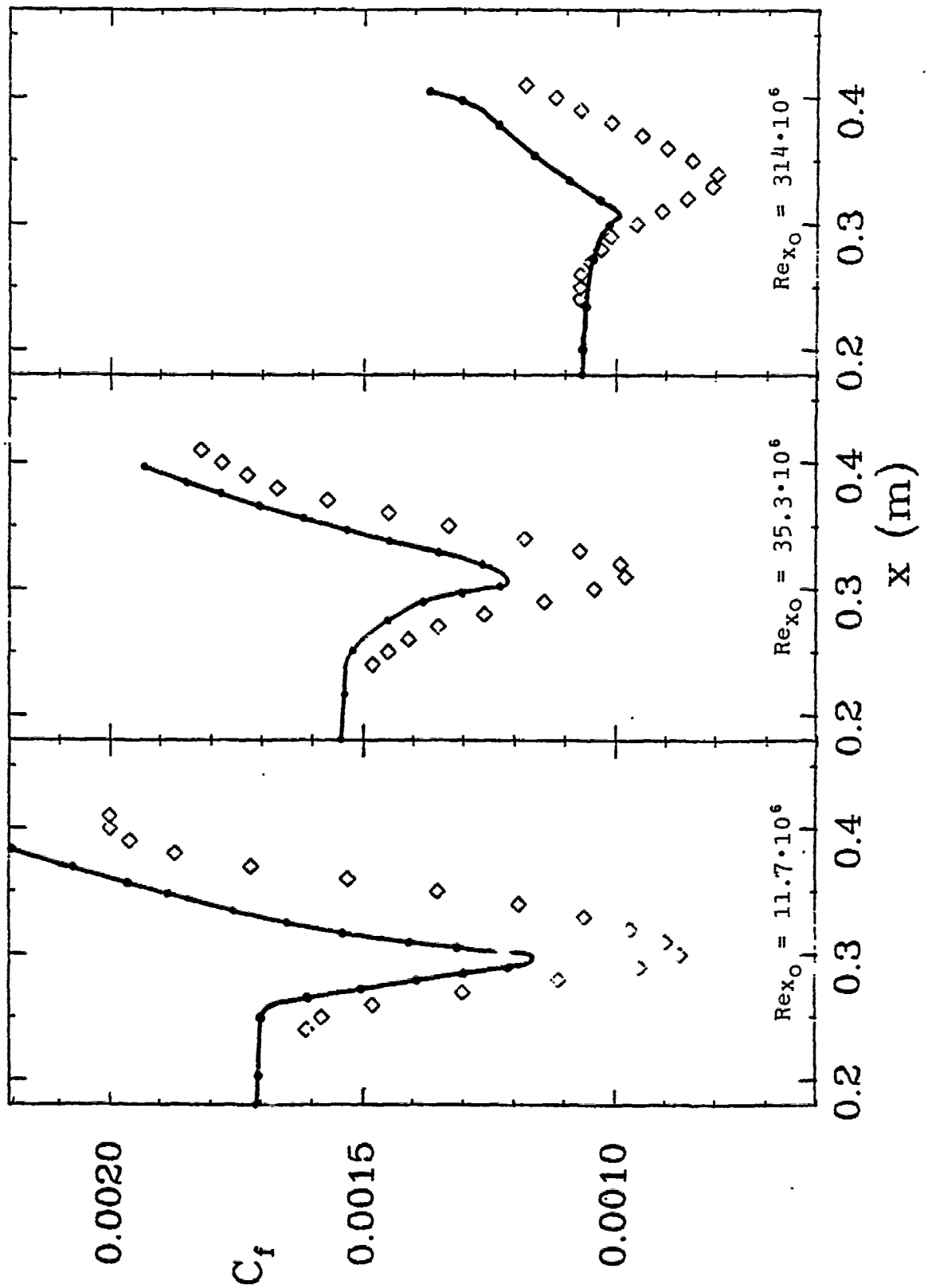


Figure 48. Mach 2.2 boundary layers with adverse pressure gradient.

PLOT 3 CASE 8403 FILES 10,11,13 CENTERBODY VI

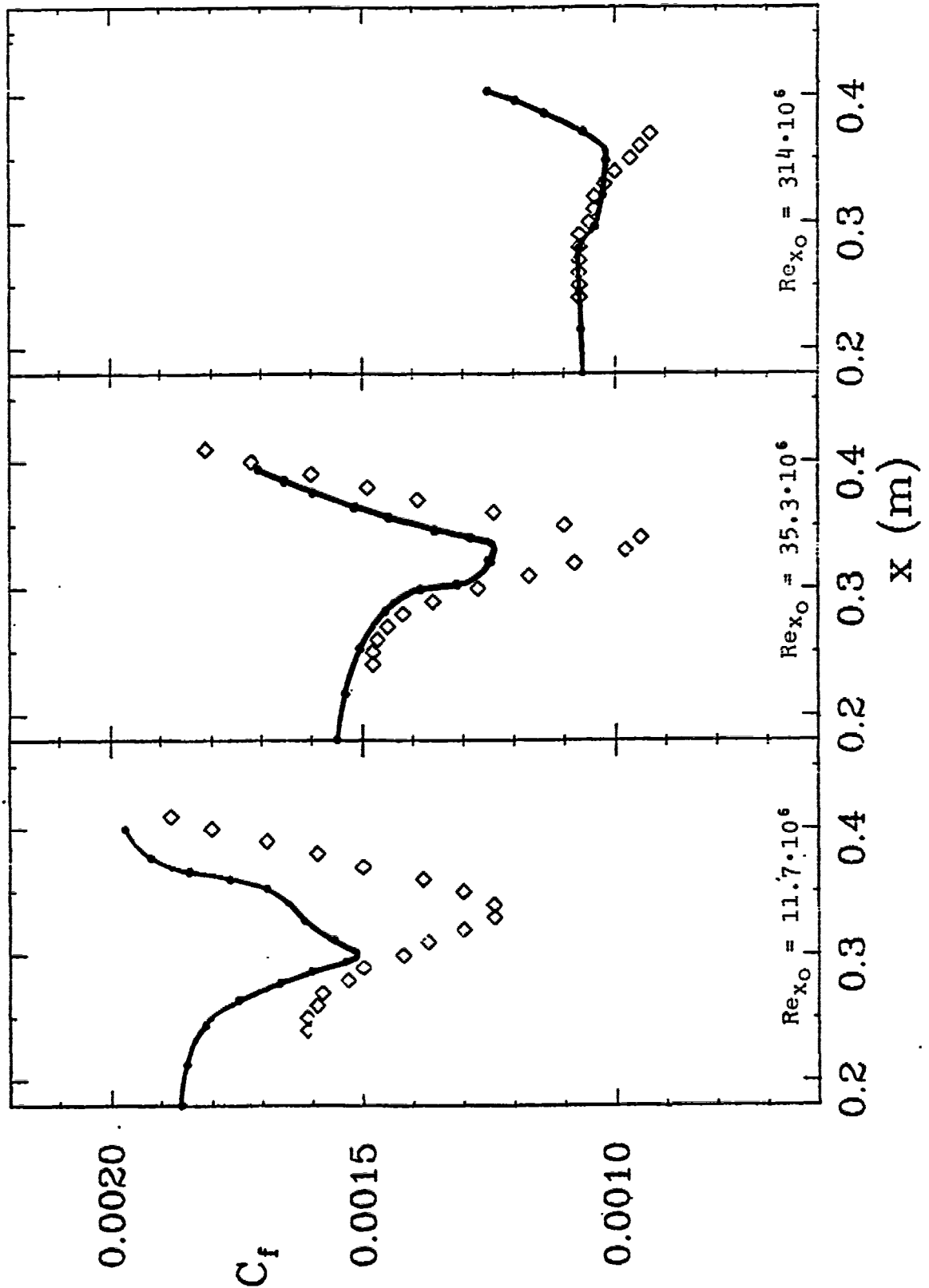


Figure 49. Mach 2.2 boundary layers with adverse pressure gradient.

PLOT 4 CASE 8403 FILE 14 CENTERBODY II

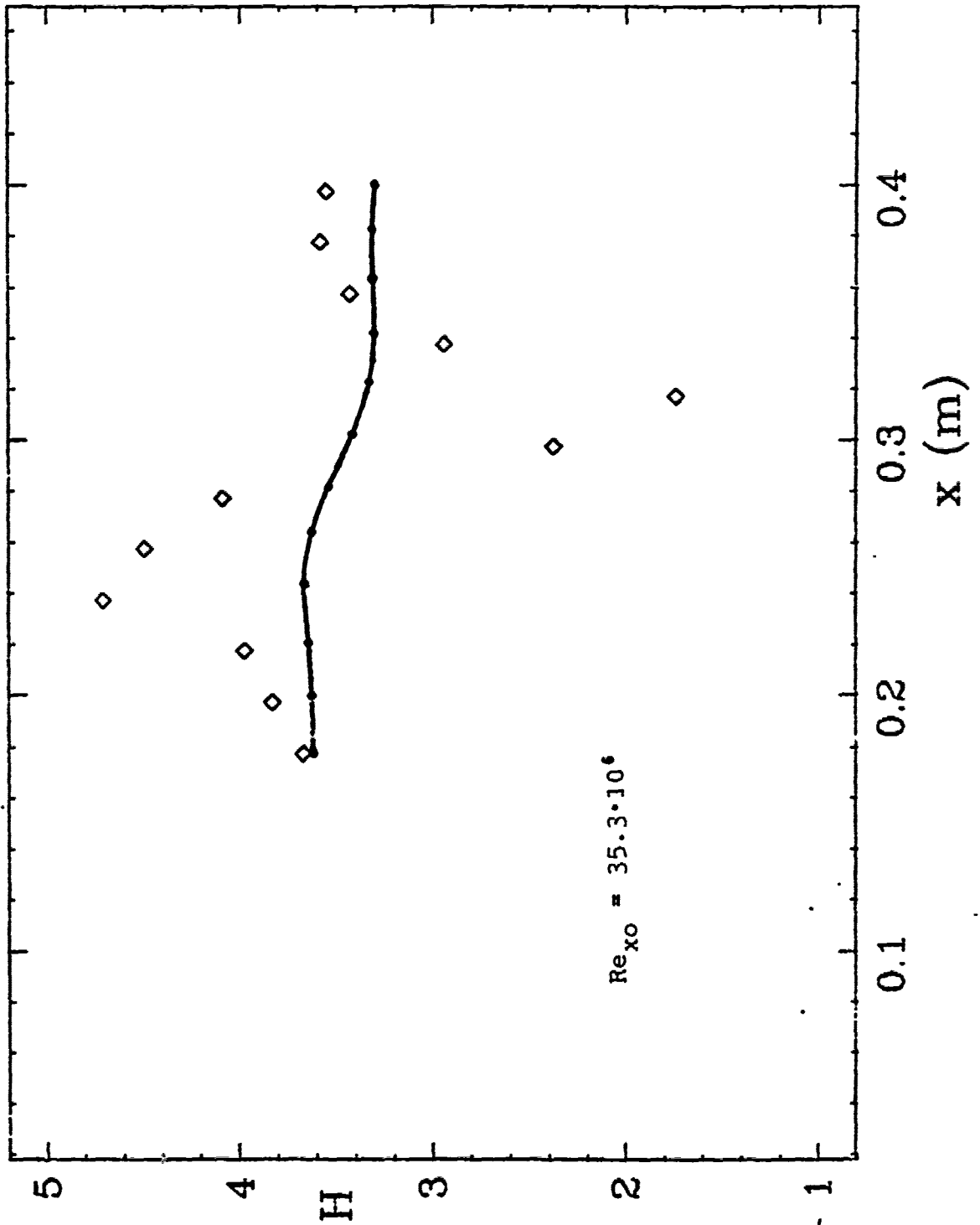


Figure 50. Mach 2.2 boundary layer with adverse pressure gradient.

PLOT 5 CASE 8403 FILE 15 CENTERBODY IV

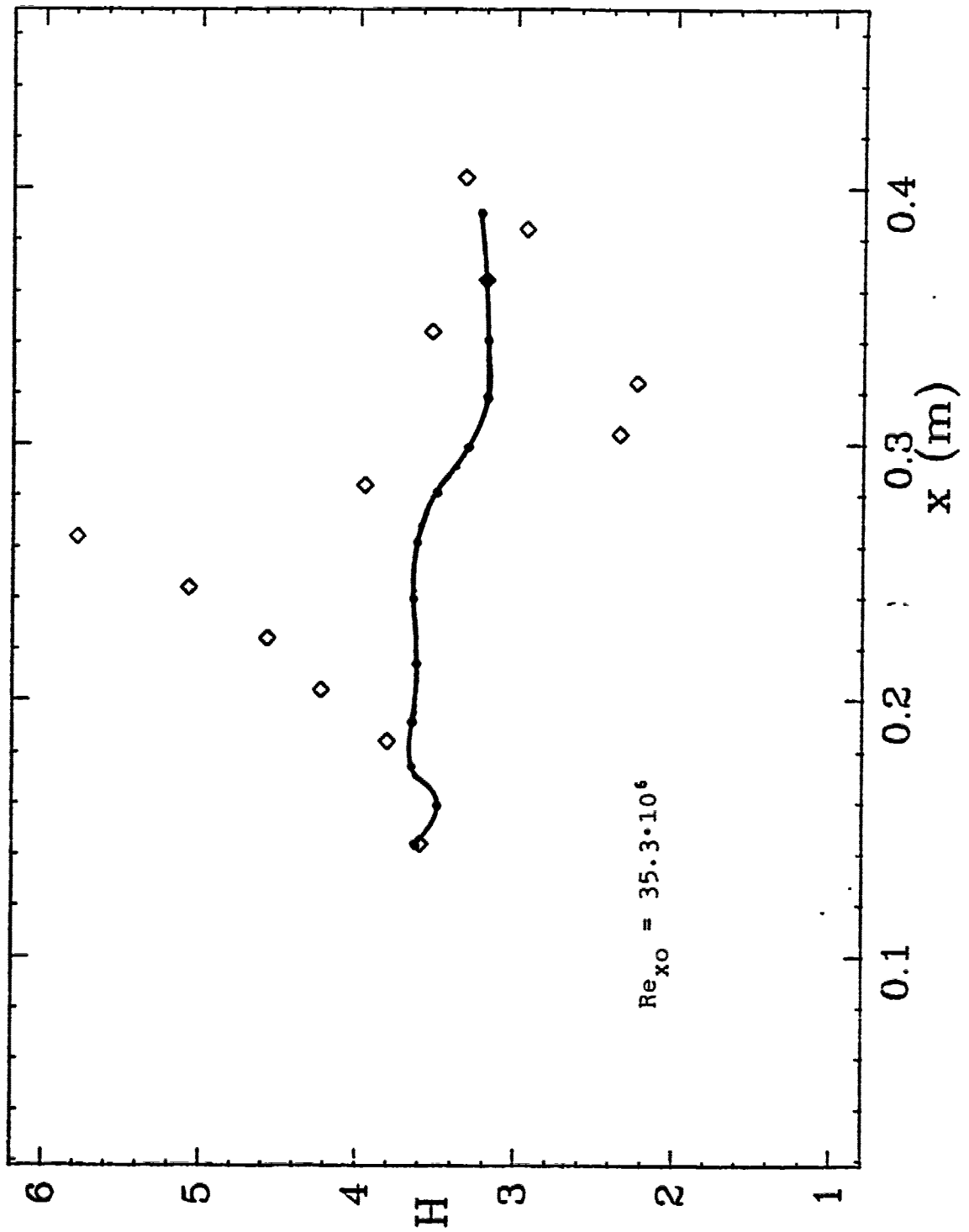


Figure 51. Mach 2.2 boundary layer with adverse pressure gradient.

PLOT 6 CASE 8403 FILES 17,21,23 CENTER BODY II

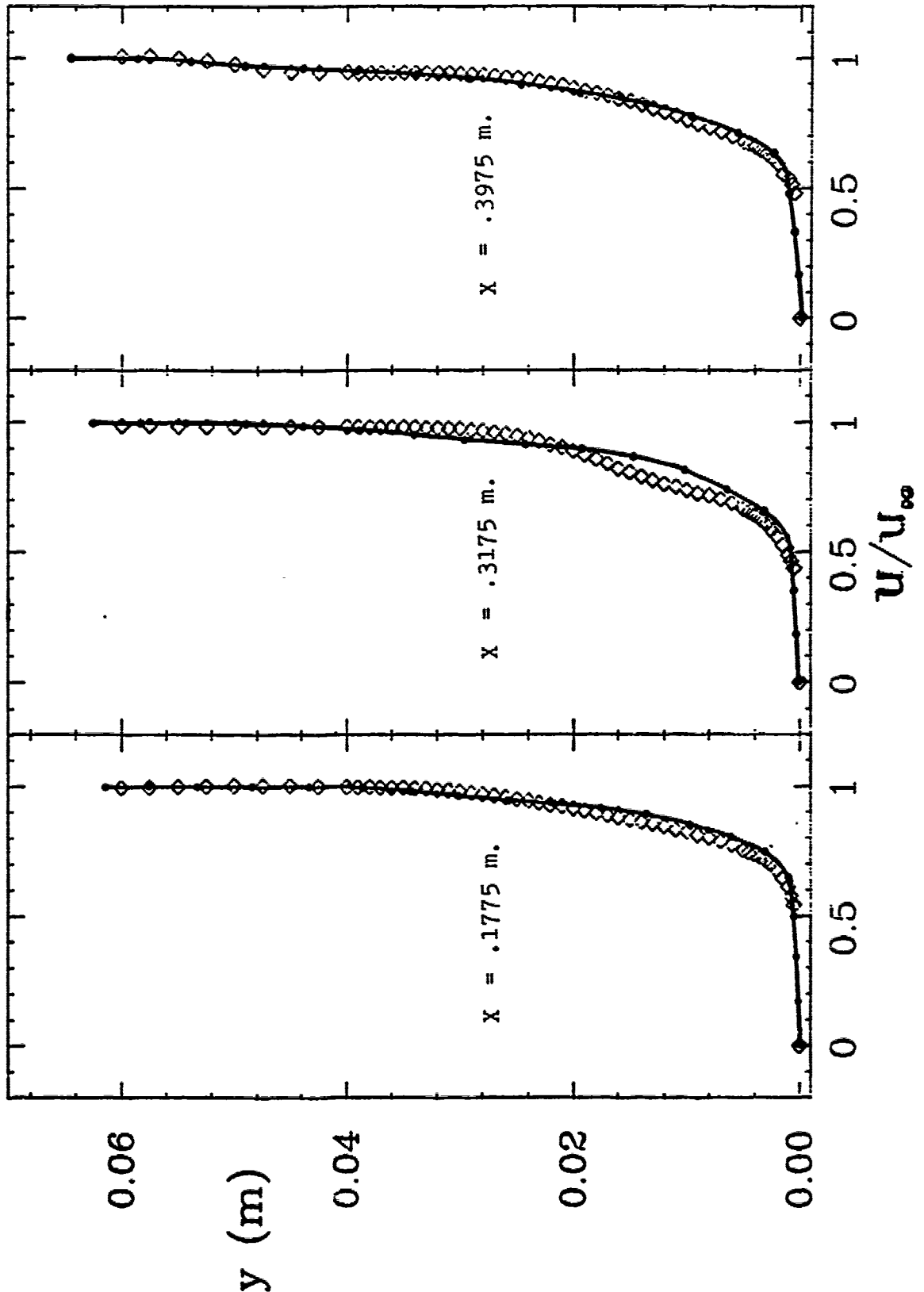


Figure 52. Mach 2.2 boundary layer with adverse pressure gradient.

PLOT 7 CASE 8403 FILES 33,37,39 CENTERBODY II

THE 1980-81 AFOSR-HTTM-STANFORD CONFERENCE ON COMPLEX TURBULENT FLOWS:
COMPARISON OF COMPUTATION AND EXPERIMENT

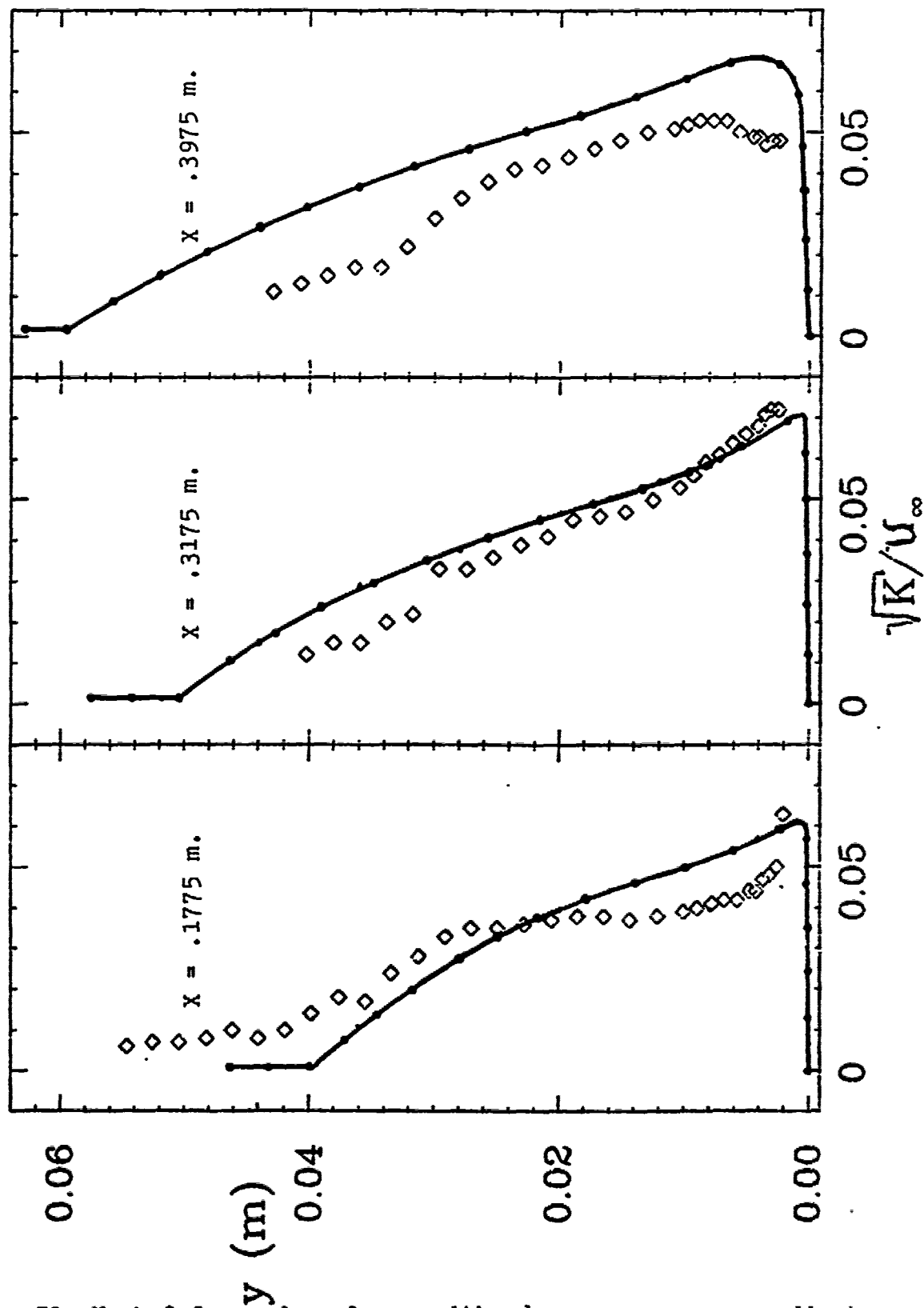


Figure 53. Mach 2.2 boundary layer with adverse pressure gradient.

PLOT 8 CASE 8403 FILES 33,37,39 CENTER BODY II

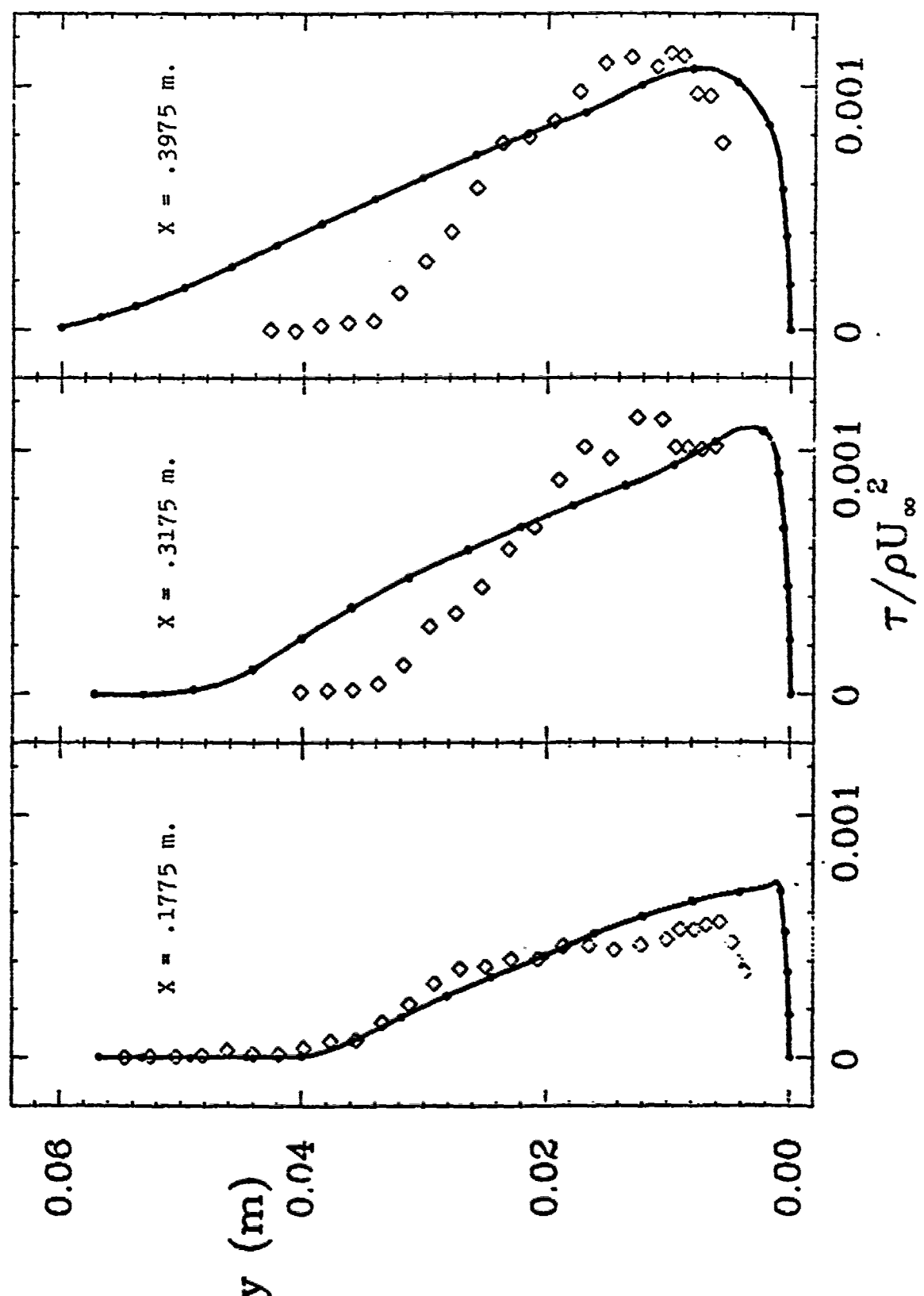


Figure 54. Mach 2.2 boundary layer with adverse pressure gradient.

PLOT 9 CASE 8403 FILES 24,28,30 CENTERBODY IV

THE 1980-81 AFOSR-HTTM-STANFORD CONFERENCE ON COMPLEX TURBULENT FLOWS:
COMPARISON OF COMPUTATION AND EXPERIMENT

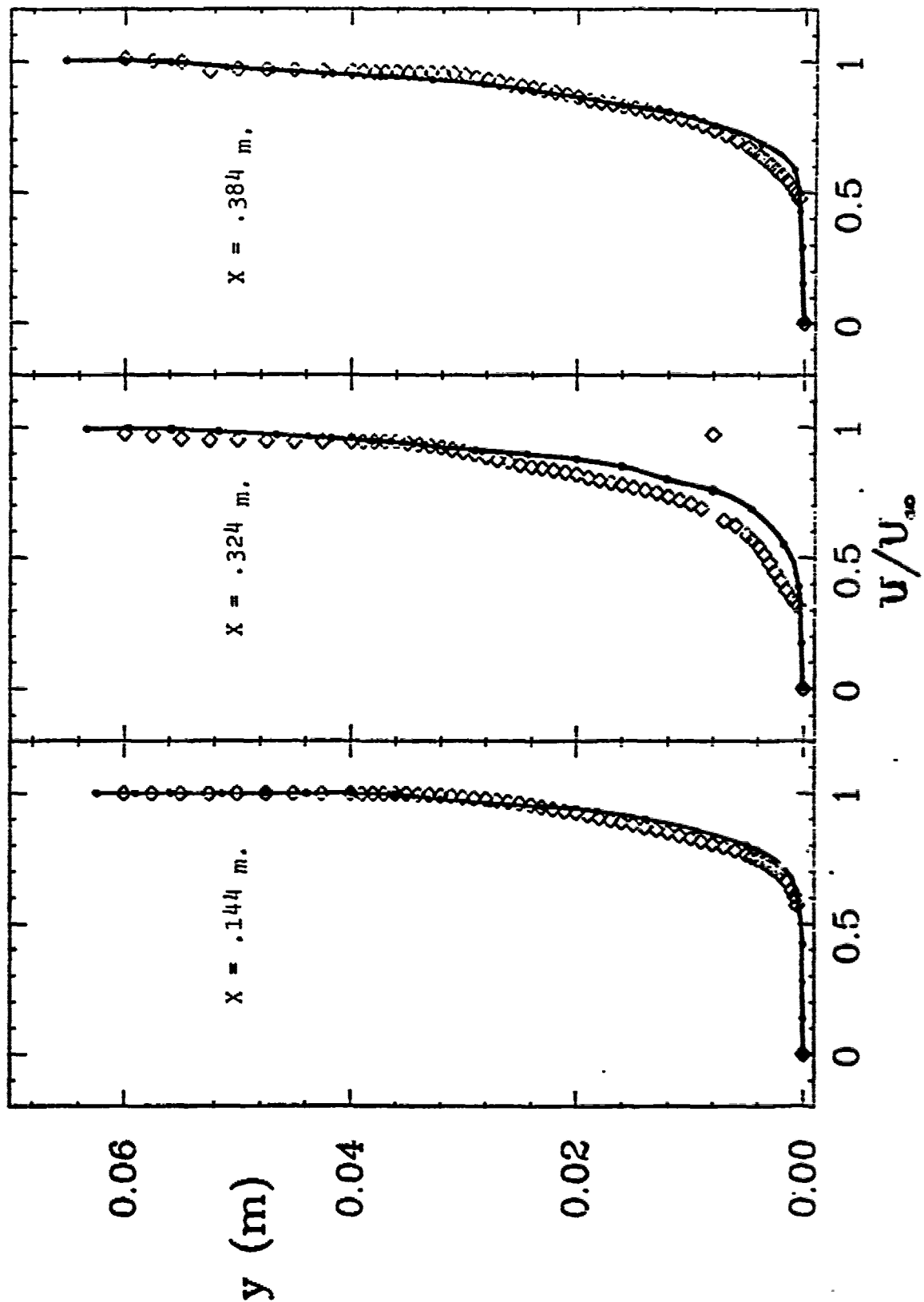


Figure 55. Mach 2.2 boundary layer with adverse pressure gradient.

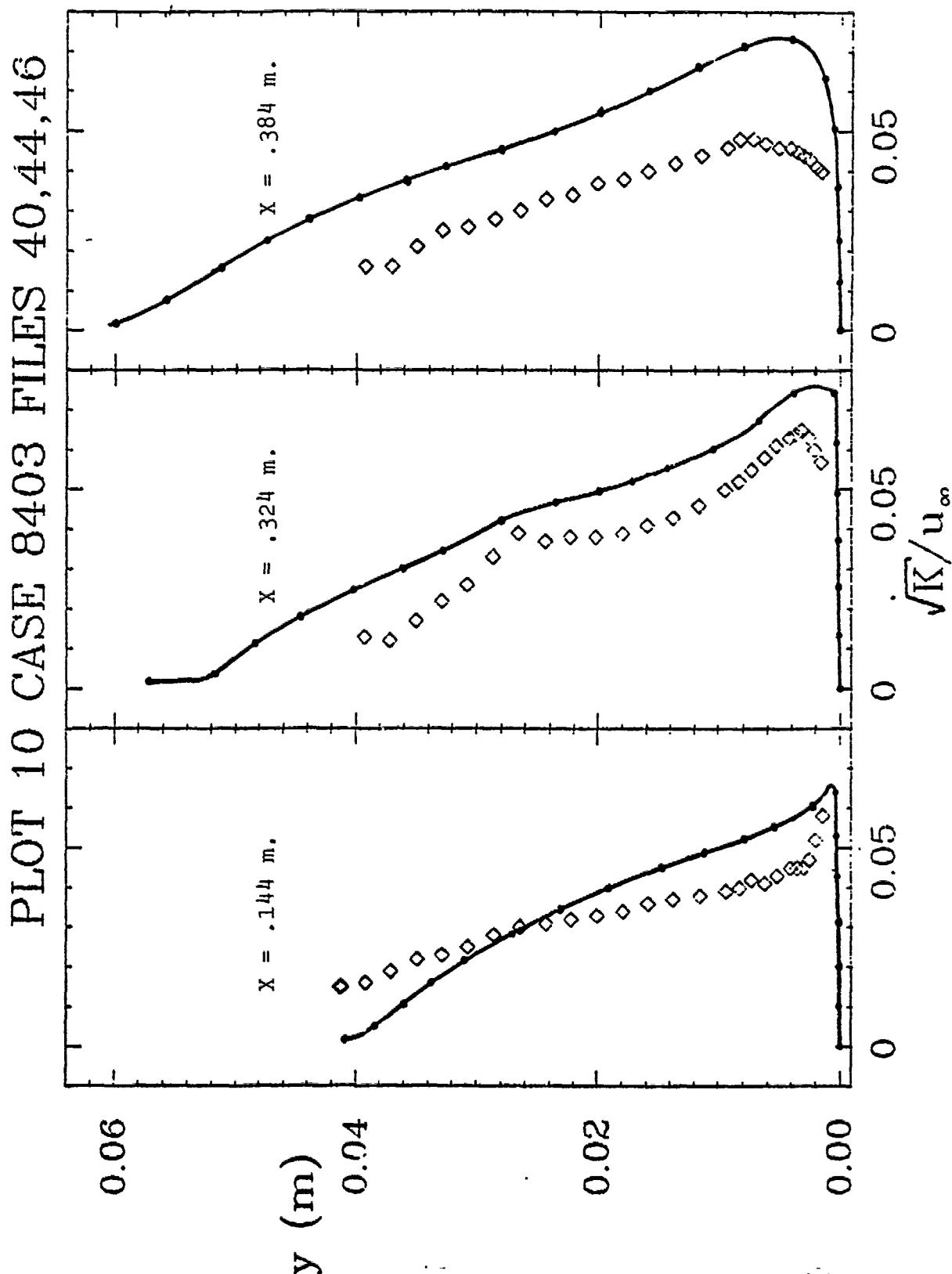


Figure 56. Mach 2.2 boundary layer with adverse pressure gradient.

PLOT 11 CASE 8403 FILES 40,44,46

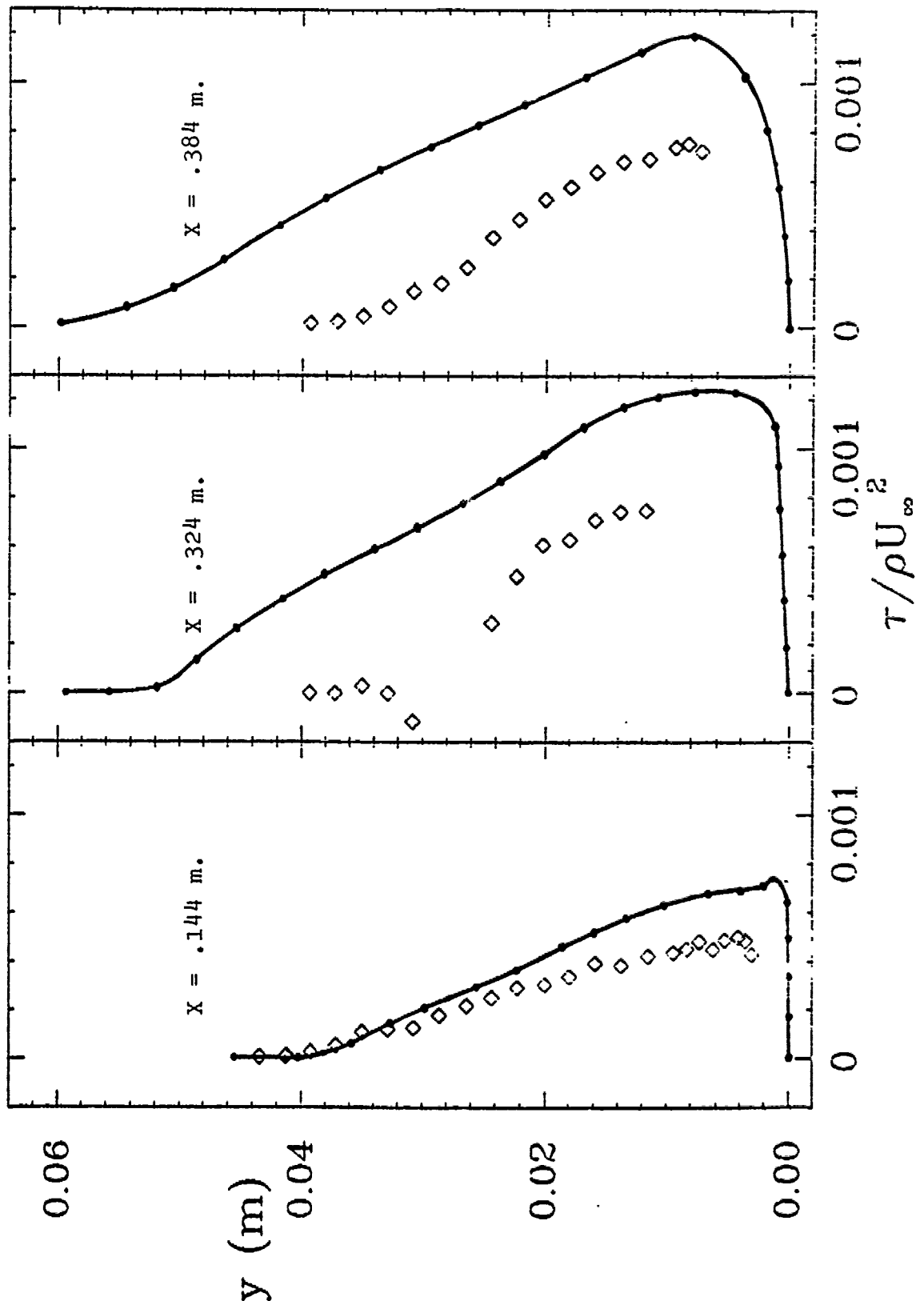


Figure 57. Mach 2.2 boundary layer with adverse pressure gradient.

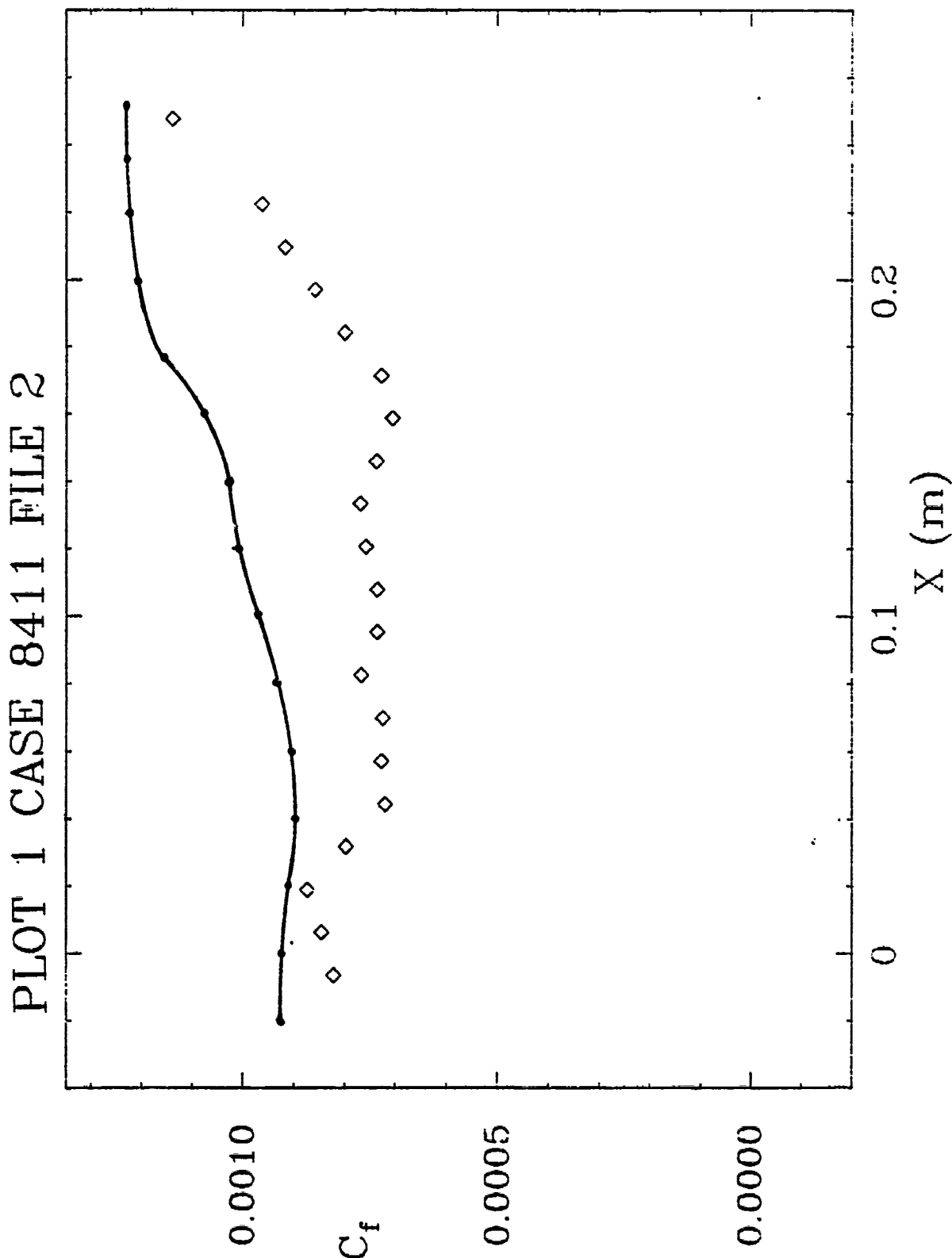


Figure 58. Mach 4 boundary layer with adverse pressure gradient.

PLOT 2 CASE. 8411 FILE 2

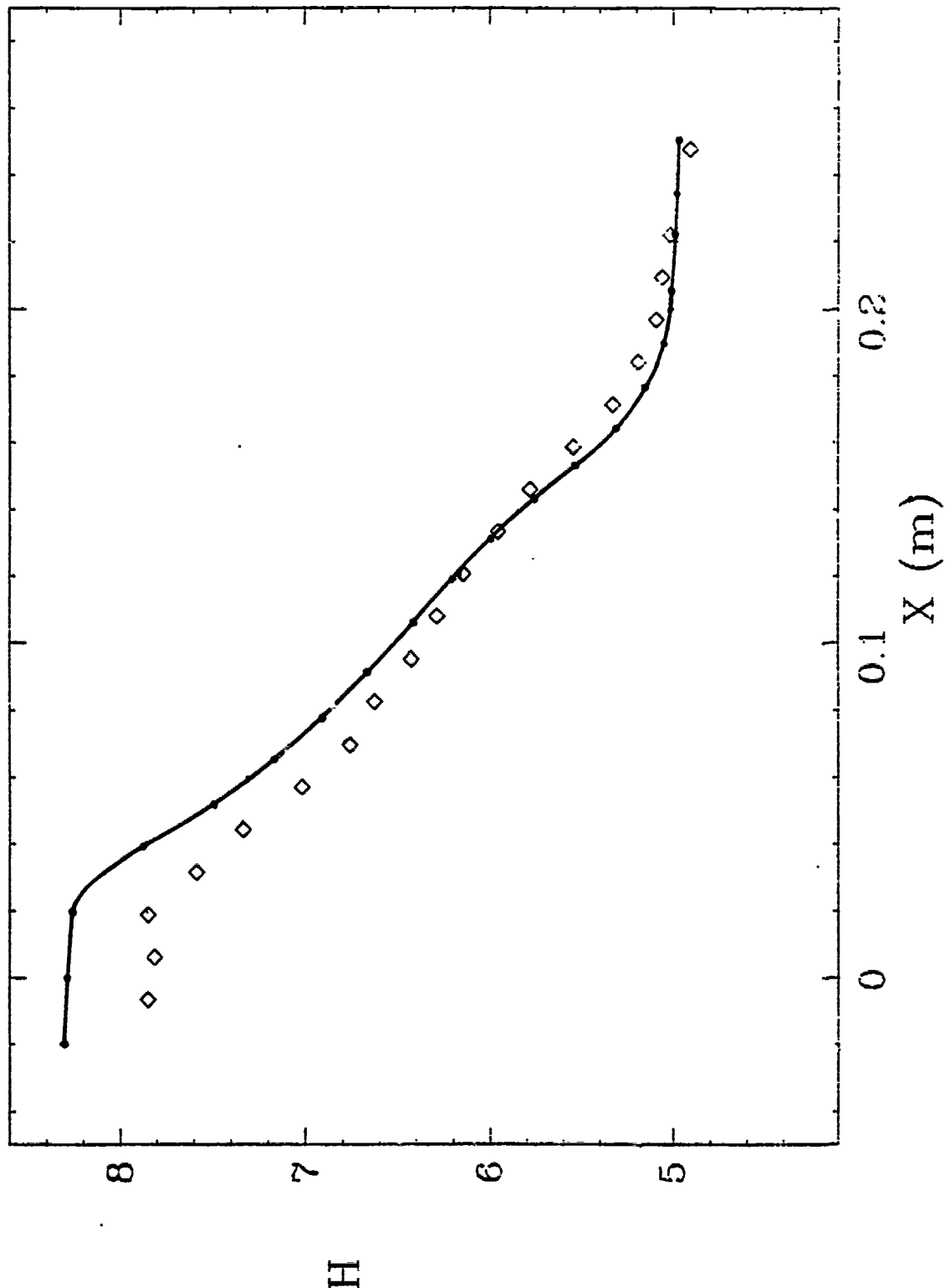


Figure 59. Mach 4 boundary layer with adverse pressure gradient.

PLOT 3 CASE 8411 FILE 2

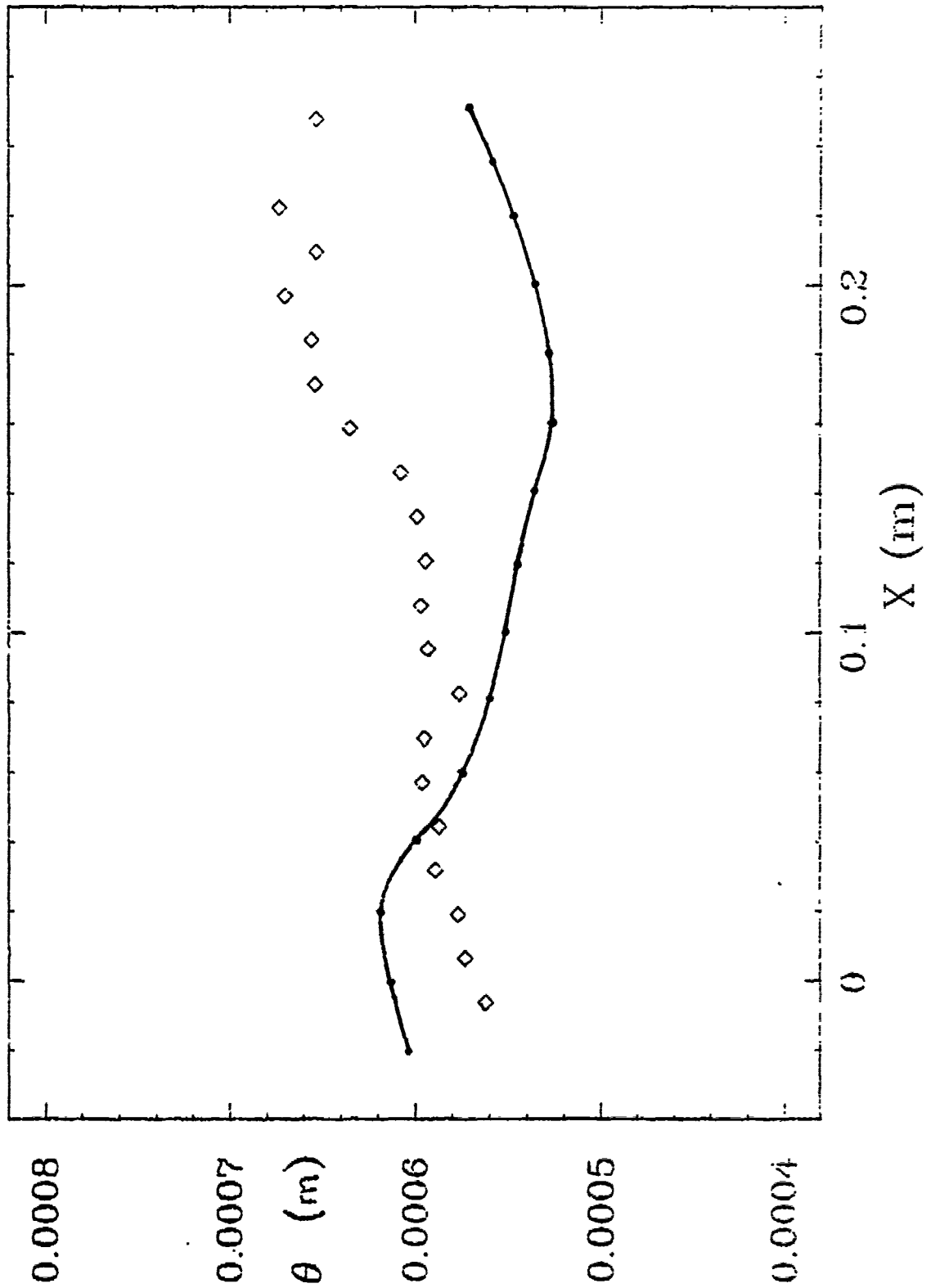


Figure 60. Mach 4 boundary layer with adverse pressure gradient.

PLOT 4 CASE 8411 FILES 3,5,7

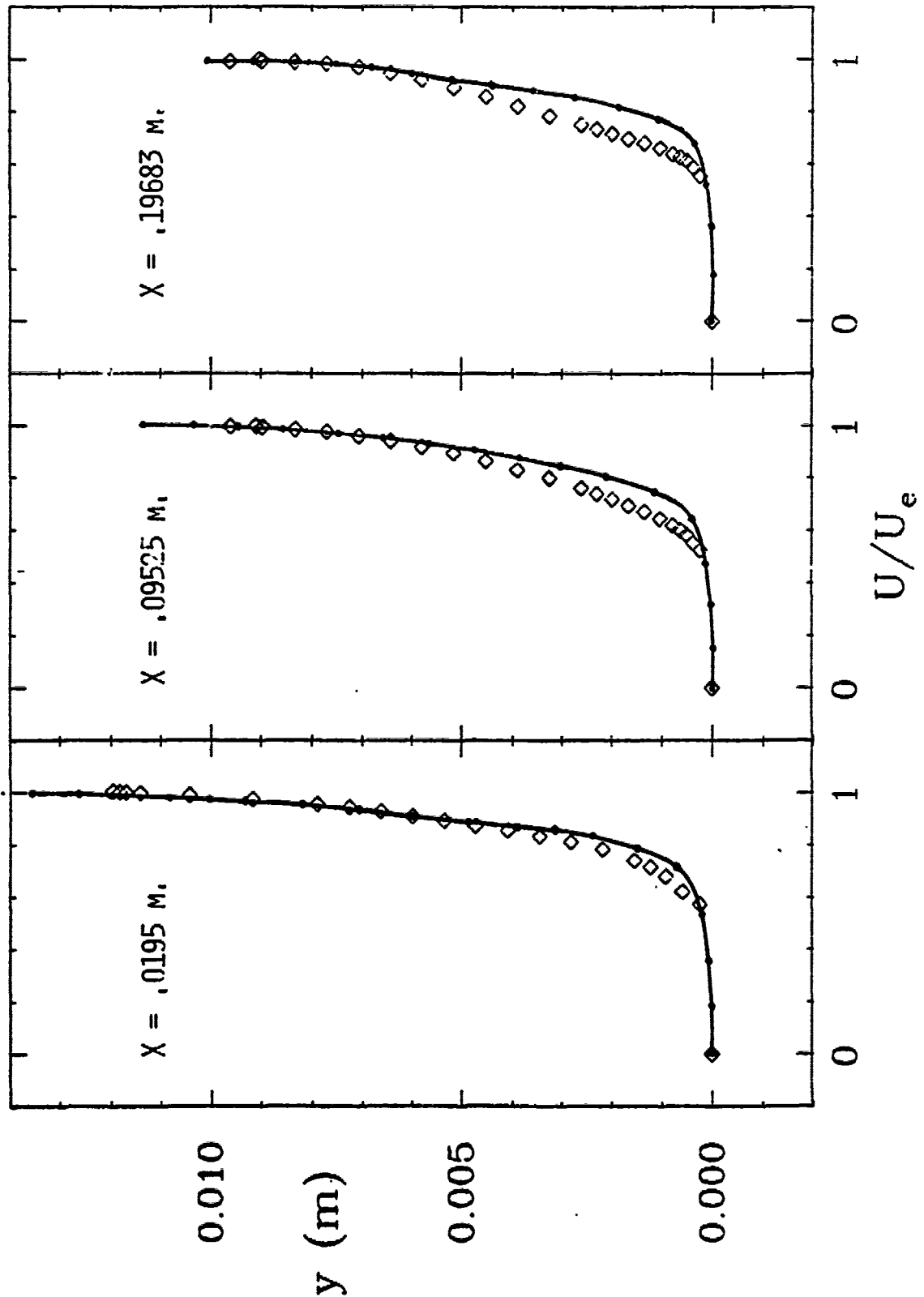


Figure 61. Mach 4 boundary layer with adverse pressure gradient.

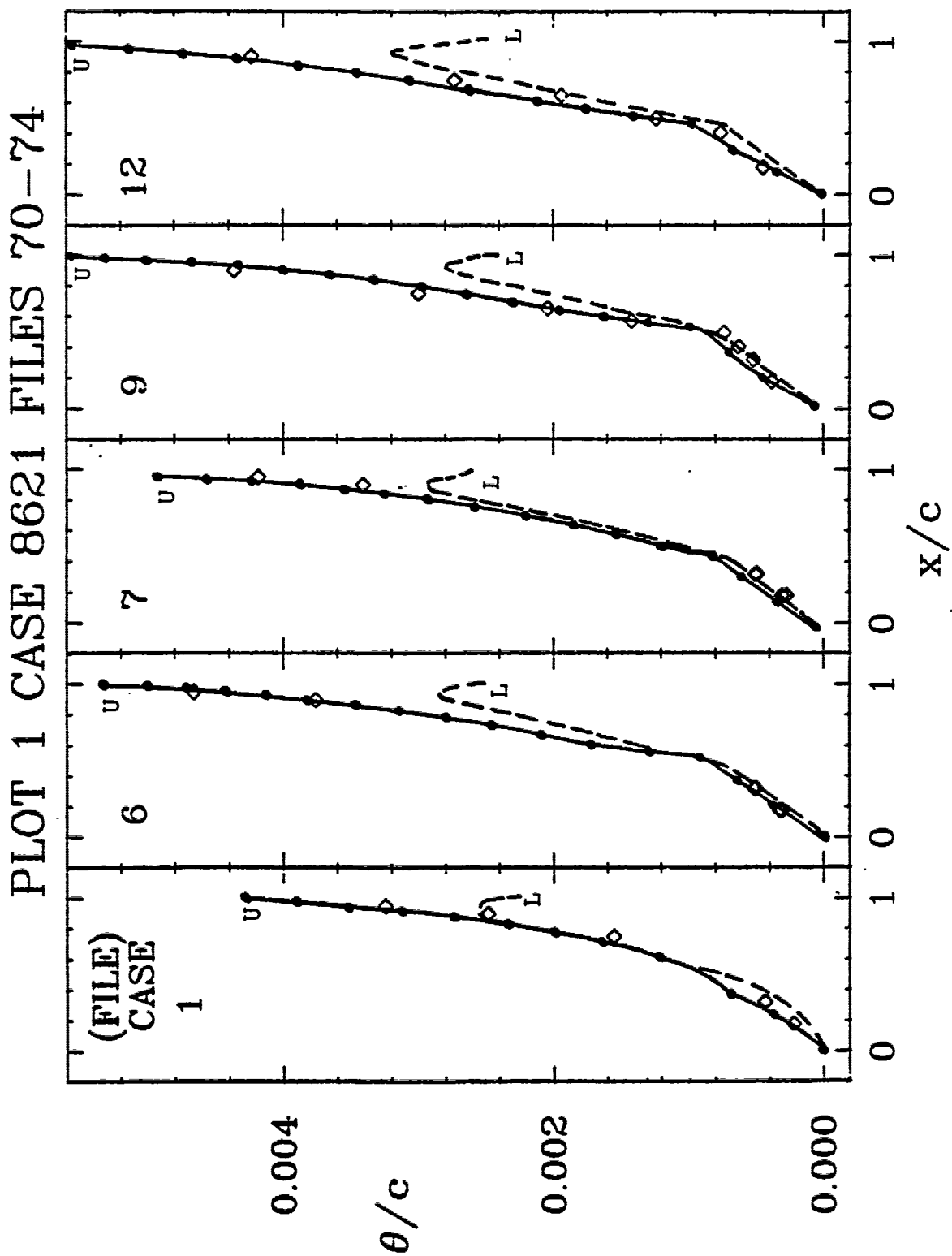


Figure 62. Transonic airfoil RAE 2822.

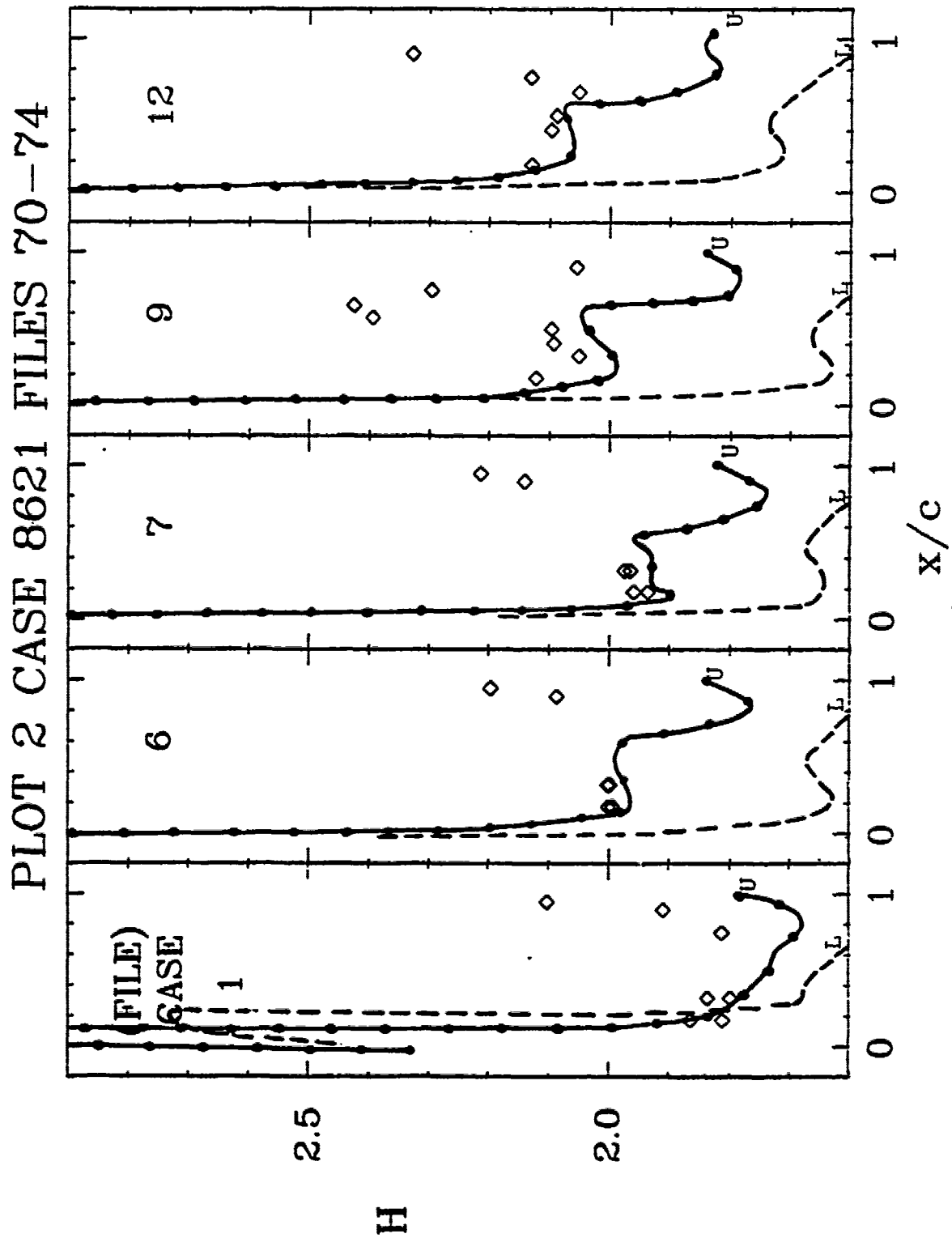


Figure 63. Transonic airfoil RAE 2822.

PLOT 3 CASE 8621 FILES 70-74

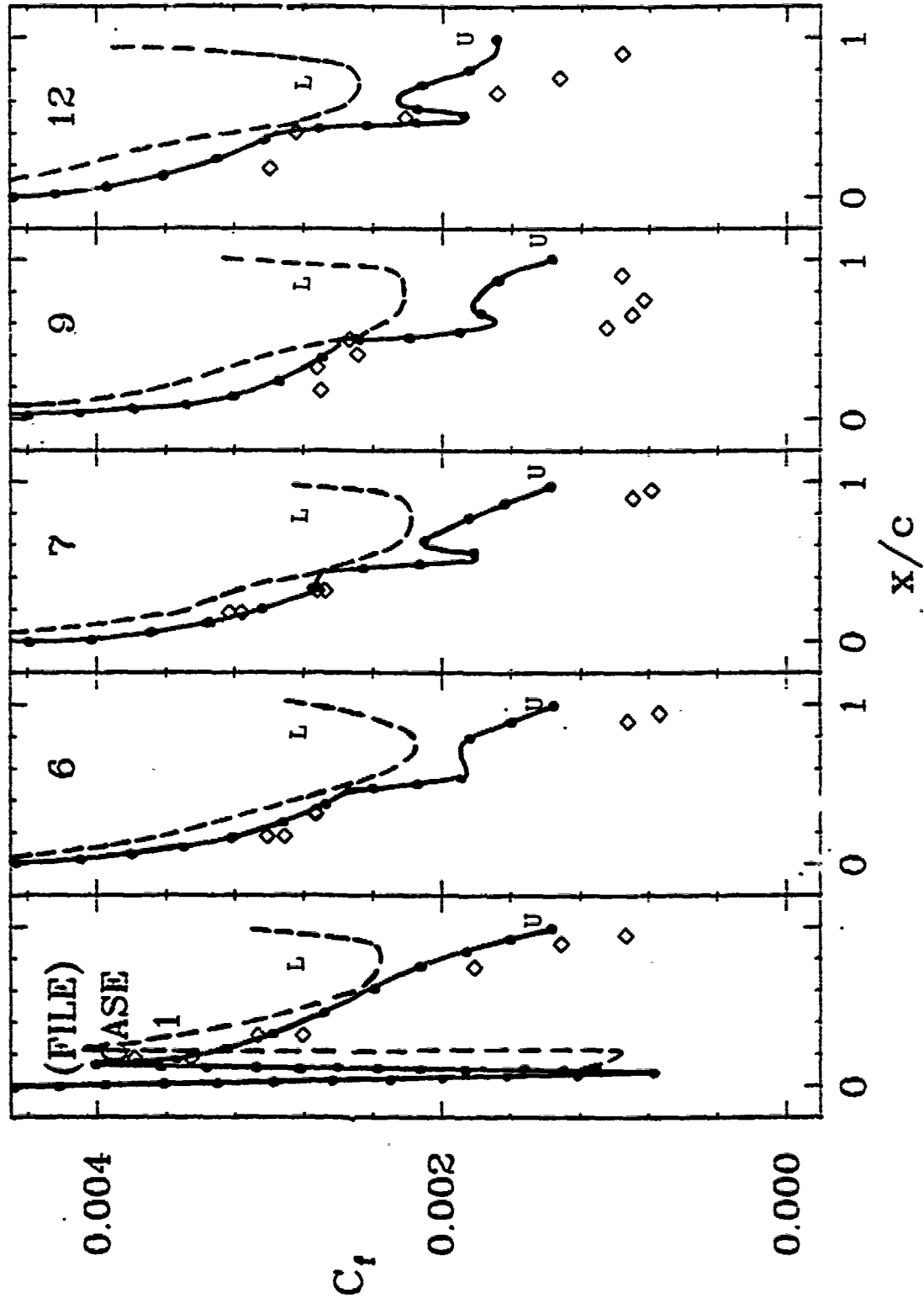


Figure 64. Transonic airfoil RAE 2822.

CASE 1

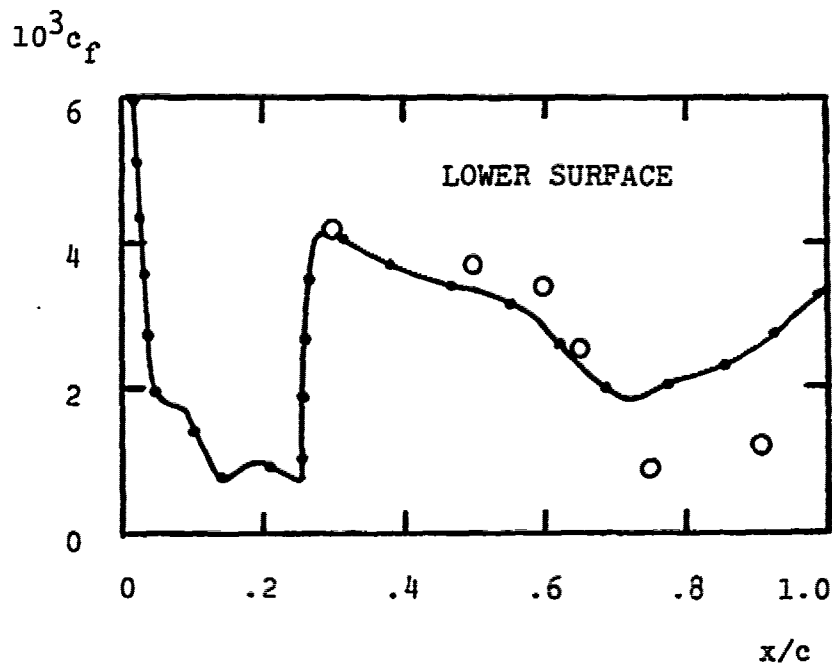
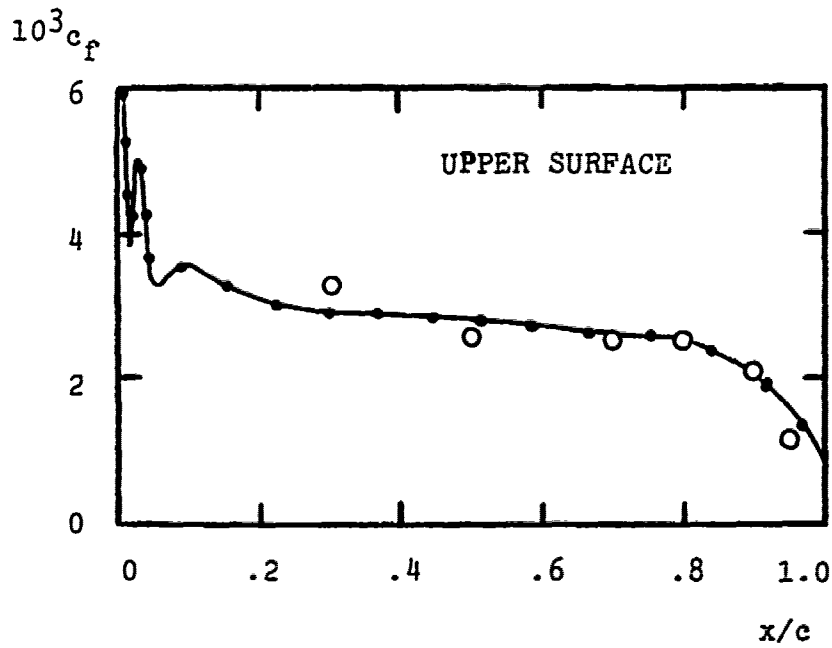


Figure 65. Airfoil DSMA 523s; Mach .6; $Re_c = 4$ million.

CASE 2

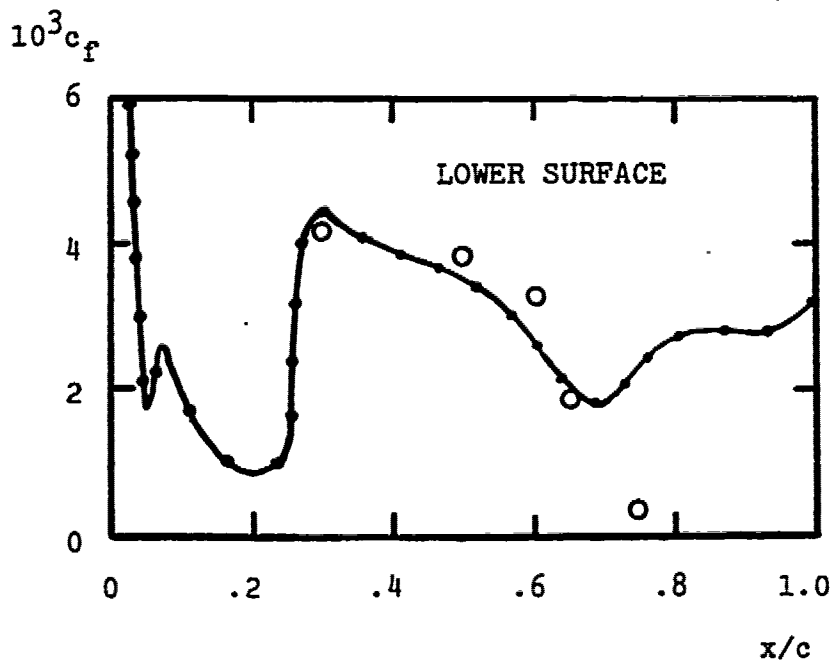
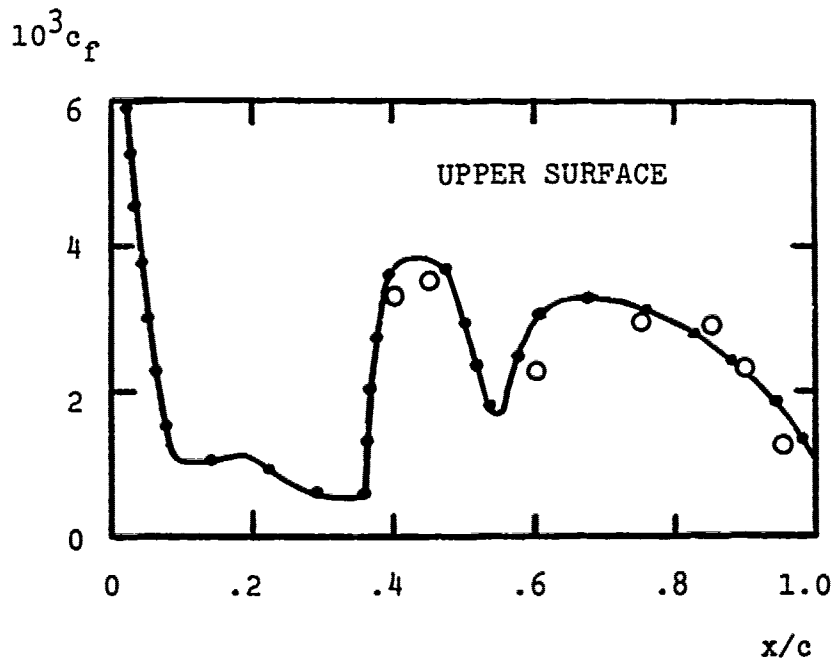


Figure 66. Airfoil DSMA 523s; Mach .8; $Re_c = 2$ million.

CASE 3

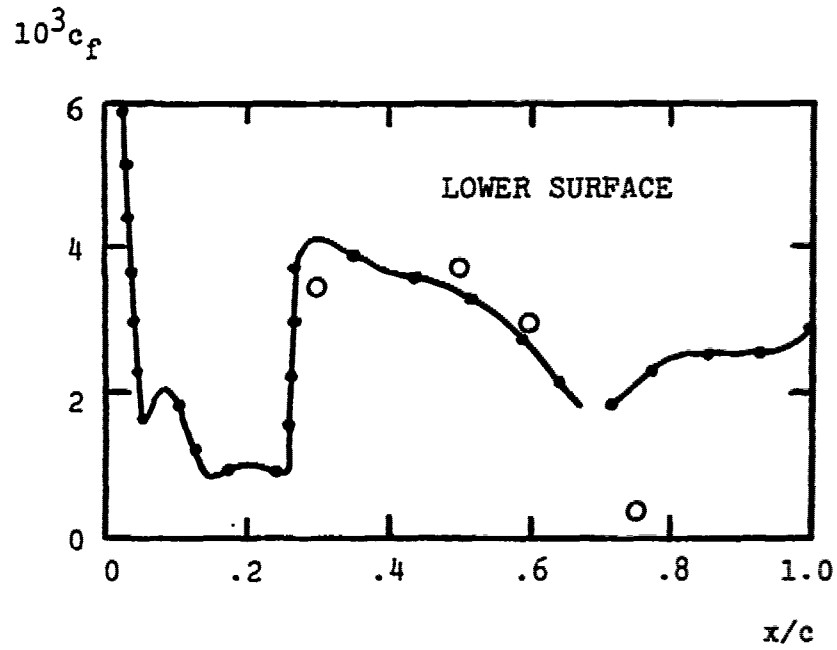
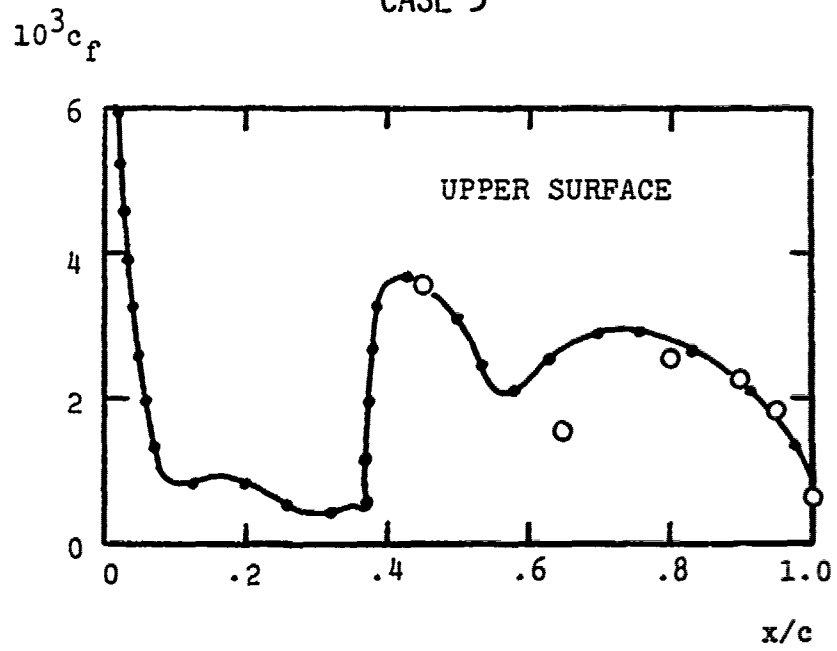


Figure 67. Airfoil DSMA 523s; Mach .8; $Re_c = 3$ million.

PLOT 1 CASE 8623 FILES 6,7,8,9,11

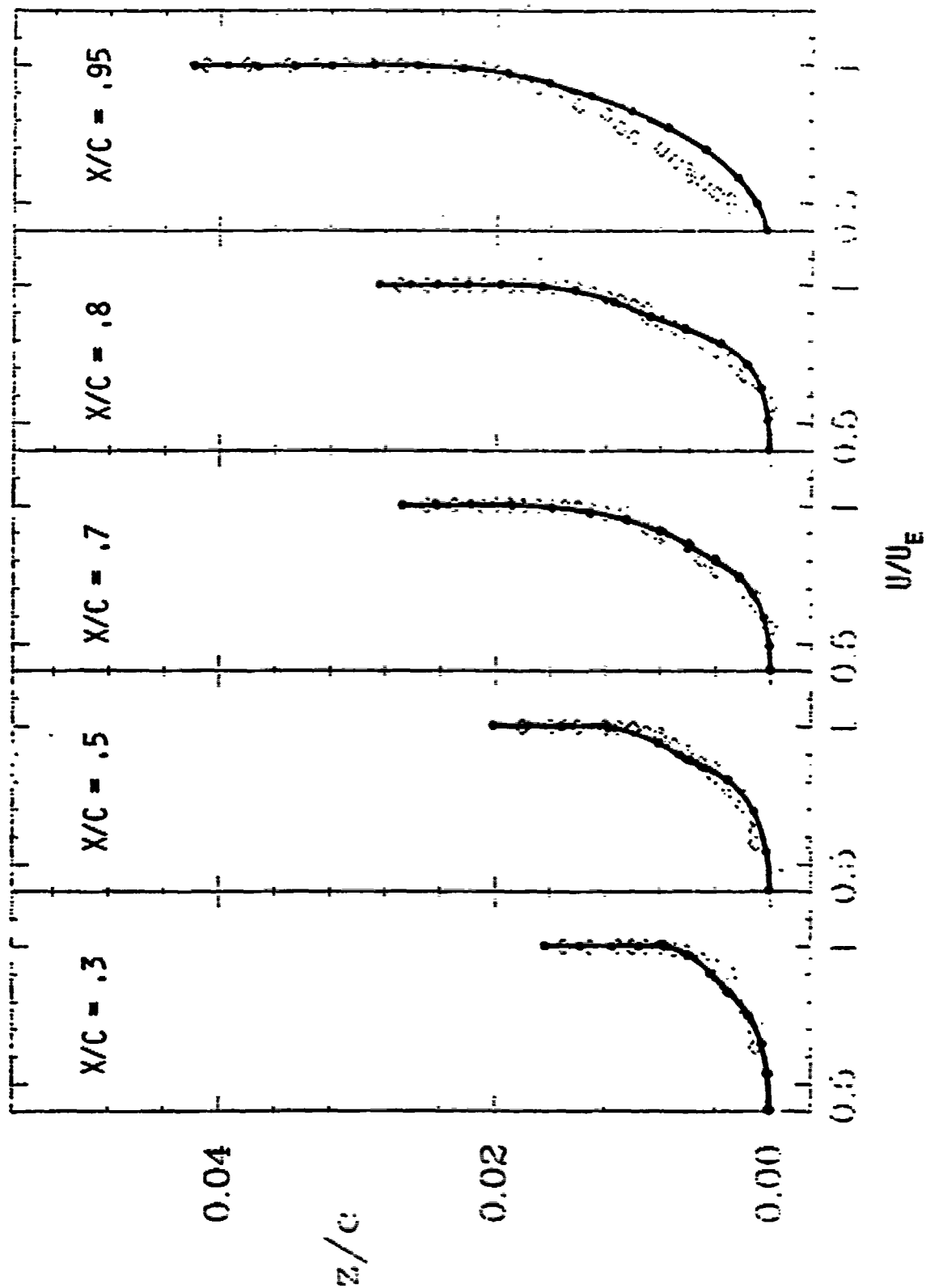


Figure 68. Airfoil DSMA 523s; Case 1; Upper surface.

THE 1980-81 AFOSR-HTTM-STANFORD CONFERENCE ON COMPLEX TURBULENT FLOWS:
COMPARISON OF COMPUTATION AND EXPERIMENT

PLOT 2 CASE 8623 FILES 14, 15, 17, 18, 19

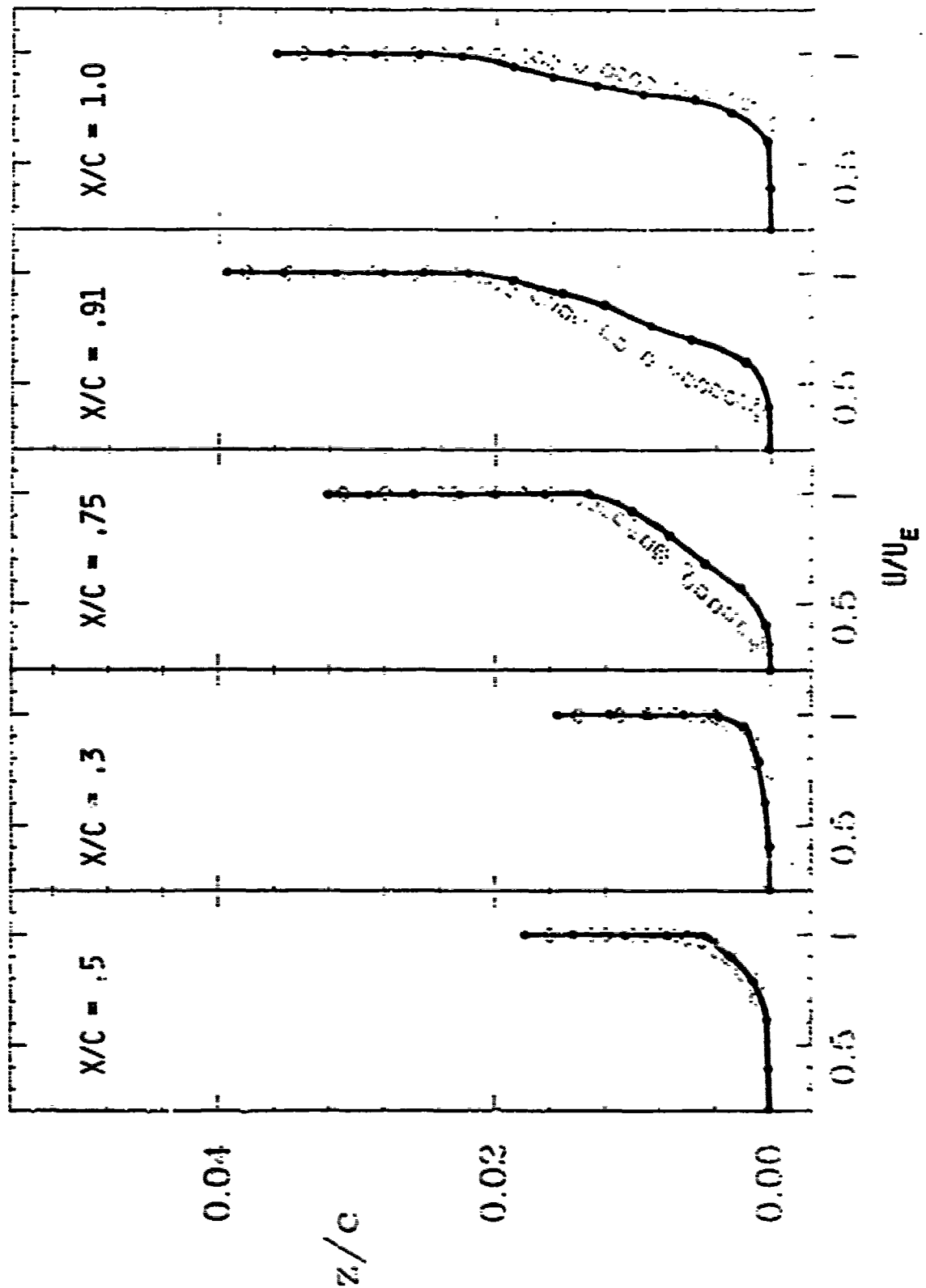


Figure 69. Airfoil DSMA 523s; Case 1; Lower surface.

PLOT 3 CASE 8623 FILES 20,24,25,22,27

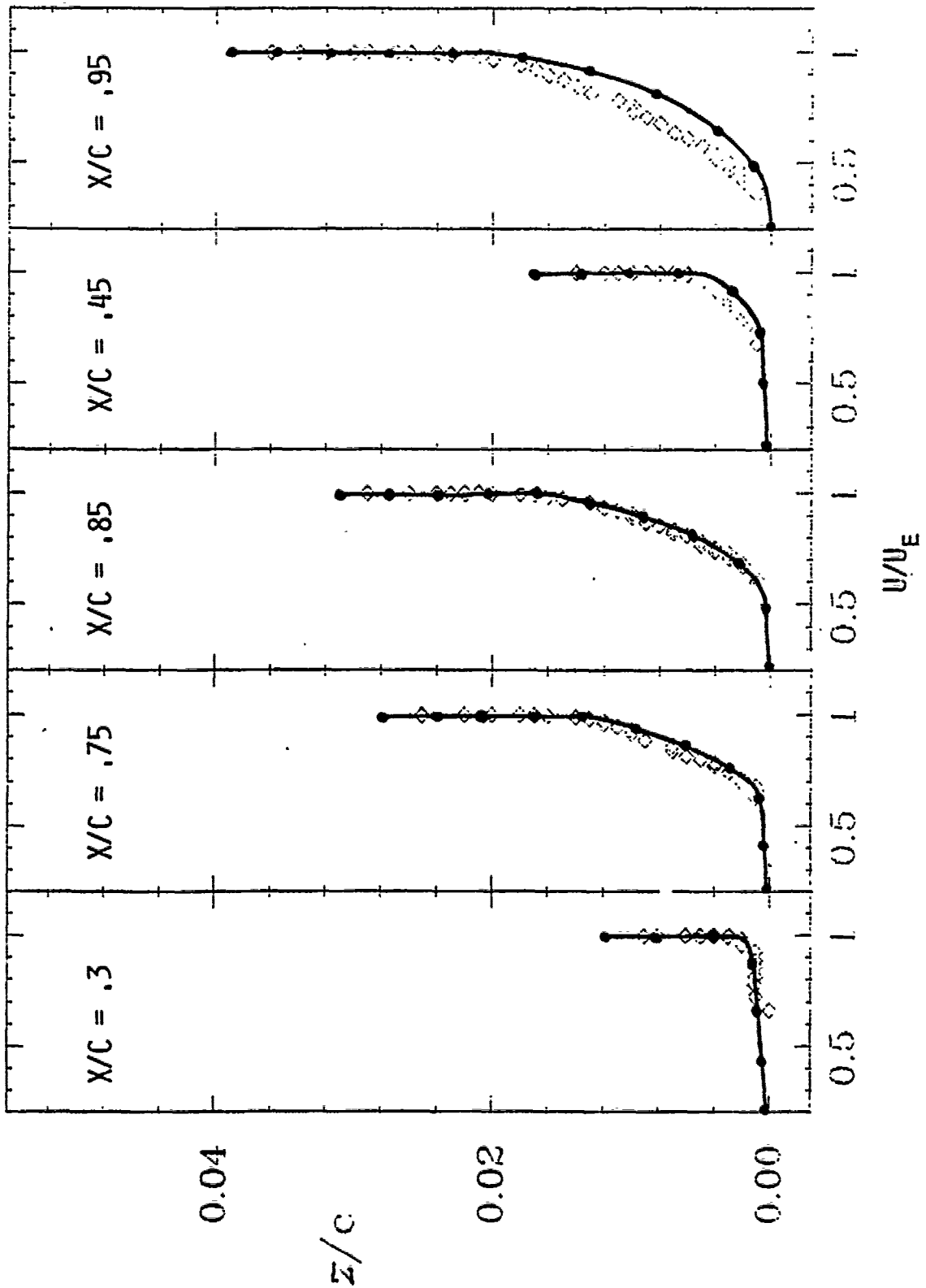


Figure 70. Airfoil DSMA 523s; Case 2; Upper surface.

PLOT 4 CASE 8623 FILES 29,30,32,33,34

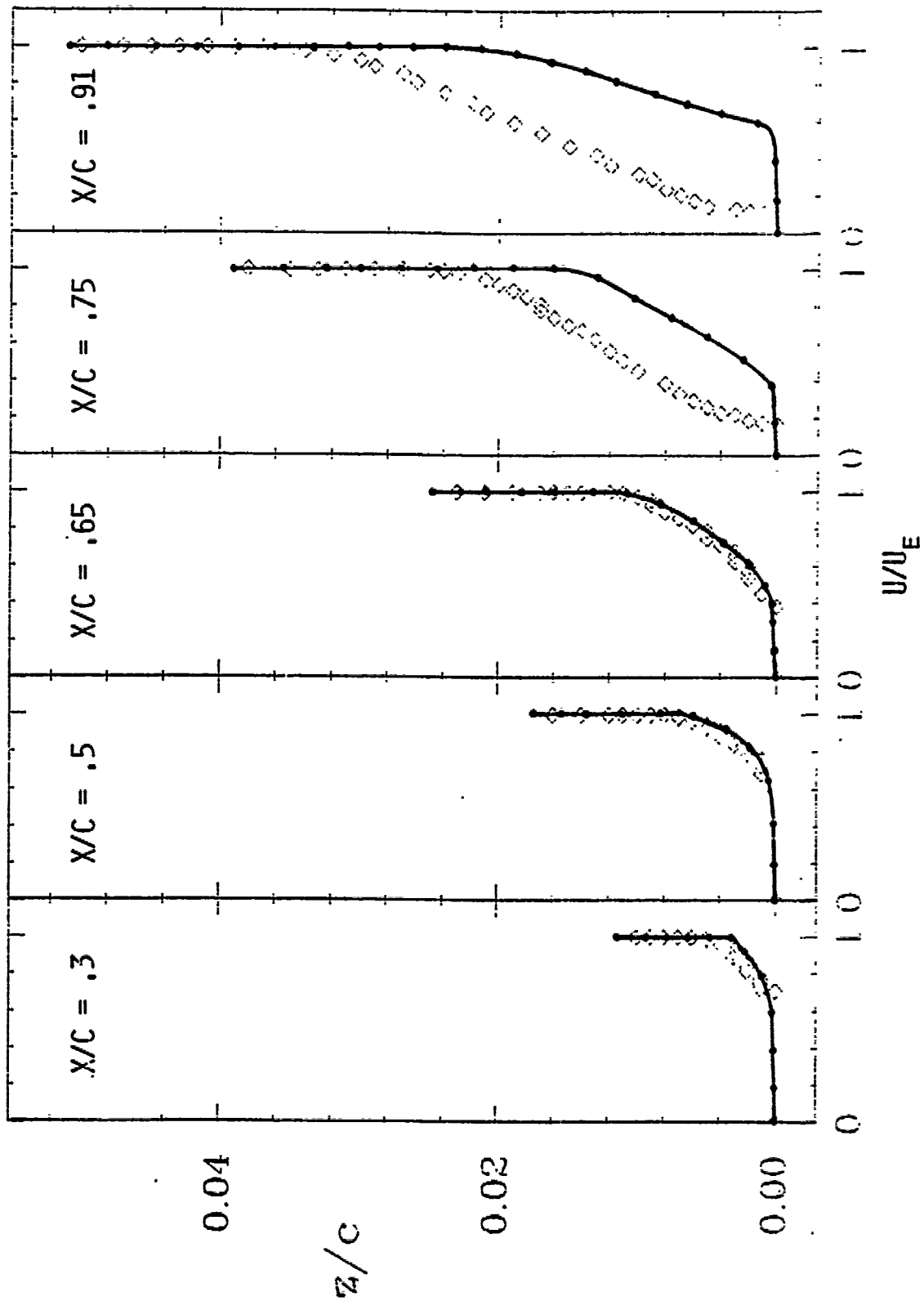


Figure 71. Airfoil DSMA 523s; Case 2; Lower surface.

PLOT 5 CASE 8623 FILES 36,37,38,39,40

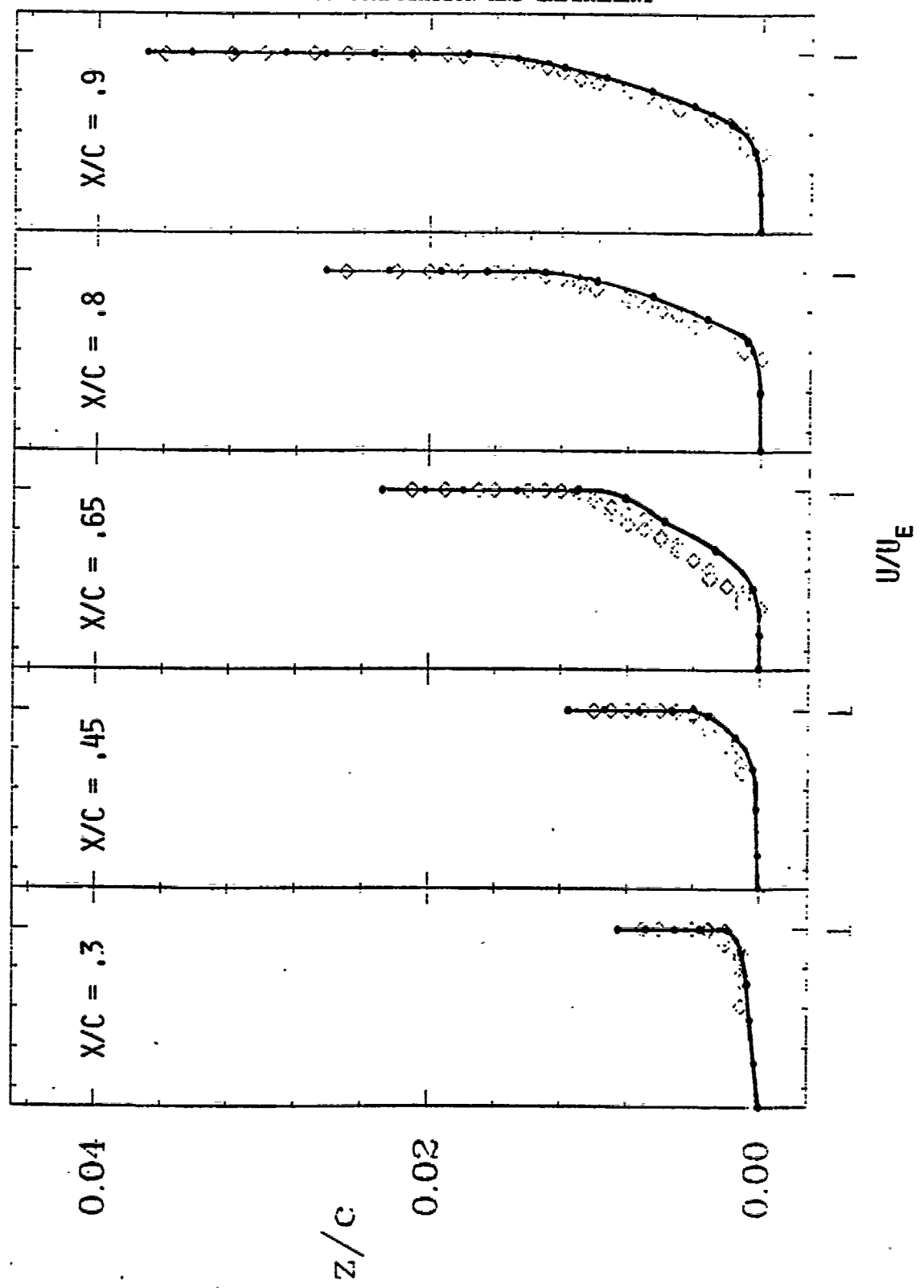


Figure 72. Airfoil DSMA 523s; Case 3; Upper surface.

THE 1980-81 AFOSR-HTTM-STANFORD CONFERENCE ON COMPLEX TURBULENT FLOWS:
COMPARISON OF COMPUTATION AND EXPERIMENT

PLOT 6 CASE 8623 FILES 43,44,46,47,48

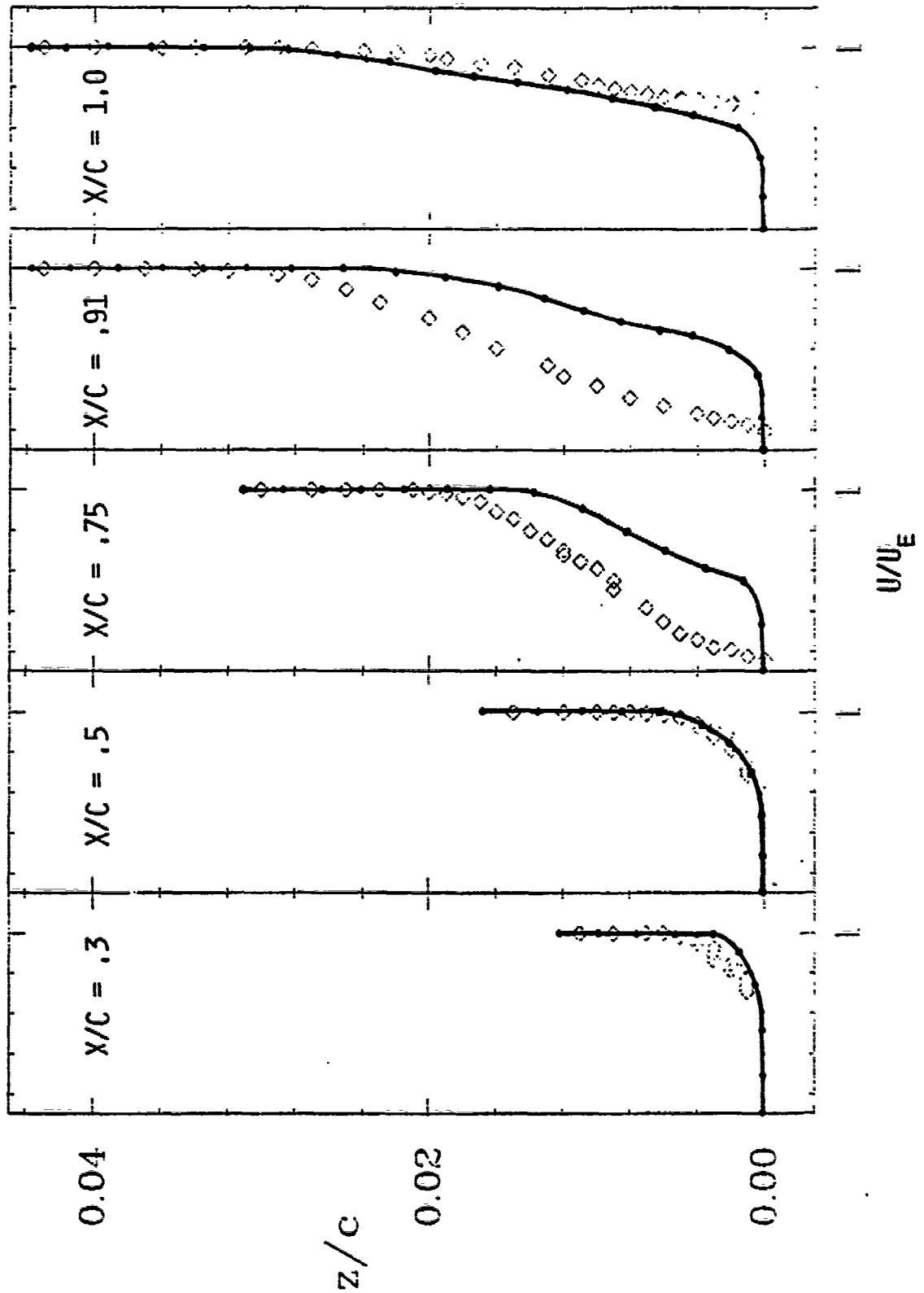


Figure 73. Airfoil DSMA 523s; Case 3; Lower surface.

PLOT 1 CASE 0142 FILE 2

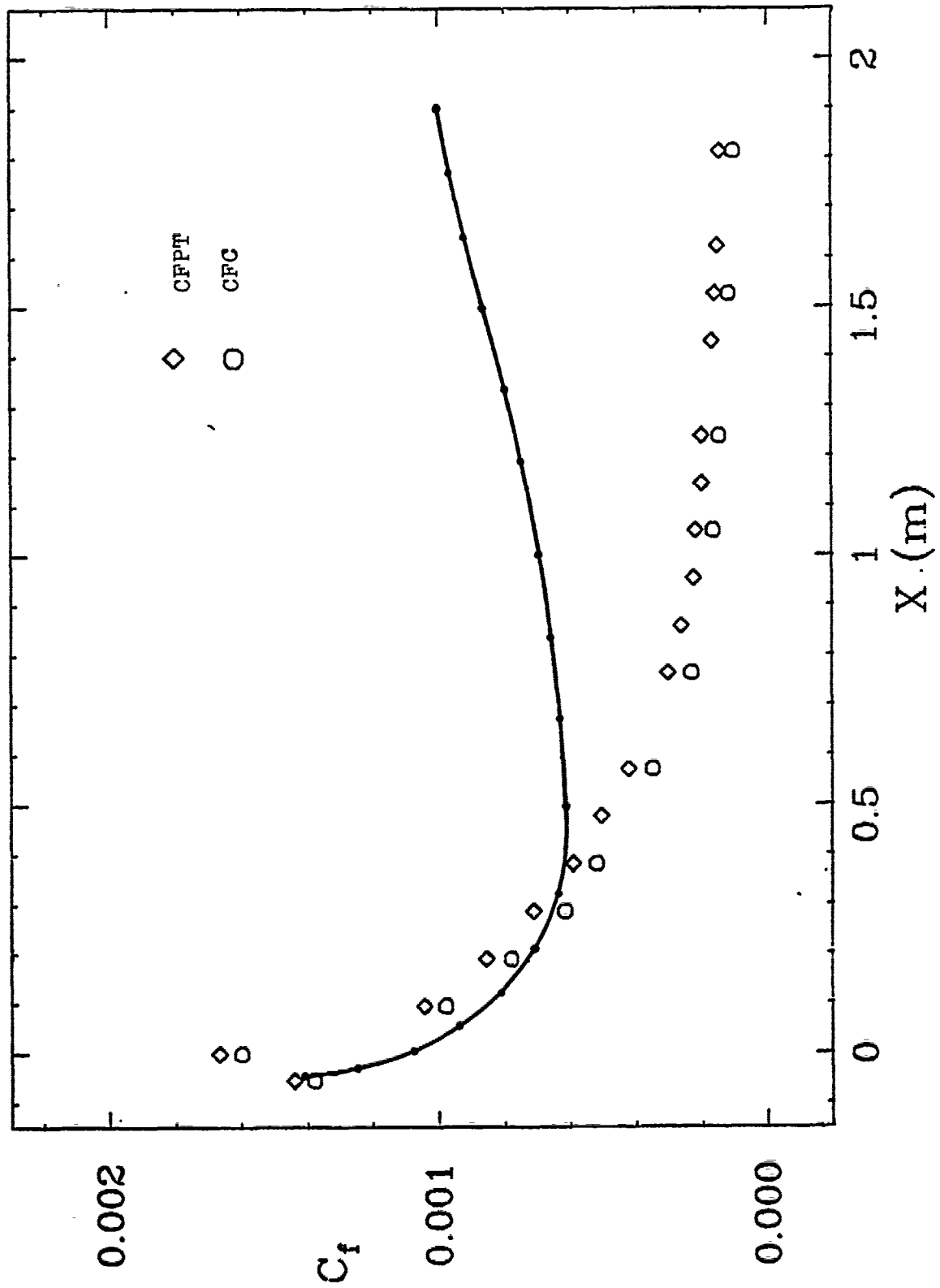


Figure 74. Diffuser flow with low-core turbulence.

PLOT 3 CASE 0142 FILES' 22,27

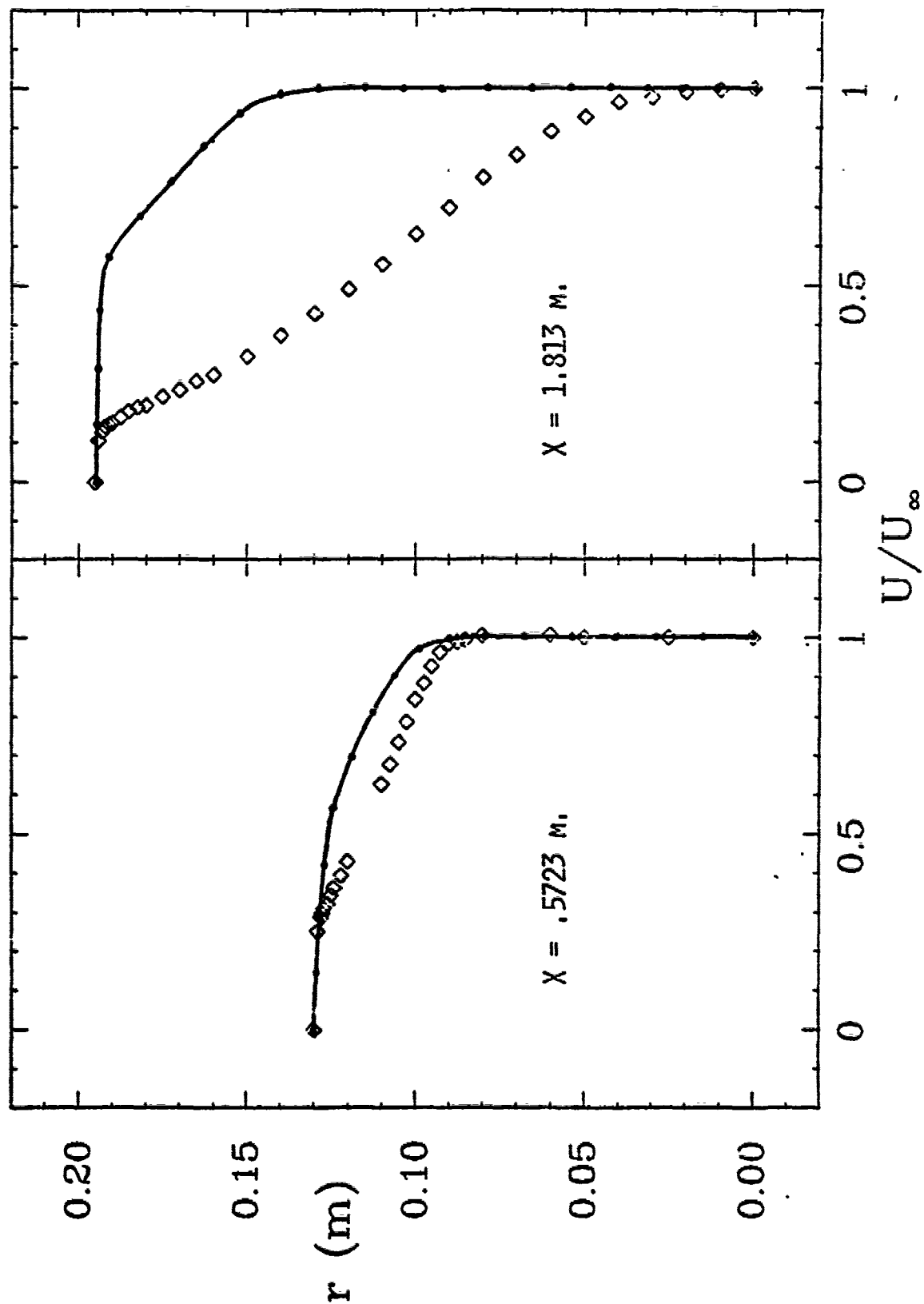


Figure 75. Diffuser flow with low-core turbulence.

PLOT 4 CASE 0142 FILES 16,19,22,24,27:

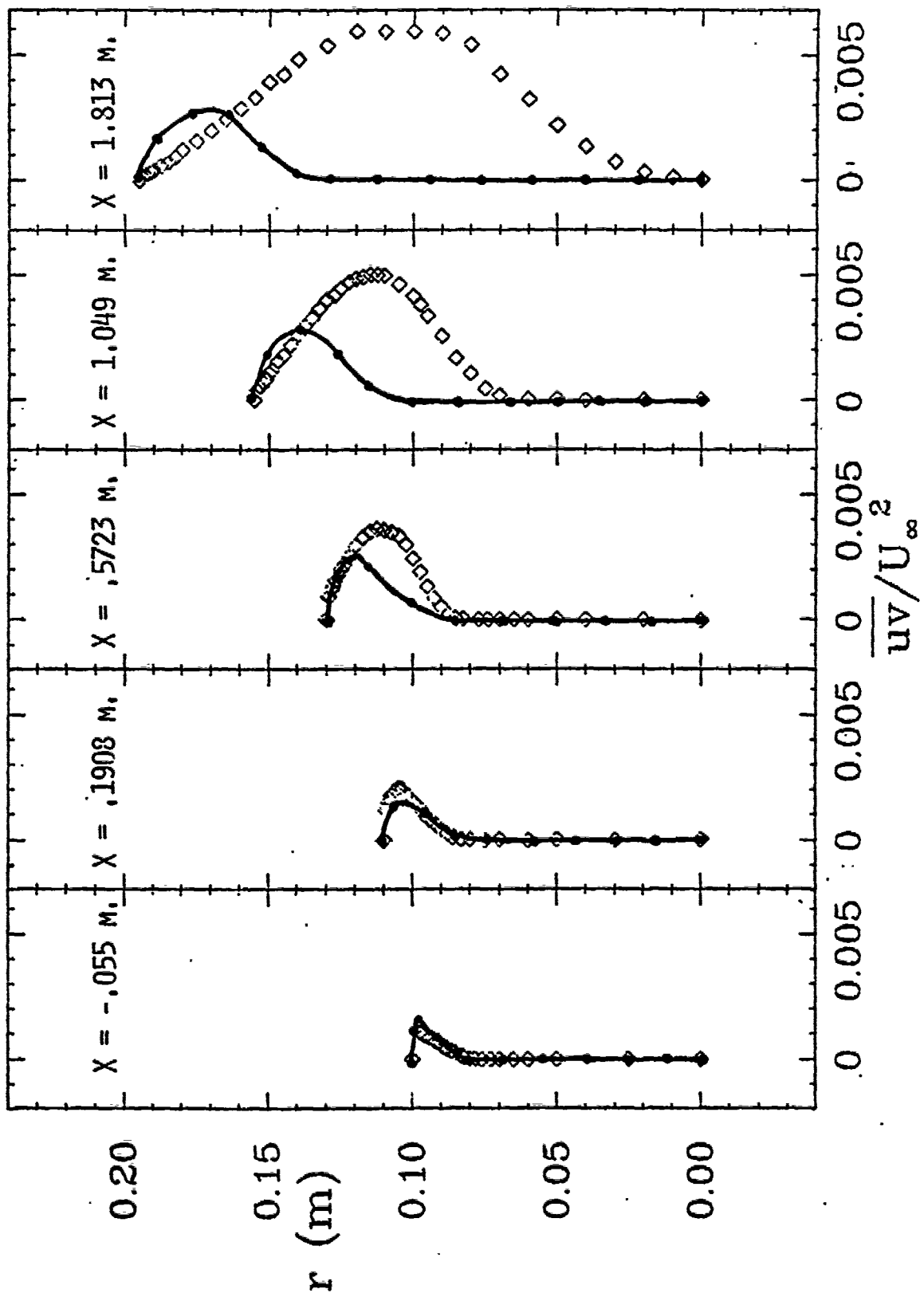


Figure 76. Diffuser flow with low-core turbulence.

PLOT 1 CASE 0143 FILE 28

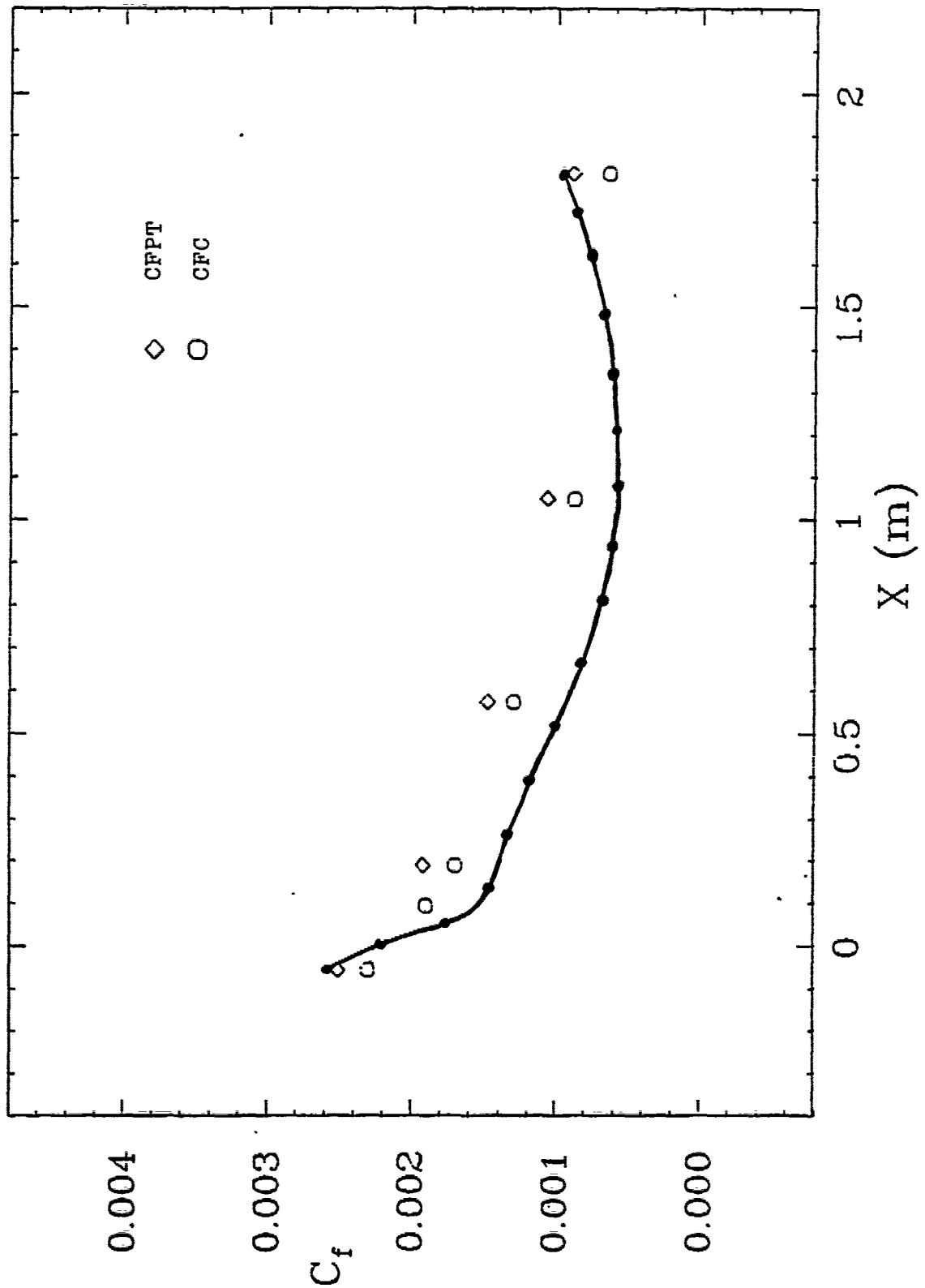


Figure 77. Diffuser flow with high-core turbulence.

PLOT 3 CASE 0143 FILES' 37,39

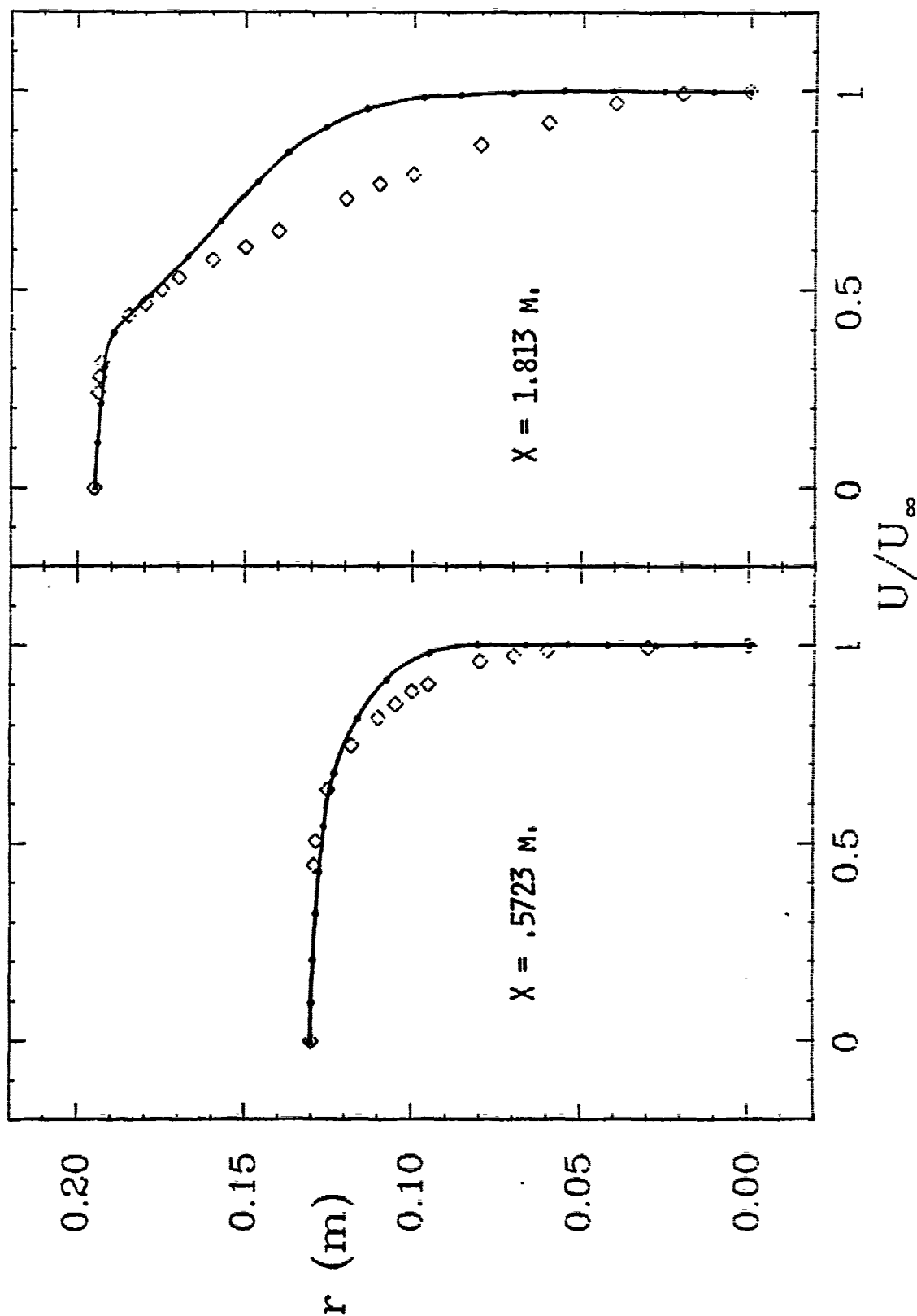


Figure 78. Diffuser flow with high-core turbulence.

PLOT 4 CASE 0143 FILES 35,36,37,38,39

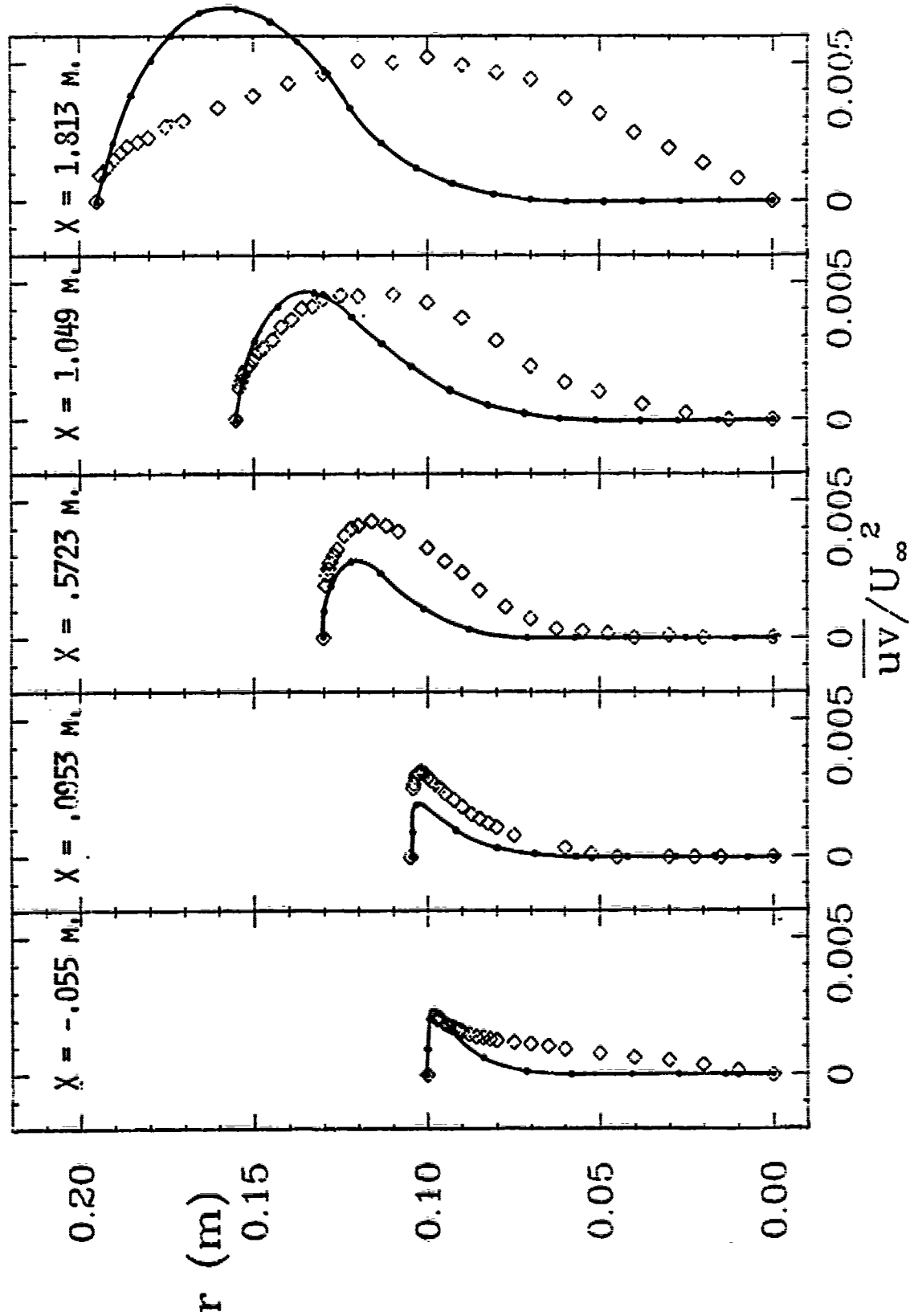


Figure 79. Diffuser flow with high-core turbulence.

PLOT 1 CASE 0421 FILES 2-3

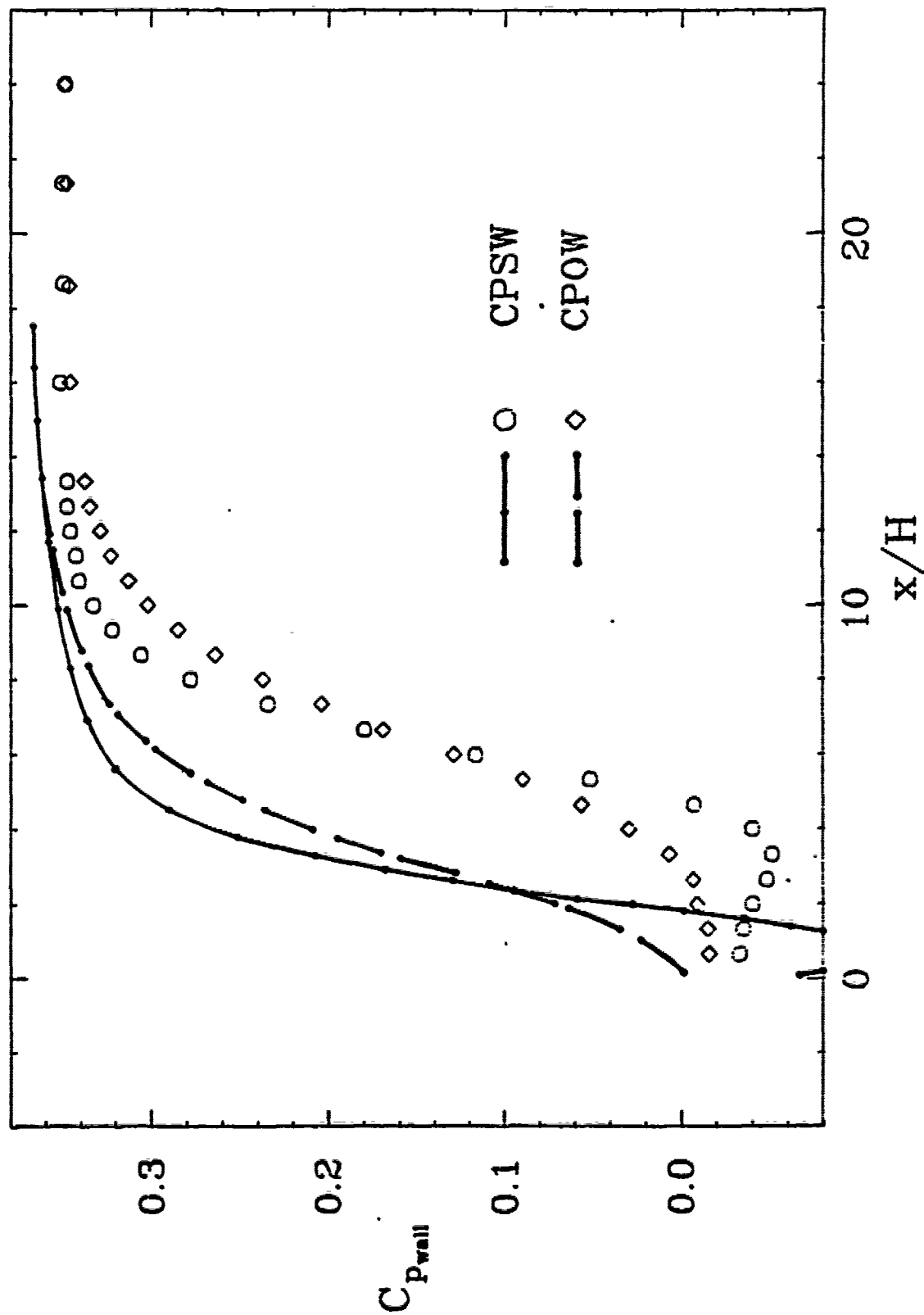


Figure 80. Flow past a backward-facing step.

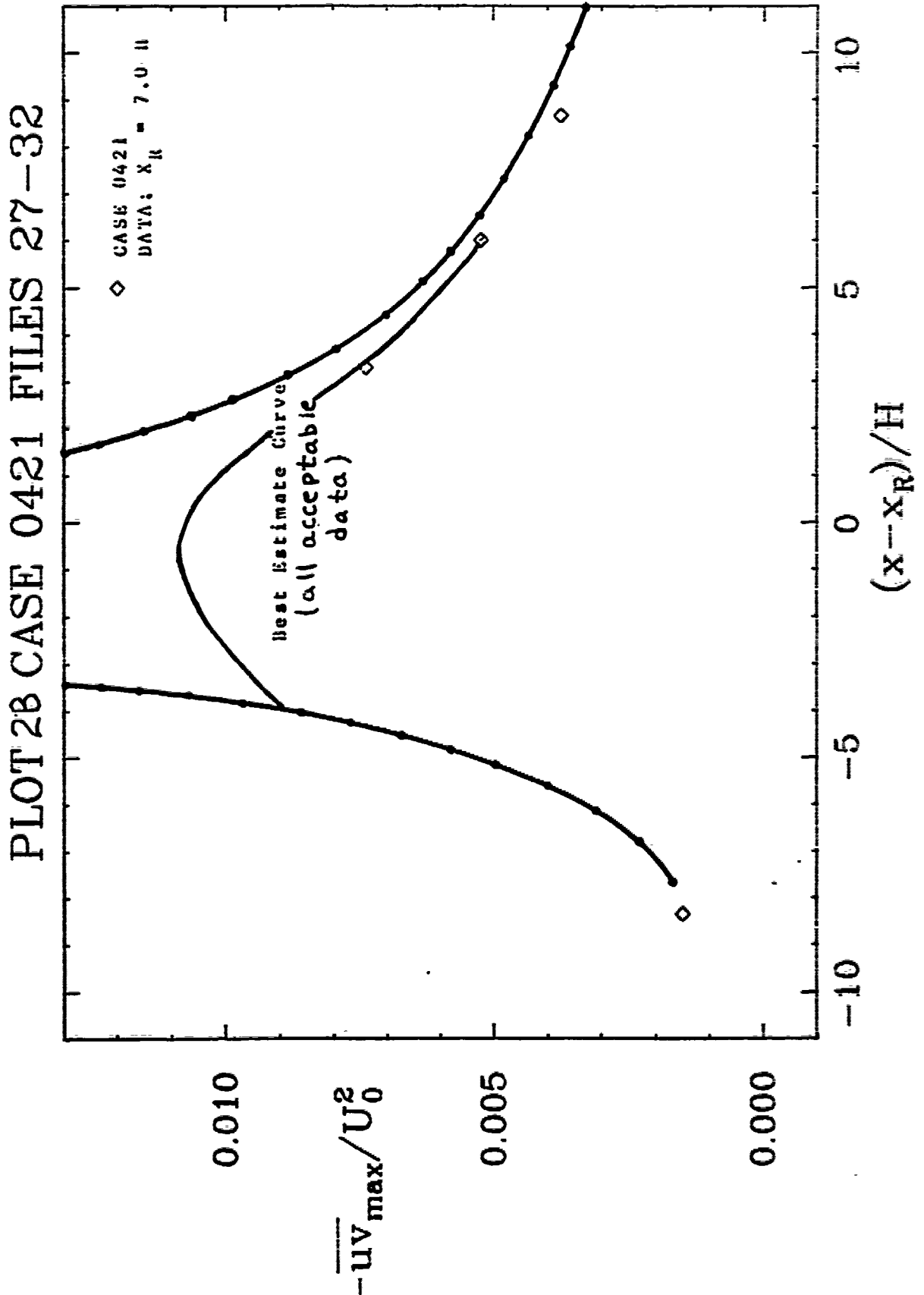


Figure 81. Flow past a backward-facing step.

PLOT 3 CASE 0421 FILES 19,22,25

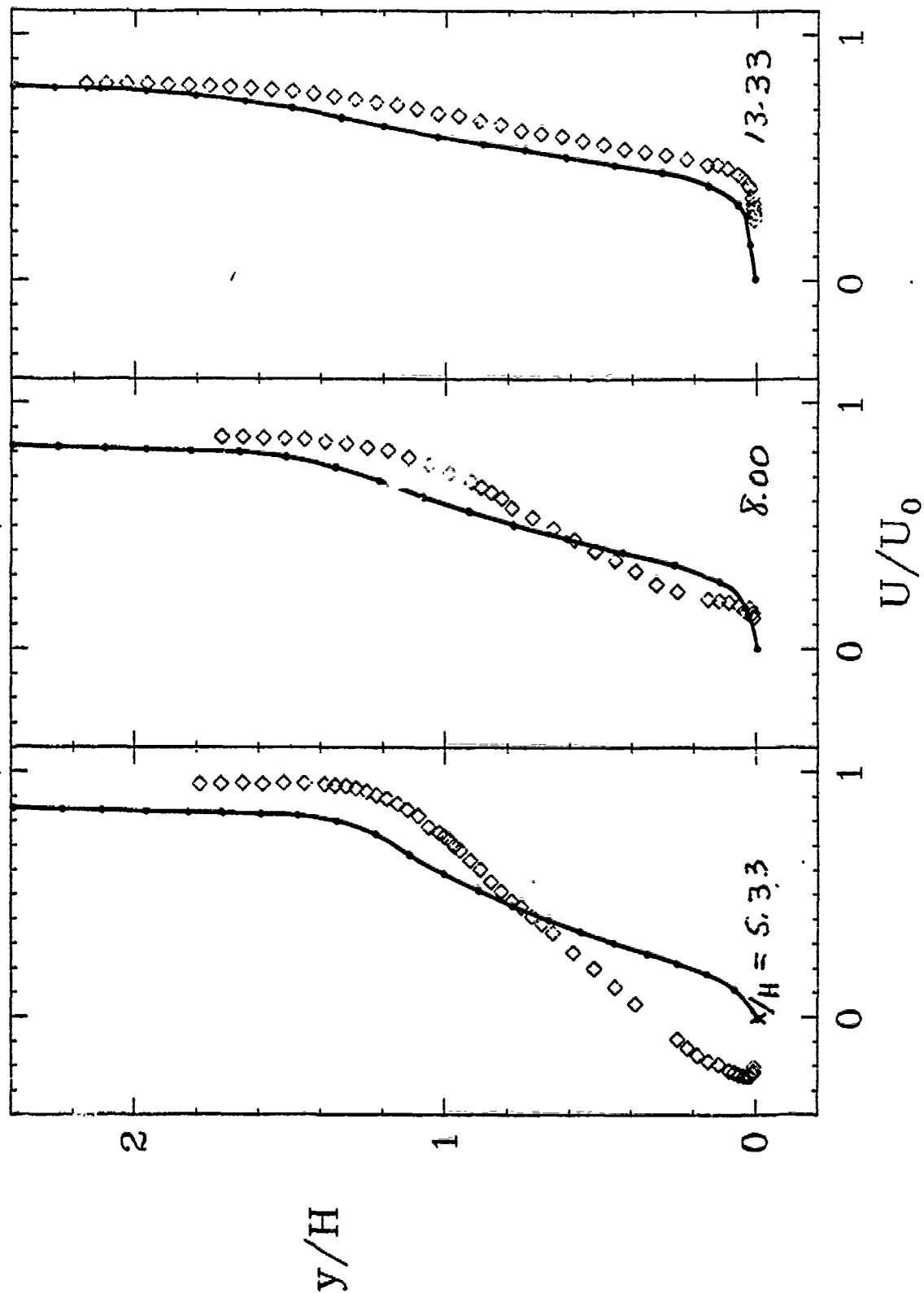


Figure 82. Flow past a backward-facing step.

PLOT 4 CASE 0421 FILES 28,30,32

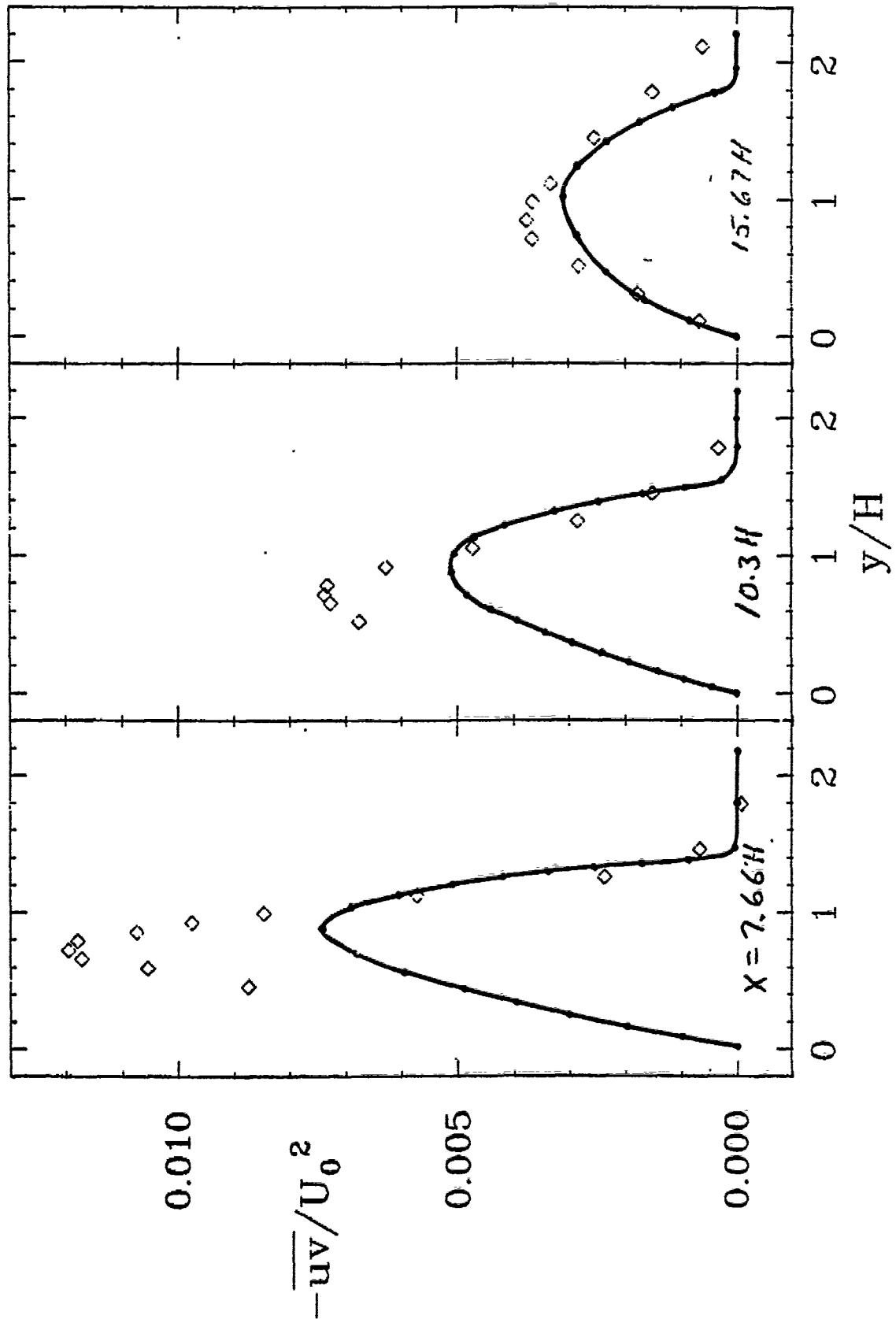


Figure 83. Flow past a backward-facing step.

APPENDIX
WALL FUNCTIONS

The purpose of this Appendix is to provide some insight into the use of so-called "wall functions" with advanced turbulence models. In its original form, this Appendix was submitted to the Stanford Olympics Committee as a note and, except for minor editorial changes needed for consistency with this report, is reproduced in its entirety.

1. Mathematical Meaning of Matching to the Law of the Wall

Generally speaking, in order to solve the equations of motion for a viscous flow over a solid surface one must specify boundary conditions valid at the surface. Often, in turbulent flow computations, it is convenient to avoid integration through the sublayer. This can be done by assuming the law of the wall to be valid for the flow of interest so that we write (for incompressible flow)

$$u_2 = u_\tau \left(\frac{1}{\kappa} \log \frac{u_\tau y_2}{\nu} + B \right) \quad (A1)$$

where u_τ is friction velocity, κ is Karman's constant, $B \sim 5$ for smooth walls and ν is kinematic viscosity. The quantities u_2 and y_2 denote tangential velocity and normal distance from the surface at the first mesh point adjacent to the surface.

The first point I wish to make is that in a strict mathematical sense the boundary condition we are actually using when we invoke Equation (A1) is:

$$u \rightarrow u_\tau \left(\frac{1}{\kappa} \log \frac{u_\tau y}{\nu} + B \right) \quad \text{as } y \rightarrow 0 \quad (A2)$$

We are in fact idealizing the flow as having (relative to the overall scale of the boundary layer) a zero thickness sublayer.

2. The Origin of "Wall Functions"

When a turbulence model is used which involves additional differential equations describing evolution of turbulent field properties, more boundary conditions are needed. For example, using the Wilcox-Rubesin¹ two-equation model of turbulence we must also specify the appropriate "boundary" conditions for the turbulent mixing energy, e , and turbulent dissipation rate per unit energy, ω . It is at this point that the concept of so-called "wall functions" is introduced. These functions generally are deduced by examining the limiting form of the turbulence-model equations as $y \rightarrow 0$. The equations simplify in this limit primarily through dropping of the convection terms. For example, in a constant pressure boundary layer the Wilcox-Rubesin model equations simplify in this limit to the following:

$$\frac{e}{\omega} \frac{du}{dy} = u_{\tau}^2 \quad (A3)$$

$$\frac{e}{\omega} \left(\frac{du}{dy} \right)^2 - \beta^* \omega e + \sigma^* \frac{d}{dy} \left(\frac{e}{\omega} \frac{de}{dy} \right) = 0 \quad (A4)$$

$$\gamma \omega \left(\frac{du}{dy} \right)^2 - \left\{ \beta + 2\sigma \left(\frac{d\ell}{dy} \right)^2 \right\} \omega^3 + \sigma \frac{d}{dy} \left(\frac{e}{\omega} \frac{d\omega^2}{dy} \right) = 0 \quad (A5)$$

where ℓ is turbulent length scale defined by $\ell = e^{1/2}/\omega$ and β , β^* , γ , σ , σ^* are closure coefficients whose values are

$$\left. \begin{aligned} \beta &= 3/20, & \beta^* &= 9/100 \\ \sigma &= 1/2, & \sigma^* &= 1/2 \\ \gamma &= 10/9 \end{aligned} \right\} \quad (A6)$$

It is easy to show that one solution to Equations (A3-A5), which we shall denote as $e=e_w$ and $\omega = \omega_w$, is:

$$e_w = u_{\tau}^2 / \sqrt{\beta^*} \quad (A7)$$

$$\omega_w = u_{\tau} / \sqrt{\beta^*} \kappa y \quad (A8)$$

where κ is the Karman constant, a fact which has been arranged by selecting the closure coefficients to satisfy the condition $\gamma = \beta/\beta^* - 2\sigma\kappa^2/\sqrt{\beta^*}$. Equations (A7 - A8) generally are referred to as wall functions. In computations, Equations (A7 - A8) are used to define e_2 and ω_2 at $y=y_2$.

The second point I wish to make is that, as with the law-of-the-wall velocity boundary condition, the precise mathematical statement of the "wall-function" boundary conditions for e and ω is

$$\left. \begin{array}{l} e \rightarrow e_w \\ \omega \rightarrow \omega_w \end{array} \right\} \text{ as } y \rightarrow 0 \quad (\text{A9})$$

3. Non-Uniqueness of Wall Functions

Now, because the equations for e and ω are of second order, Equations (A7 - A8) are not the only solutions of Equations (A3-A5). In fact, by changing independent variables from y to u one can show immediately that the e equation simplifies to

$$\sigma^* \frac{d^2 E}{dU^2} = \beta^* E^2 - 1 \quad (\text{A10})$$

where $E = e/u_\tau^2$ and $U = u/u_\tau$. As above, one solution has $dE/dU = 0$ so that $E = 1/\sqrt{\beta^*}$. There are also solutions having $dE/dU \neq 0$ which can be obtained by multiplying both sides of Equation (A10) by dE/dU and integrating twice to obtain

$$U = U_0 \pm \sqrt{\frac{3}{2} \frac{\sigma^*}{\beta^*}} \int_{E_0}^E \frac{d\xi}{\sqrt{\xi^3 - \frac{3}{\beta^*} \xi + A}} \quad (\text{A11})$$

where A is an integration constant and E_0, U_0 denote reference values of E, U . Equation (A11) is an elliptic integral whose properties vary widely with the value of the integration constant A . It is not my purpose here to examine in detail the behavior of E contained in Equation (A11). Rather, I wish only to emphasize that more than one solution to the model equations exists and that, without careful analysis, we cannot be sure that all solutions necessarily

are consistent with the law of the wall.

Based on this observation, the third point I wish to make is that arbitrarily deviating from Equations (A7-A9) by using some value other than β^* and/or κ may introduce unexpected surprises, many of which may be hiding in the integrand of Equation (A11). In essence, in selecting the "wall functions" defined in Equations (A7 - A8) we are (a) demanding that our boundary conditions be consistent with the differential equations and (b) excluding any other asymptotic (as $y \rightarrow 0$) behavior which might be inconsistent with the law of the wall.

4. Effects of Pressure Gradient

All of the analysis above assumes constant pressure. As will be shown in this section, Equations (A7 - A8) are inappropriate unless boundary conditions are applied much closer to the surface than is done in common practice. To see this, note that now Equation (A3) must be replaced by

$$\frac{e}{\omega} \frac{du}{dy} = u_{\tau}^2 + \frac{1}{\rho} \frac{dp}{dx} y \quad (A12)$$

where ρ is density and dp/dx is pressure gradient. Equations (A4) and (A5) remain as before. Letting $y^+ = u_{\tau} y / \nu$ we can rewrite Equation (A12) as

$$\frac{e}{\omega} \frac{du}{dy} = u_{\tau}^2 \left(1 + \frac{\nu dp/dx}{\rho u_{\tau}^3} y^+ \right) \quad (A13)$$

Order of magnitude estimates for typical attached boundary-layer flows in pressure gradient indicate the dimensionless grouping multiplying y^+ is a small parameter. This suggests seeking a solution of the form

$$\left. \begin{aligned} e &= \frac{u_{\tau}^2}{\sqrt{\beta^*}} (1 + \phi e_1 + \dots) \\ \omega &= \frac{u_{\tau}}{\sqrt{\beta^* \kappa y}} (1 + \phi \omega_1 + \dots) \\ \frac{du}{dy} &= \frac{u_{\tau}}{\kappa y} (1 + \phi u_1 + \dots) \end{aligned} \right\} \quad (A14)$$

where, for simplicity, we have defined our small parameter ϕ as follows:

$$\phi = \frac{vdp/dx}{\rho u_{\tau}^3} \quad (A15)$$

For the sake of brevity, I omit details of the algebra and simply state the final solution up to terms linear in ϕ , viz,

$$\left. \begin{aligned} e_1 &= \frac{36}{31} y^+ \\ \omega_1 &= -\frac{28}{31} y^+ \\ u_1 &= -\frac{33}{31} y^+ \end{aligned} \right\} \quad (A16)$$

Consequently, for flows in adverse pressure gradient Equation (A2) must be replaced by

$$u \rightarrow u_{\tau} \left(\frac{1}{\kappa} \log \frac{u_{\tau} y}{\nu} + B - \frac{33}{31} \frac{\phi}{\kappa} \frac{u_{\tau} y}{\nu} \right) \quad \text{as } y \rightarrow 0 \quad (A17)$$

while, to this order of approximation, the wall functions e_w and ω_w defined in Equations (A7 - A8) must be replaced by

$$e_w = \frac{u_{\tau}^2}{\sqrt{\beta^*}} \left\{ 1 + \frac{36}{31} \phi \frac{u_{\tau} y}{\nu} \right\} \quad (A18)$$

$$\omega_w = \frac{u_{\tau}}{\sqrt{\beta^* \kappa y}} \left\{ 1 - \frac{28}{31} \phi \frac{u_{\tau} y}{\nu} \right\} \quad (A19)$$

To show the importance of the order ϕ corrections in the wall functions, Figure A1 shows results of a computation with the Wilcox-Rubesin model in which the order ϕ corrections were omitted. The flow considered was the Bradshaw "Flow C" adverse pressure gradient boundary layer⁷. In the computation "surface" boundary conditions were applied at values of y^+ ranging between 12 and 20. The figure compares computed turbulent mixing energy at $x = 7$ feet with Equation (A18). At this position the value of y^+ for the mesh point

$$\sqrt{\beta^*} e/u_\tau^2$$

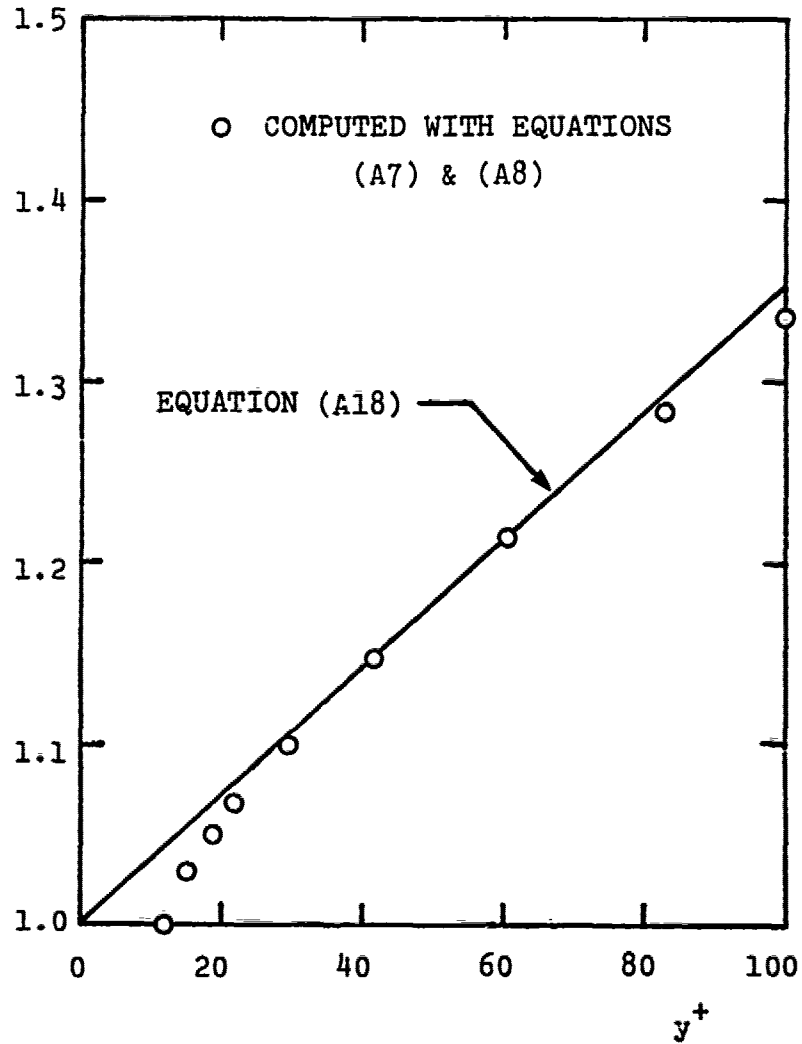


Figure A1. Deviation of computed turbulent mixing energy from predicted near-wall behavior resulting from use of zeroth-order wall functions; Bradshaw "Flow C" adverse pressure gradient boundary layer; $x = 7$ feet.

nearest the surface is 12. As shown, the numerical solution rapidly approaches the analytical solution given by Equation (A18) and the two solutions differ by less than 2% above $y^+ = 30$.

In a subsequent solution in which order ϕ corrections to the law of the wall and the wall functions were included, the numerical and analytical solutions are virtually identical up to about $y^+ = 70$ beyond which point terms of order ϕ^2 presumably become important.

Skin friction for these two numerical computations changed by less than 2% indicating the neglect of the order ϕ corrections was not terribly important in this particular computation. However, please note that in applying the boundary conditions at $y^+ = 12$ our error in e was only 4%. Had we applied the boundary condition at a value of $y^+ = 40$ (which is typical for those who use wall functions in their work), the error in e increases to 14% which could very easily result in a skin friction error of 5% or more. Indeed, I did some numerical experimentation years ago and found that c_f would change substantially with the point of application of the boundary conditions when the order ϕ corrections are omitted. The fourth point I wish to make is that, by contrast, solutions are virtually independent of this point of application when the order ϕ corrections are included.

5. Other Effects

Similar perturbation analyses can be used to determine near-wall behavior of an advanced turbulence model including effects such as compressibility and surface mass transfer³. In my work I generally integrate through the sublayer so I have found no need to derive any but the leading order solutions. I have made such derivations only to investigate limiting behavior of the model in order to check for consistency with physical reality. Hence, my past work offers no further assistance to those wishing to use wall functions. However, the procedure is no more complicated than outlined above and also in Reference 3.

6. Summary

In conclusion I would like to summarize the points made above and add one further comment. The key points I am making are:

1. In matching to the law of the wall we are, in a strict mathematical sense, insisting upon specified asymptotic behavior of the velocity/surface-stress relationship in the limit $y/\delta \rightarrow 0$, where δ is a length characteristic of overall scale of the boundary layer;
2. In using "wall functions" we are likewise insisting upon specified asymptotic behavior of turbulence-field properties in the limit $y/\delta \rightarrow 0$;
3. Wall functions are not unique. For a given turbulence model, there generally is more than one asymptotic solution as $y/\delta \rightarrow 0$ and only one of these solutions can usually be said with certainty to be consistent with the law of the wall;
4. In using wall functions for flows with pressure gradient, surface mass transfer, etc., solution accuracy can be impaired if proper account is not taken of these effects upon the wall functions and upon their point of application.

If proper account is taken of the points above, it is possible to eliminate at least one key area of uncertainty in numerical work and in turbulence-model research in which advanced turbulence models are used. For example, as noted above, solutions become independent of the location of the mesh point nearest the surface (provided $y^+ < 60$ for that point) when Equations (A17-A19) are used in place of Equations (A2) and (A9) for the Bradshaw "Flow C" case. Such an end, I feel, more than justifies the effort involved in performing a straightforward perturbation analysis of the asymptotic behavior of a given turbulence model. This behavior is, of course, unique

to each model; Equations (A16), for example, are valid only for the Wilcox-Rubesin model. The behavior peculiar to any other model nevertheless can be determined once and for all using the same kind of perturbation analysis. The modest effort involved should greatly reduce uncertainty about numerical procedures employed by those who make use of wall functions.

REFERENCES

1. Wilcox, D.C. & Rubesin, M.W., "Progress in Turbulence Modeling for Complex Flow Fields Including Effects of Compressibility," NASA TP 1517 (Apr 1980).
2. Wilcox, D.C. & Chambers, T.L., "Streamline Curvature Effects on Turbulent Boundary Layers," AIAA J, Vol 15, pp 574-580 (1977).
3. Wilcox, D.C. & Traci, R.M., "A Complete Model of Turbulence," AIAA Paper 76-351 (July 1976).
4. Wilcox, D.C., "User's Guide for the EDDYBL Computer Program," DCW Industries Report DCW-R-14-02 (Nov 1976).
5. Gosman, A.D. & Ideriah, F.J.K., "TEACH-2E: A General Computer Program for Two-Dimensional, Turbulent, Recirculating Flows," Imperial College (July 1976).
6. Saffman, P.G. & Wilcox, D.C., "Turbulence Model Predictions for Turbulent Boundary Layers," AIAA J, Vol 12, pp 541-546 (1974).
7. Coles, D.E. & Hirst, E.A., "Computation of Turbulent Boundary Layers - 1968 AFOSR-IFP-Stanford Conference", Vol II, Stanford Univ (1969).